2007

Measurement and modeling of the anhysteretic magnetization of magnetic cores for temperature and frequency dependent effects

Jeremy M. Walker
University of South Florida

Measurement and Modeling of the Anhysteretic Magnetization of Magnetic Cores for Temperature and Frequency Dependent Effects

by

Jeremy M. Walker

A dissertation submitted in partial fulfillment
of the requirements for the degree of
Doctor of Philosophy
Department of Electrical Engineering
College of Engineering
University of South Florida

Major Professor: Stephen E. Saddow, Ph.D.
Wesley C. Tipton, Ph.D.
David Rabson, Ph.D.
Lawrence Dunleavy, Ph.D.
Paris Wiley, Ph.D.

Date of Approval:
July 20, 2007

Key Words: Jiles-Atherton model, transformer, inductor, BH loop, power electronics

To my love, Christalee, your life has made mine.

Acknowledgments

I cannot in good conscious forget the tremendous and selfless investments made by those individuals who supported, encouraged, and helped me toward the end of such a long journey. To Christalee, who has lifted my spirit in times of discouragement, I am grateful for the love, encouragement, and support that you have shown me throughout these years. To mom, dad, and Jonathan, my success in this work is a reflection of the influence and love that you have given me. You are never far away from my heart.

To Dr. Stephen Saddow, there are few words that can describe the type of thanks that I would like to give and desire to give to my major professor and friend. Your care for others, your belief in them, and your desire for them to succeed is unmatched by any other. You are an example to your peers, and without you I would not have attempted nor completed this work. To Dr. Wesley Tipton, I thank you for your continued support and direction throughout this work and for the opportunities provided to me through the Army Research Lab.

To the friends I leave behind that I have worked with for so many years, I thank each of you for helping me, befriending me, and sharing a part of yourself with me. Each of you has taught me something new about life, and I am thankful to have shared a portion of my life with yours. I would like to sincerely give my humble thanks to Camilla Coletti, Gene Short, Ian Haselbarth, Norelli Schettini, Chris Locke, Chris Frewin, Drew Hoff, Tim Fawcett and Stephen Bates. You will all be missed.

Table of Contents

List of Figures

Measurement and Modeling of the Anhysteretic Magnetization of Magnetic Cores for Temperature and Frequency Dependent Effects

Jeremy M. Walker

ABSTRACT

Inductors and transformers are electrical devices critical to power conversion systems. The current-voltage (*I-V*) behavior of these devices is very nonlinear as a result of the magnetic cores used in their construction. However, in the design of these power conversion systems the present state of Spice-based models is limited to low frequency and room temperature effects. An addition to the present model found in many Spice type environments, Jiles-Atherton, is the subject of this work.

Chapter 1 of this dissertation introduces the source of these nonlinearities as being a result of the relationship between the magnetic flux density, $\boldsymbol{B}$, and the applied magnetic field, $\boldsymbol{H}$. Chapter two then derives the original mathematical model used in the Spice, Jiles-Atherton, to provide a physical basis of the addition to the model. The original derivation as it can be found in the referenced literature shows that a temperature and frequency dependence on the model does not exist. This work will seek to add such a dependence on temperature first followed by frequency.

Using this approach, the temperature dependence can be modeled without the core experiencing self-heating. The model therefore must be capable of being further modified after the temperature dependence is added.

Chapter 1: Introduction

1.1. Power Electronics Introduction

Within the first two months of 2007, the total U.S. consumption of electrical power rose 6.5% from the previous year to a staggering 675,034 thousand megawatt hours [1]. Worldwide PC sales rose 10.9% in the first quarter of 2007 [2], and by the end of 2006 approximately 233 million cell phone subscriptions [3] had been purchased in the United States. The rising demand for electrical power, energy storage, and power conversion has been driving several vital areas of research such as alternative fuel sources and smart power supplies, all of which are becoming essential elements of our society and economy. Not only can small electrical losses in the power conversion process create huge losses on a large scale, inefficient power conversion can render an electronic device useless. Imagine a cell phone with only a ten minute battery, or a PC that requires twice the space and produces a large amount of heat. Such losses are costly both monetarily and ecologically. Therefore research into the area of power conversion has spawned numerous benefits as well as complex technical challenges. One of which this dissertation aims to directly address.

1.1.1. Classical Power Conversion

If one considers the classical method of power conversion as represented by the linear power supply shown in Figure 1.1 [4]. The need for an alternate method for power conversion will soon become apparent. Although simple in its construction as well as very robust, the linear power supply that performs the function of converting AC line power at 60 Hz into a specific DC quantity can vary widely in efficiency from 20% to 75% [5]. Electrical power is transformed, rectified, filtered, regulated and delivered to the load in a linear fashion. During the process, current continuously flows to maintain the regulation, and power is continuously applied across the regulating device. In Figure 1.1, a BJT performs this function and is seen electrically as a variable resistor [4].

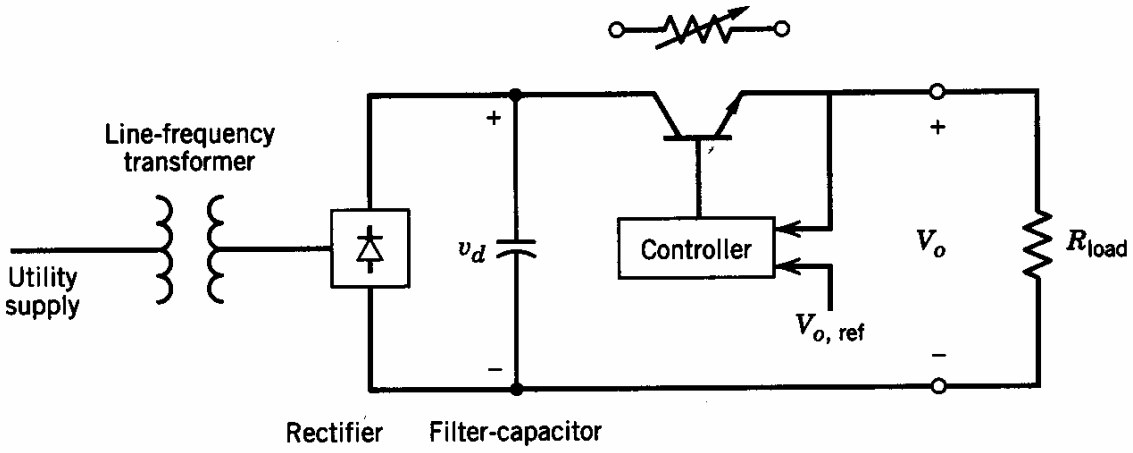

Figure 1.1 Classical linear power supply schematic. The linear regulator is implemented with a BJT that is seen electrically as a variable resistance. Power is regulated to the load by controlling the resistance of the BJT.

Figure copied from [4].

Because of the linear design, the power at the input is either applied to the load or is applied across the regulator. The later causes the power to be converted into heat. This type of power conversion scheme is extremely inefficient. In a portable device such as cell phone, such a method of regulating power is unacceptable. Moreover, a large volume of space is required to implement the power transformer required in the linear power conversion process. This is primarily due to the use of a magnetic core in the transformer's construction. Such a large size would be both cumbersome and expensive for many practical portable products.

1.1.2. Switch-Mode Conversion

In examining the classical linear power supply, power is continuously consumed by the regulator in an inefficient manner and transformed into heat. In contrast, if the BJT in Figure 1.1 was replaced by an ideal switch, then the total power consumed when the switch is open would be zero. The switch could then be toggled at a given frequency to regulate power to a load. This is the most basic idea behind switch-mode power conversion. Hence, the efficiency would dramatically improve as no power would be consumed when the switch was open [4], and the power to the load could still be regulated. Such a design is common in many electrical systems such as a PC that can now have upwards to a 1000 W power supply. The benefits of which are seen greatly in the improved 80%-90% efficiency [5] rating.

The basic design of the switch mode power supply is shown in Figure 1.2 with the ideal switch being implemented with a BJT.

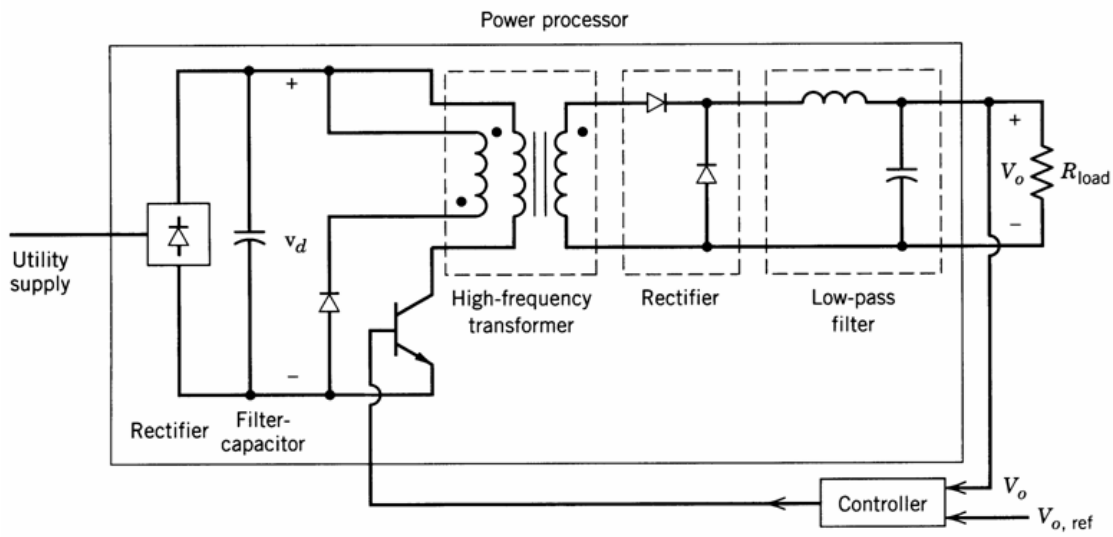

Figure 1.2 Switch-mode power supply showing the input line voltage and key components. Voltage is regulated by a feedback loop controlling BJT. Efficiencies of up to 90% and utilizes a high-frequency transformer.

Figure copied from [4].

A key overall advantage of this scheme lies with the operation of the high-frequency transformer. The largest volume of space in power supplies is consumed by the magnetic component [4] used to make the transformer. To achieve higher power densities, the size of the magnetic components must be reduced. This is achieved by operating the transformer at higher frequencies ranging from 50 kHz to 1 MHz [6]. The volume of the magnetic component relates directly to the energy loss, so shrinking the core's volume is key to increased efficiency as well. However, real magnetic cores that make up component are nonlinear and change as a function of temperature and frequency. A mathematical model for Spice-based applications for frequency and temperature effects is the chief goal of this research. Such a model would greatly aid the designer in the application of these magnetic components.

The basic principle governing magnetic components is Faraday's Law, which states that the voltage is proportional to the change in magnetic flux,ϕ, with respect to time is given by the following equation [7]:

$$V(t) = -N\frac{d\varphi}{dt} = -N\frac{d}{dt}\int_S \boldsymbol{B}\cdot\boldsymbol{ds} = -NA_c\frac{d\boldsymbol{B}}{dt} \tag{1.1}$$

Here the flux density, $\boldsymbol{B}$, relates the induced voltage, $V(t)$, to the cross-sectional area of the core, A_c and the number of winding turns around the core, N. In the ideal sense, the same voltage can be induced across the core if the change in $\boldsymbol{B}$ with respect to time is balanced by an appropriate change in core size. In this way, the magnetic core which is quite large for AC line frequencies can be made quite small at very high switching frequencies [4]. However, the actual flux density, $\boldsymbol{B}$, is nonlinear as a result of the material composing the core.

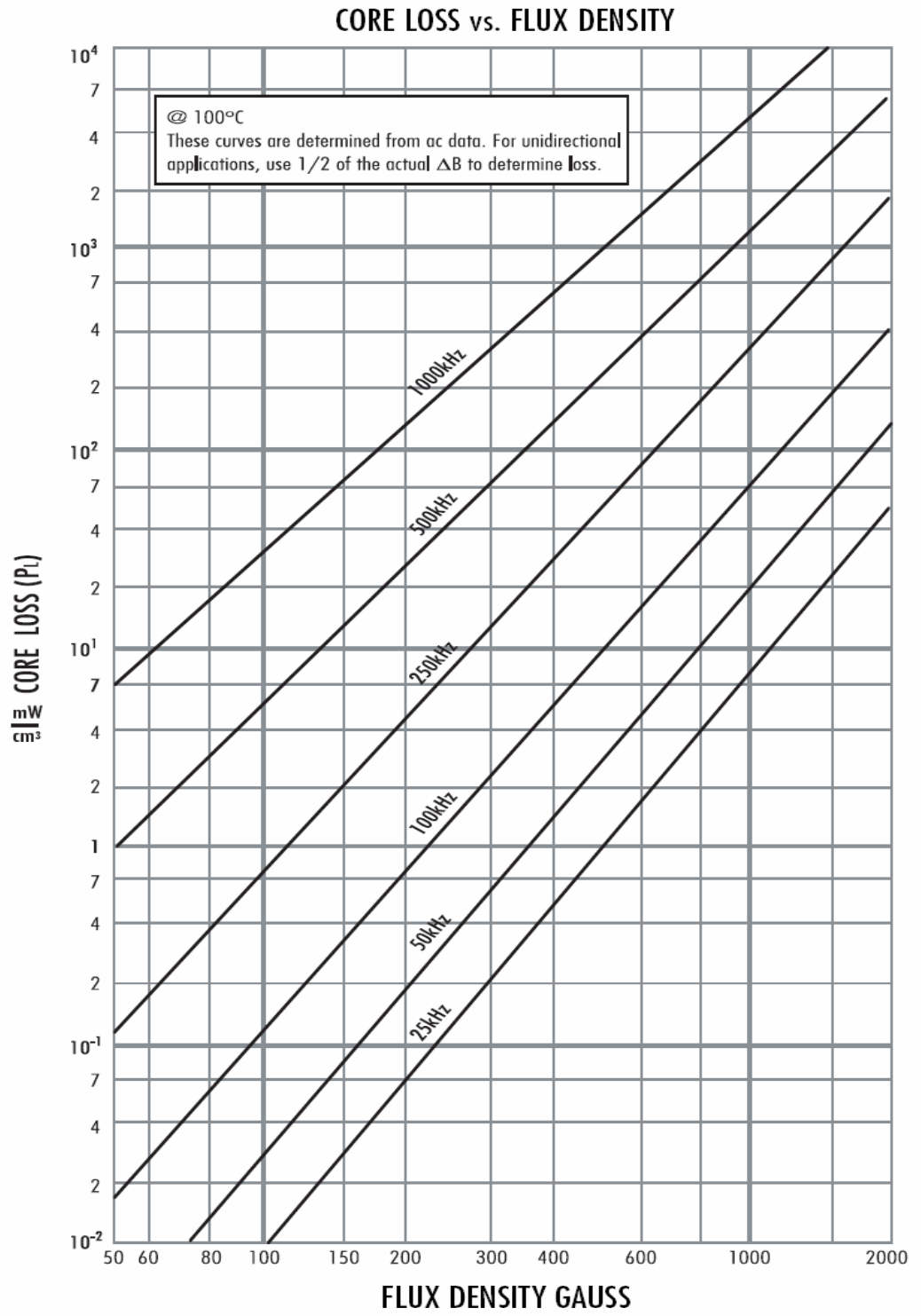

Figure 1.3 Core loss divided by volume as a function of flux density.

Figure copied from [8].

The trade-off in power consumption is also positive as the core loss due to high higher frequency operation is proportional to the volume of the core [9]. This means transformers or inductors can satisfy the same current-voltage (*I-V*) characteristic while consuming less power with a simultaneous increase in overall power density.

Usually, in the analysis and design of switch-mode power conversion, the switching components are assumed to be ideal switches [4]. Accepting this assumption still leaves a large number of nonlinear waveforms to be processed that are a result of the switching scheme used in the circuit. These nonlinear waveforms are often applied to a magnetic transformer or inductor that has a core with nonlinear *I-V* terminal characteristics even at room temperature and low frequencies. The basis for this dissertation is to analyze and model magnetic cores as a function of temperature and high-frequency operation so that optimized power electronics design on a circuit level can be performed. This is necessary as present models do not adequately address these challenges as will be discussed more fully in Chapter 2. In order to set the stage for this research, the impact of switching waveforms on the transformer needs to be discussed first.

The output of the high-frequency transformer and the rectifier that follows it may be modeled as a simplified, equivalent circuit as shown in Figure 1.4 [4].

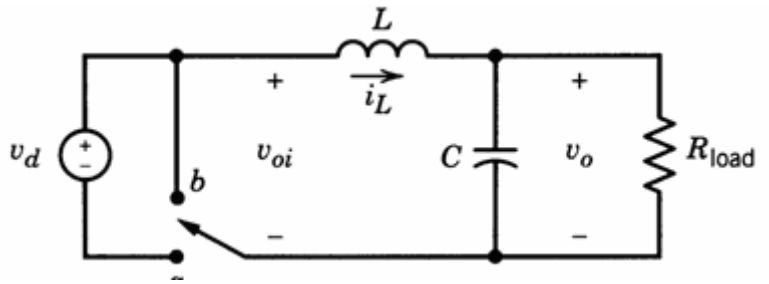

Figure 1.4 Equivalent circuit of the switch-mode power supply shown in Figure 1.2. The DC voltage, v_d, is formed from the rectified output of the high-frequency transformer.

Figure copied from [4].

If one observes the output of the rectified DC voltage that is passed from the high-frequency transformer, a large number of unwanted harmonics are filtered at the output by the tuning of the inductor and capacitor.

However, the purpose of this discussion is to point out the nonlinearities in the voltage waveforms that are processed and produced by component blocks in the circuit, while still holding to the assumption that the components themselves are ideal. In Figure 1.5, V_{oi} represents the rectified DC output of the power supply, which is the mean value over time. v_{oi} represents the total voltage both AC and DC from the conversion process.

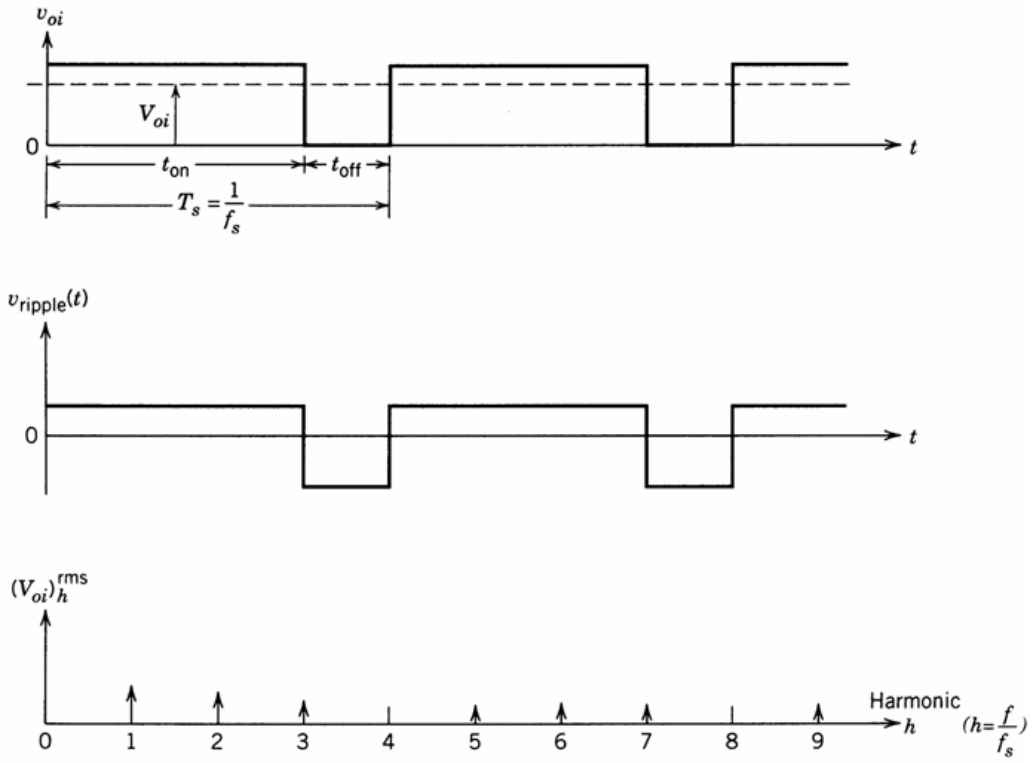

Figure 1.5 Waveforms produced by the high-frequency transformer and rectified as a DC value. Note the harmonics that are found in the rectified voltage, $V_{oi.}$

Figure copied from [4].

Even with these ideal considerations, a large number of harmonic components are applied across the high-frequency transformer. In reality, the *I-V* behavior of the transformer is highly dependent on frequency and temperature. This is due to the material properties of the magnetic core from which the transformer is made. The nonlinearities in the *I-V* relationship due to frequency and temperature effects are an additional technical challenge that is compounded by the nonlinear waveform processing. Notice also that the output of the high-frequency waveform in Figure 1.4 is also filtered by another magnetic component, namely the inductor in the LC filtering network found at

the output of the power supply. The *I-V* behavior of the inductor also experiences the same dependency on frequency and temperature as the high-frequency transformer. Both of these magnetic components derive their nonlinear characteristics primarily from the composition of their magnetic cores. To understand the origin of these nonlinearities, the ideal ***B-H*** relationship will be introduced. After the ideal ***B-H*** relationship is introduced, the actual ***B-H*** relationship will be discussed. It will be shown, that the nonlinearities of the ***B-H*** relationship will produce nonlinear *I-V* terminal characteristics on a magnetic device. It is the prediction of these nonlinear terminal characteristics that are the object of the current research.

1.2. Research Objective

The research objective of this work is summarized as follows:

1. The research will focus on the Jiles-Atherton (Spice) model.
2. The research will seek to determine if the Jiles-Atherton model can be made temperature dependent, and then implement a thermodynamic version of the model.
3. The research will seek to determine if the Jiles-Atherton model can be made frequency dependent, and then implement a frequency dependent version of the model.

The methodology employed here is not to curve fit as many parameters as possible to a specific core, but to establish techniques, practices, and theory that can be applied to a wide a range of magnetic materials at a much more fundamental level. First, having

added temperature dependence to the Jiles-Atherton model, the addition of high-frequency effects on magnetic cores will be investigated. If practicable the final model will possess a physically based temperature and frequency dependence thus allowing follow-on development of design simulation models to be developed with ease.

1.3. Magnetic Components

At a very basic level, magnetic components depend on the relationship between an applied magnetic field, ***H***, and a resulting magnetic flux density, ***B***. From these two vector fields, the *I-V* characteristics of magnetic component can be determined by application of either Ampere's Critical Law or Faradays' Law. The law that is applied depends on whether a voltage or current is applied to the magnetic core.

There are generally two types of common magnetic components used in power electronics namely inductors and transformers, and there are a multitude of material types, geometries, coatings, wire types and other particulars that complete the design of a magnetic component. However, the chief governing property of a magnetic component is the behavior of its magnetic core. This is because the material properties of a magnetic core determine the ***B-H*** properties of the core and therefore the *I-V* properties of the magnetic device, where ***B*** is the magnetic flux density in Tesla and ***H*** is the applied magnetic field in A/m.

A transformer or inductor is made from the winding of wire around a material that has the unique property of producing a large magnitude of ***B*** in response to an applied ***H***. While all materials can have some magnetic response, the magnitude of ***B*** resulting from an applied ***H*** in most materials is so small that it is of no consequence. However, the

materials that are used in the construction of magnetic cores possess a set of unique properties which allow them to produce a large magnitude of ***B*** in response to ***H***. The details of these properties will be discussed in Chapter 2. Presently, a brief overview of the idealized properties will be presented. Following this, the nonlinearities found in real magnetic materials is introduced.

1.3.1. Ideal Magnetic Components

To construct a magnetic component such as an inductor or transformer, a wire is wound around a magnetic core. The wire carries a current which in turn produces a magnetic field of the type shown in Figure 1.6. When this occurs, the material responds by causing a magnetic flux to flow in the material. It should be noted that this flux is a scalar field that is often measured for the purpose of calculating ***B***. The change in B with respect to time induces a voltage, V(t), from Faraday's Law, on the winding of the coil.

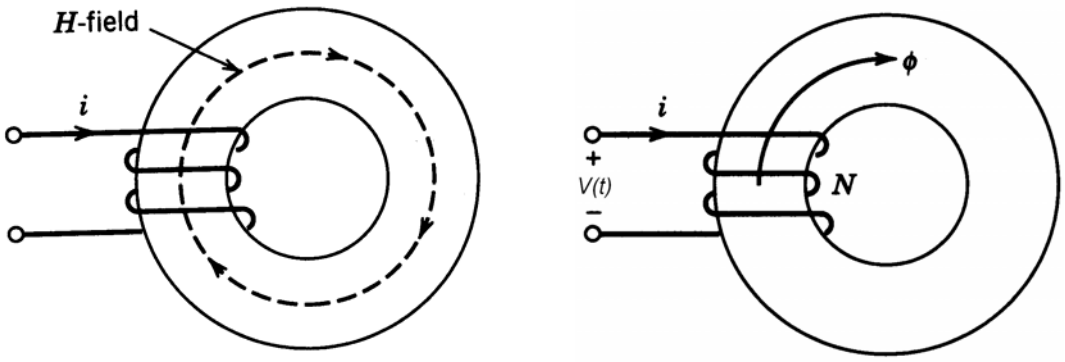

Figure 1.6 Magnetic field in a torrid vs. input current i. (a) A current is applied to a toroidal shaped magnetic core. On the right, the response of the core is shown as a flux, ϕ, causes a voltage to be induced across the winding.

Figure copied from [4].

An ideal representation of the ***B-H*** characteristic of a core is shown in Figure 1.7.

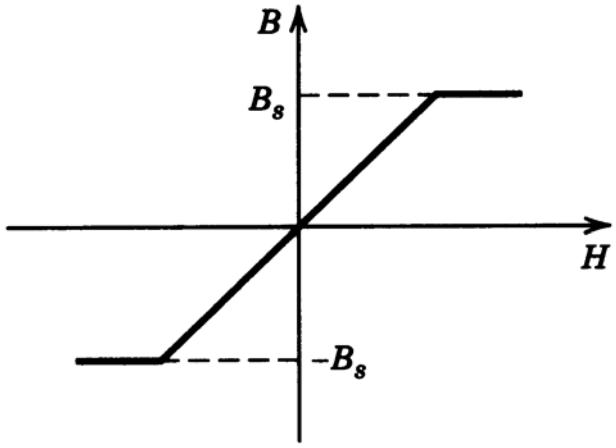

Figure 1.7 Idealized ***B-H*** relationship showing a linear relationship between ***B*** and ***H***. Note that ***B*** has a maximum value, B_s.

Figure copied from [4].

Here, the magnitude of ***B*** depends linearly on the magnitude of ***H***. ***B*** saturates once a certain magnitude of ***H*** is reached, meaning that the magnitude of ***B*** has reached a maximum value, B_s. As the voltage induced is proportional to the change in ***B*** with respect to time, once ***B*** saturates the value of the induced voltage will be zero.

The mathematical expression for the relationship shown in Figure 1.7 is

$$\boldsymbol{B} = \mu \boldsymbol{H} \tag{1.2}$$

Where μ is the permittivity that describes how ***B*** will respond to ***H*** and is a material's parameter and has units of H/m. If ***H*** is sinusoidal, then ***B*** will be sinusoidal. This means that if a sinusoidal current is applied to an inductor with the characteristic ***B-H*** relationship shown in equation (1.2), then the current waveform will produce an ***H*** field with a magnitude proportional to the applied current according to Ampere's Law. ***H*** is

related to ***B*** by μ, so ***B*** is sinusoidal. The induced voltage, *V(t)*, across the winding will also be sinusoidal according to Faraday's Law. To this end, the ideal ***B-H*** relationship of a core is linear.

1.3.2. Real Magnetic Components

Real magnetic components are also characterized by their ***B-H*** relationship. However, a real ***B-H*** relationship is nonlinear and contains hysteresis. This means that the present value of ***B*** depends not only on the present value of ***H***, but on past values of ***H***. The ***B-H*** relationship of a real magnetic core is shown in Figure 1.8. This is commonly called a ***B-H*** loop due to the hysteresis inherent in the curve.

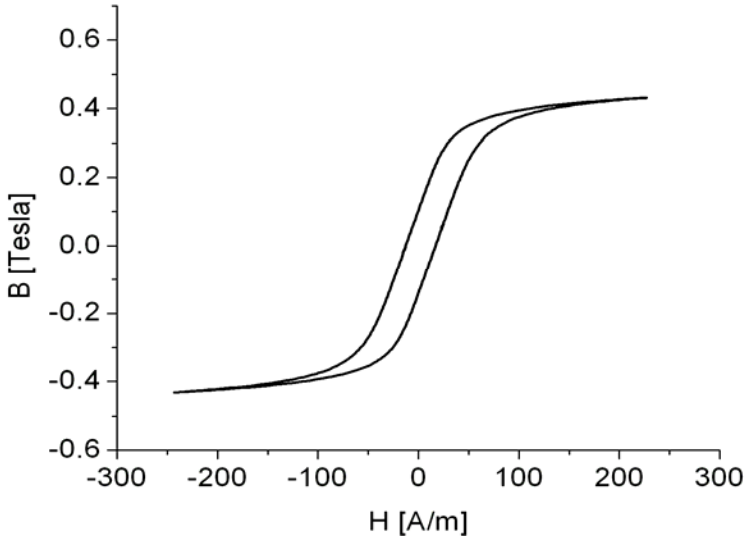

Figure 1.8 ***B-H*** loop measurement performed by the author for a MnZn power ferrite core showing hysteresis. The curve was measured by the Walker Hysteresisgraph AMH-401A courtesy of Magnetics Inc.

The ***B*-*H*** relationship shown in Figure 1.8 is far from a singled-value mathematical function. ***B*** still saturates as in the linear case, however, the hysteresis of the material changes the value of ***B*** making it dependent on past values of ***H***. If a voltage waveform were applied to an inductor or transformer with this ***B*-*H*** relationship, then the resulting *I*-*V* behavior would be nonlinear. If ***B*** and ***H*** are plotted independently as a function of time, these nonlinear characteristics can be further observed. In Figure 1.9 the ***B*** and ***H*** waveforms used to plot the ***B*-*H*** loop in Figure 1.8 are plotted independently as a function of time. The relationship between is nonlinear with $\mu=\mu_r\mu_o$ relating ***B*** and ***H***. The relative permeability, μ_r, is used to describe a specific material and μ_o is the permeability of free space.

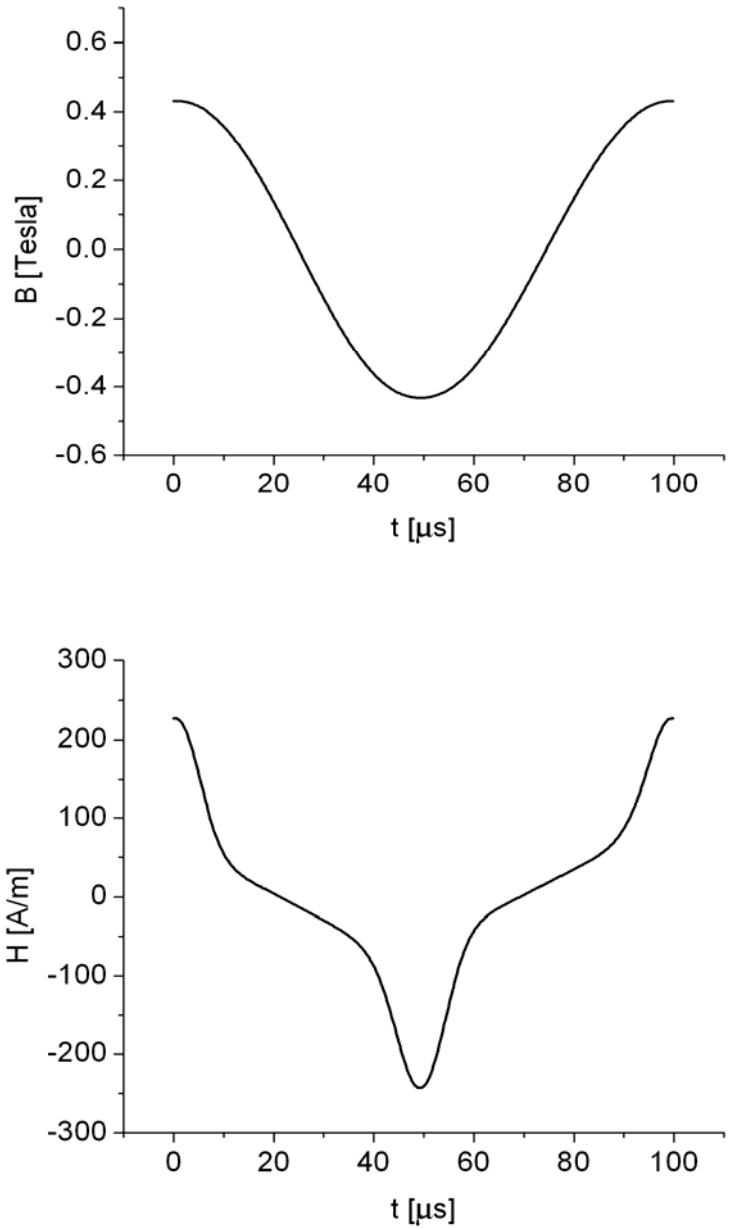

Figure 1.9 *B(t)* and *H(t)* waveforms as a function of time for a sinusoidal input voltage on a MnZn magnetic core. These waveforms were measured by the author and used to construct the ***B*-*H*** plot shown in Figure 1.8.

The resulting waveforms demonstrate the complexities of the ***B*-*H*** relationship even for just a single excitation frequency at room temperature. To further complicate the design process of power electronics, the ***B*-*H*** relationship of real materials is very dependent on the temperature of the material. This means that as a magnetic component heats up during operation due to wasted energy, the *I*-*V* characteristics of the device change as a result of the changing core ***B*-*H*** characteristic. Figure 1.10 shows two ***B*-*H*** loops in the first quadrant plotted as a function of temperature. The magnitude of the applied ***H*** has remained the same. The difference in the loops is due to the effect temperature is having on ***B***. The slope of a point on the plot represents μ, and it is continually changing because ***B*** is not a linear function of ***H***.

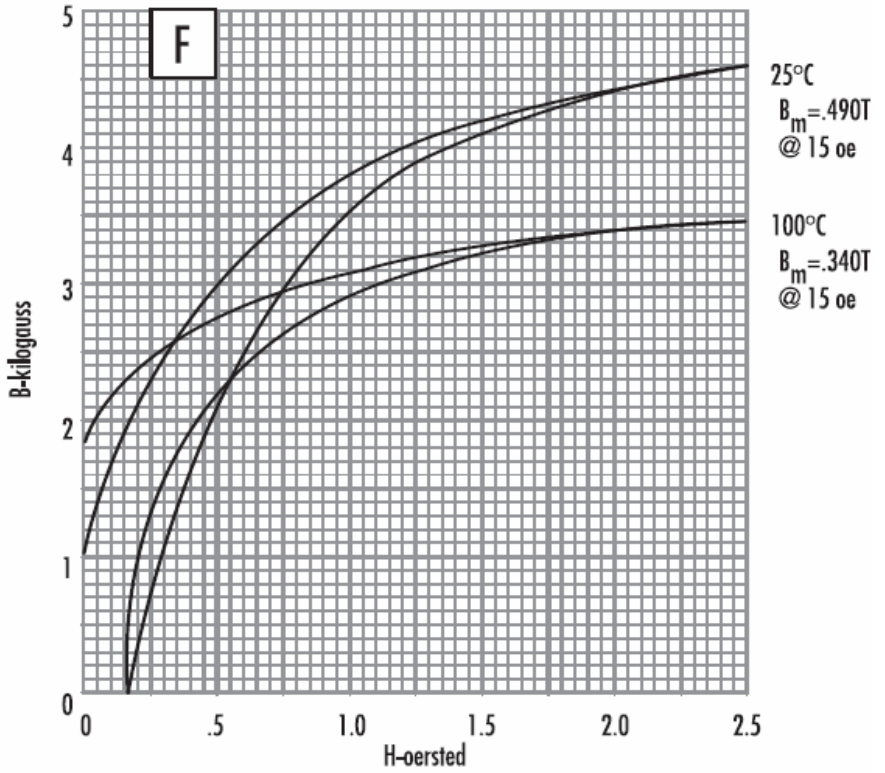

Figure 1.10 Effect of temperature on the ***B*-*H*** relationship. As a direct consequence, the overall *I-V* characteristics of the magnetic component change greatly complicating component and system design.

Figure copied from [8].

The initial permeability, μ_i, is shown in Figure 1.11. It specifically refers to the slope on the line on the ***B*** and ***H*** when the curve begins at the zero coordinate. The origin is called the demagnetized state. Once ***H*** is applied when the core is in the demagnetized state, the value of ***B*** is traced out and the slope is equal to the initial permeability. The dependence of the initial permeability on temperature and the magnitude of ***B*** is also shown in Figure 1.11. The point here is to demonstrate the nonlinear relationship that temperature has on the ***B*-*H*** characteristic of the core.

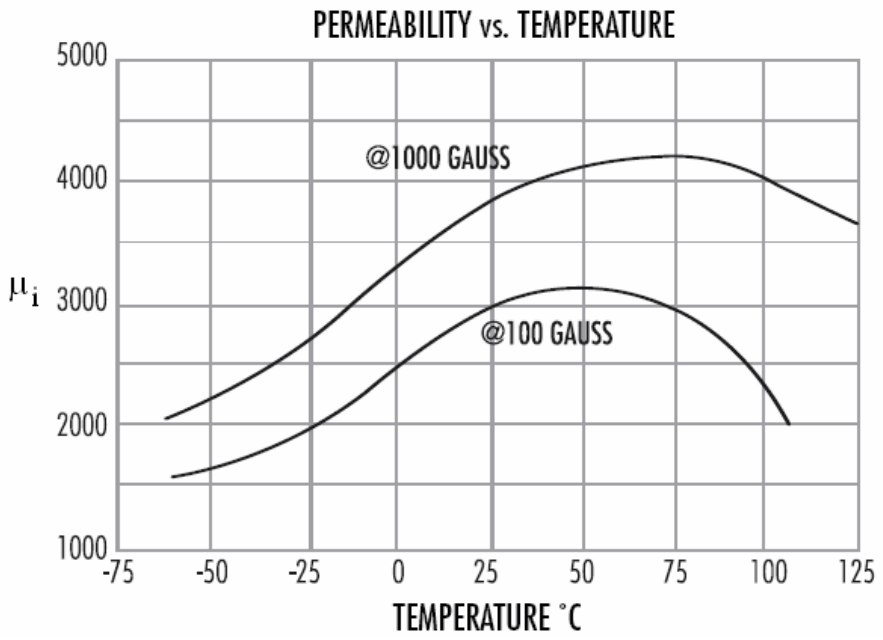

Figure 1.11 The initial permeability plotted as a function of temperature for two different magnitudes of ***B***. The material shown is a MnZn power ferrite.

Figure copied from [8].

Nonlinearities in the ***B***-***H*** characteristics also change as a function of frequency. This is a result of eddy-currents being induced in the material and also a result of the limited penetration depth of the applied ***H*** field into the bulk of the material. At low frequencies, the generated eddy-currents are negligible and the depth of penetration of ***H*** is considered to be throughout the core. In Figure 1.12, the relationship of three types of magnetic cores is shown changing as a function of temperature. Again, this is the initial permeability relating ***B*** and ***H*** as ***H*** is applied from the demagnetized state.

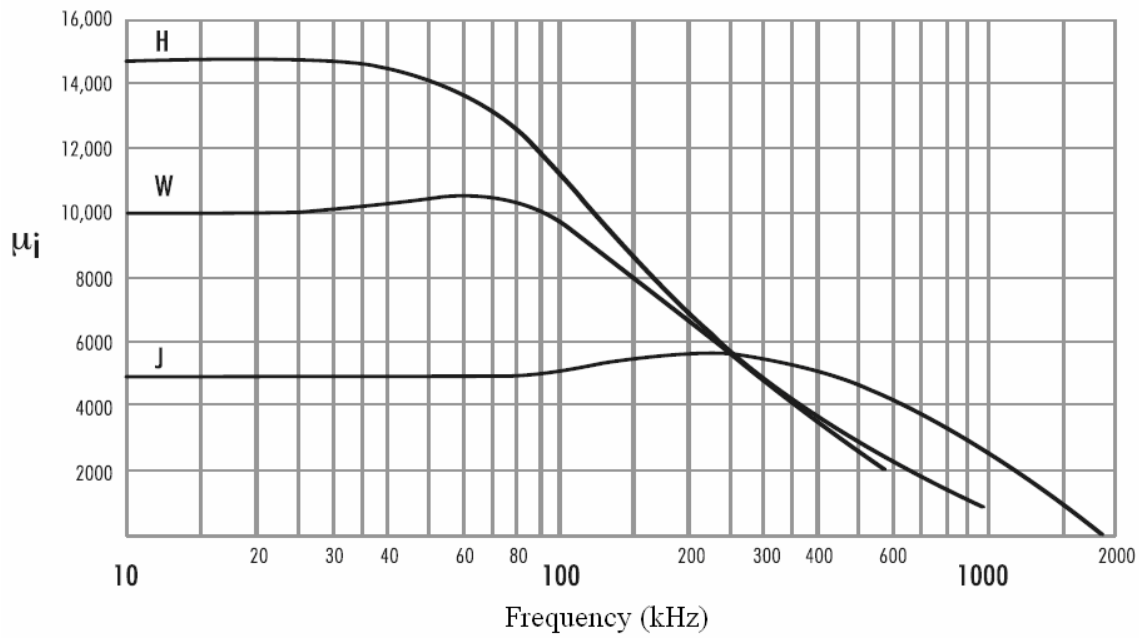

Figure 1.12 Three types of ferrite cores (H, W, J) manufactured by Magnetics, Inc. showing their nonlinear permeability as a function of frequency.

Figure copied from [8].

The trends observed in Figure 1.12 indicate the strong dependence that the ***B*-*H*** relationship has on the frequency of excitation. As a whole, a designer of power electronics must consider both the temperature and frequency of operation of a magnetic component as they both dramatically effect the ***B*-*H*** relationship and the resulting *I-V* behavior.

1.4. Problem Statement

In the design of power electronics, the movement toward higher-switching frequencies is expected as is evident by the benefits they provide [10]. Higher temperature operation is also expected as a result of the energy lost in the power

conversion process [11]. Figure 1.3 has already shown that increased magnitude of ***B*** and increased frequency yield higher losses. The effects cause nonlinear *I-V* characteristics for magnetic components [11]. The magnetic components that are used under these conditions need mathematical models to aid their use and design. One plausible solution is the use of CAD-based design software such as PSpice [12], Saber [13], Maxwell 3D [14], and others, but it should be noted that it is the fundamental problem with the present state of the magnetic component model in these tools that it is the subject of the present research [15].

Over the years the Jiles-Atherton model [16] has become one of the primary models for modeling magnetic components as it models the material properties used for magnetic core. It is implemented in many circuit simulators and physics-based simulators and is used in predicting the ***B-H*** relationship [15]. The reason for the model's popularity comes first from its accuracy in predicting the correct ***B-H*** relationship because the model is based on the fundamental mechanics of the material. The underlying mathematics are also capable of being implemented in a circuit simulator. The model in its present form lacks a true, fundamental dependence on temperature as will be extensively covered in the theory Chapter of this dissertation.

The effect of nonlinearities in a magnetic core due to temperature and frequency are coupled [11], and the Jiles-Atherton model has proven that it can model low frequency and room temperature operation with high accuracy. Several years after the model's initial development, the addition of high-frequency effects were added to the model with modest success [17]. While there are other models which rely upon extensive measured and empirical data, they also lack fundamental temperature dependence.

Moreover, those types of models are too specific to a given core and do not provide the flexibility that the circuit designer requires, which needs to be based solely on the terminal characteristics (i.e., *I-V*) of the component.

1.5. Chapter Conclusion

The basic need for a mathematical model has been demonstrated as evident by the nonlinear nature of not only the magnetic components involved, but of the waveforms applied to these components. While ideal magnetic components would produce a linear sinusoidal waveform from a sinusoidal input, real magnetic components saturate and can make the task of designing power electronics systems difficult. Spice based simulations can aid the designer greatly, but the present Spice based simulation tools are limited as they apply only to room temperature and low frequency operation. The chief goal of this research is to add the capability to model frequency and temperature dependent effects to the present Jiles-Atherton model.

Chapter 2: Theory

2.1. Introduction to Magnetic Materials

When introduced in Chapter 1, the magnetic field, $\boldsymbol{H}$, of an ideal magnetic material was related to the flux density, $\boldsymbol{B}$, through the magnetic permeability $\mu=\mu_r\mu_o$ [7].

$$\boldsymbol{B} = \mu_r \mu_o \boldsymbol{H} \tag{2.1}$$

where μ_r is the relative permeability that characterizes a specific material and μ_o is the permeability of free space.

Ferromagnets and ferrimagnets are used in the making of magnetic cores. These two classifications of magnetic materials exhibit a very nonlinear $\boldsymbol{B}$ field in response to an applied $\boldsymbol{H}$ field [18]. This relationship demonstrates several different physical phenomenon that when averaged over the whole of the core give the hysteretic relationship previously introduced in Chapter 1. To understand this phenomenon, we will first examine some particulars of the $\boldsymbol{B}$-$\boldsymbol{H}$ loop which displays this inherent hysteresis. Following this, we move into the mechanics of how and why this relationship occurs.

In Figure 2.1, an example of a $\boldsymbol{B}$-$\boldsymbol{H}$ plot is presented showing how a real material might respond to a given excitation. Several prominent features can be observed. $\boldsymbol{H}$ is applied to a ferromagnetic material in a sinusoidal fashion. Assuming that the excitation begins with zero magnitude for both fields (i.e., the core is in the demagnetized state), the magnetic field, $\boldsymbol{H}$, forces the magnitude of $\boldsymbol{B}$ to increase until it reaches what is called

inept saturation. At this point, ***B*** has reached its maximum value that is a characteristic of the material. When the magnitude of ***H*** is then decreased to zero, ***B*** has a remaining residual value left in the material known as remanence, B_r. As the magnitude of ***H*** is further decreased to zero, the magnitude of ***B*** is finally forced to a zero value. The magnitude of ***H*** required to force the magnitude of ***B*** to a zero value is called the coercive field, H_c. Again, as the magnitude of ***H*** is further decreased, the magnitude of ***B*** reaches a maximum and becomes saturated. This application of ***H*** causes the ***B-H*** relationship to form a loop sometimes termed a hysteresis loop. The term hysteresis refers to the fact that ***B*** does not depend on present value of ***H***, but also on past values of H [19] The formation of the ***B-H*** loop is shown starting in the demagnetized state in Figure 2.1.

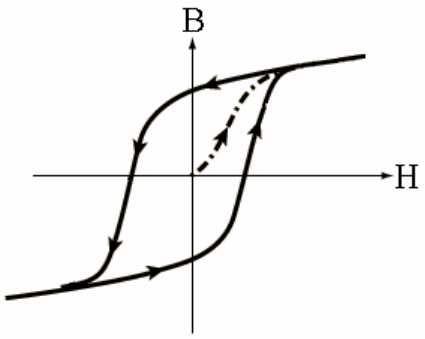

Figure 2.1 ***B-H*** loop formed by the application of a sinusoidal ***H*** to a real magnetic core and the resulting nonlinear response of ***B***. The process shown begins in the demagnetized state at the origin of the ***B-H*** plane.

Figure copied from [20].

In many cases, the application of ***H*** does not force ***B*** into a saturated state. Instead, the field, which can be cyclic, may traverse the ***B-H*** loop in a variety of ways

each of which will form a given ***B-H*** relationship of the magnetic core. The relationship formed by ***B*** and ***H*** will determine the *I-V* characteristics of the magnetic device. When ***B*** does not saturate, the loop is called a minor loop to distinguish it from a major loop formed when the core does reach saturation. This is shown in Figure 2.2 along with the points on the loop where the coercivity and remanence are defined.

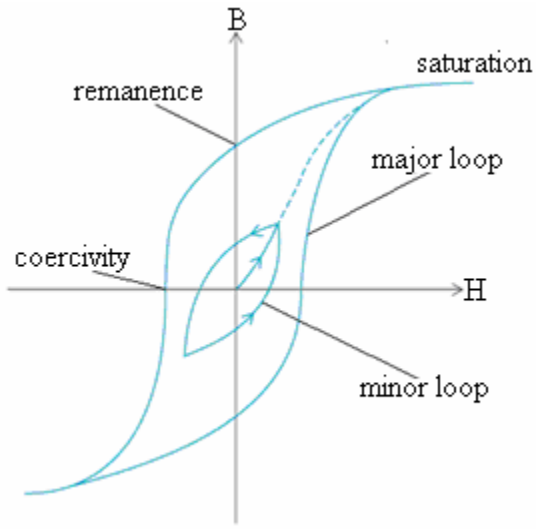

Figure 2.2 Minor and major ***B-H*** loops plus the location of the coercivity and remanence points. Note the minor loop does not reach saturation.

Figure copied from [21].

Minor loops and major loops can take a variety of forms depending on the type of excitation. It can be seen that both forms of the ***B-H*** loops created in Figure 2.2 are nonlinear. It should be noted that a model of the ***B-H*** characteristics needs to be able to predict both minor and major loops.

In understanding why a magnetic core behaves in this type of hysteretic manner, the material itself needs to be discussed on a bulk scale. Before a discussion of the

material begins, the concept of the magnetic dipole moment needs to be introduced. This will provide at a basic level the motivation for the mathematical model of a magnetic core. The objective here is not to give a thorough review of the underlying quantum mechanics of magnetism for which there is a volume of established literature [22, 23]. The point here is to point out how magnetism can naturally be included into the classical form of Maxwell's Equations and how modeling of the bulk material may be accomplished.

2.1.1. Magnetic Moments

It has been known from the early investigations of magnetism and particularly from the pioneering work of Andre Marie Ampere that a magnetic field is caused by a moving electrical charge, which we now refer to as Ampere's Law [24]. Ampere postulated the origin of tiny currents running through the material that could produce a similar effect. In a sense, he was correct. If one considers the classical model of an atom from Neils Bohr's work, then one does find charge moving in a circular pattern around the nucleus of an atom [20]

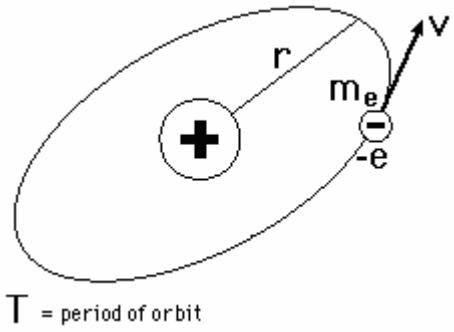

Figure 2.3 Neils Bohr's classical picture of the hydrogen atom with a single electron orbiting the nucleus. The electron's orbit and spin combine to give a net magnetic moment.

Figure copied from [20].

For a given radius, *r*, and charge of the electron, *-e*, it can be shown that given a the electron orbit period, *T*, the negative charge of the electron circling the atom creates a current that can be expressed in the form [20]

$$I = \frac{-e}{T} \tag{2.2}$$

where *I* is in coulombs per second or Amperes. This causes ***H*** to produce the field pattern shown in Figure 2.4.

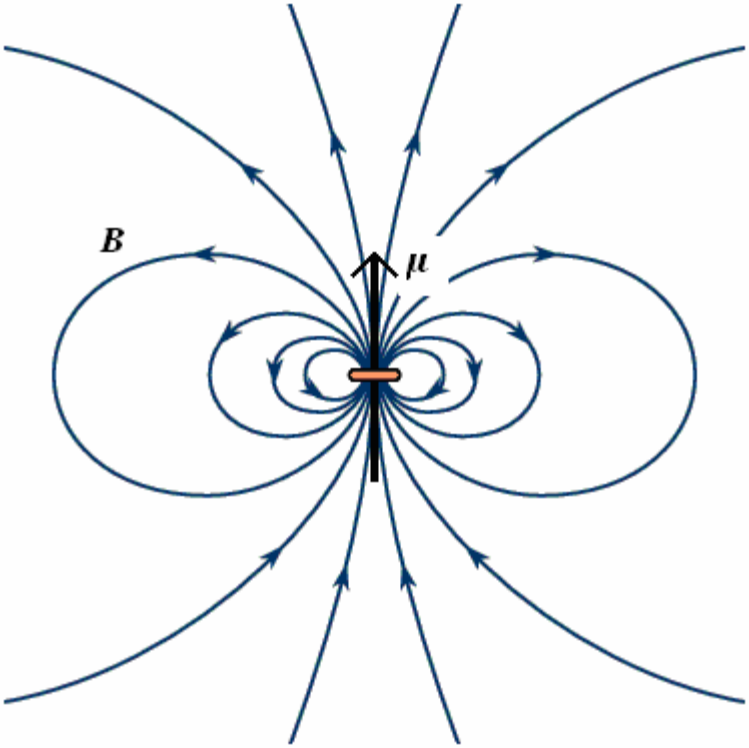

Figure 2.4 Field lines formed from simple current loop. The field line pattern resembles the field lines created by two opposite charges in the electrostatic dipole case. The phenomenon has come to be known as the magnetic dipole moment, $\boldsymbol{\mu}$.

Figure copied from [25].

For the electron period, T, with velocity, $\boldsymbol{V}$

$$T = \frac{|\boldsymbol{V}|}{2\pi\pi} \tag{2.3}$$

The resulting magnetic dipole, $\boldsymbol{\mu}$, is given by

$$\boldsymbol{\mu} = I\boldsymbol{A} \tag{2.4}$$

The magnetic dipole can be written in terms of its angular momentum, $\boldsymbol{L}$, and the electron mass, m_e [20], as

$$\boldsymbol{\mu} = \frac{-e}{2m_e}\boldsymbol{L} \tag{2.5}$$

The magnetic dipole is a vector quantity whose magnitude depends on the cross-sectional area of the current loop and the quantity of charge circulating in the loop. The magnetic dipole is therefore directly proportional to the angular momentum, $\boldsymbol{L}$, of the electron orbiting the nucleus. The direction of the $\boldsymbol{\mu}$ vector is perpendicular to the cross-sectional area of the loop and points in the opposite direction of $\boldsymbol{L}$. The magnetic dipole is usually specified in terms of its angular momentum, $\boldsymbol{L}$ [19] as shown in Figure 2.5.

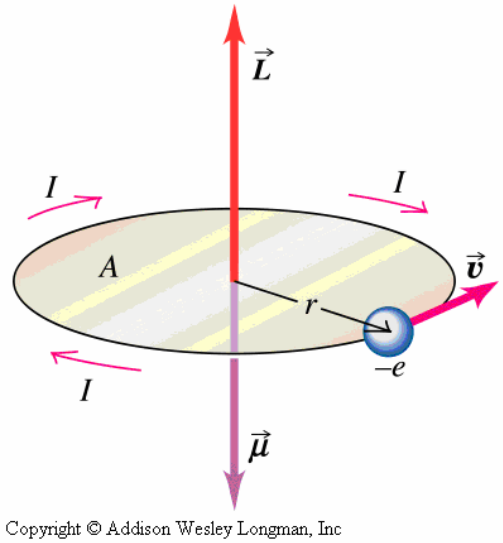

Figure 2.5 Simple representation of a magnetic dipole caused by a charge, -e, circulating around an atom in an orbit of radius, r. The magnitude of the resulting vector $\boldsymbol{\mu}$ is proportional to the magnitude of the angular momentum, $\boldsymbol{L}$, but in the opposite direction.

Figure copied from [26].

Magnetic materials have magnetic moments that are quantized, and it is shown through experiments [27] that the expected value of the magnetic moment does not follow the classical treatment that was just briefly reviewed. The ordering of this

quantization is governed by Hund's Rules [27]. The angular momentum is replaced by the quantized spin angular momentum, $\boldsymbol{s}$, of the electron given as

$$\boldsymbol{m}_{spin} = \frac{-e}{\boldsymbol{m}_e}\boldsymbol{s} \tag{2.6}$$

The magnetic moment created by the orbital motion of the electron then takes the form.

$$\boldsymbol{m}_{orb} = \frac{-e}{2\boldsymbol{m}_e}\boldsymbol{l} \tag{2.7}$$

where the angular momentum, $\boldsymbol{L}$, has been replaced by the quantized orbital angular momentum, $\boldsymbol{l}$. The total magnetic moment of an atom, $\boldsymbol{m}$, is the addition of both magnetic components and is given by

$$\boldsymbol{m} = \boldsymbol{m}_{spin} + \boldsymbol{m}_{orb} \tag{2.8}$$

The important point from a modeling point of view is that the magnetic dipole is treated as magnetization vector of atomic origin. This allows the magnetic dipoles resulting from the atom to be treated as vector type point sources that are fixed locally in the crystal lattice, yet are free to rotate in response to an applied magnetic field.

The summing of these atomistic vectors leads to a total vector magnetic field, $\boldsymbol{M}$, referred to as the magnetization of the material. Ultimately, it is $\boldsymbol{M}$ that is responsible for the nonlinear $\boldsymbol{B}$-$\boldsymbol{H}$ characteristics of a magnetic core. $\boldsymbol{M}$ is a measure of the response of the material to the applied field $\boldsymbol{H}$, and its magnitude specifies the net magnetic dipole moment per unit volume. $\boldsymbol{M}$ is included into the $\boldsymbol{B}$-$\boldsymbol{H}$ relationship as [19].

$$\boldsymbol{B}(\boldsymbol{H}) = \mu_o(\boldsymbol{H} + \boldsymbol{M}(\boldsymbol{H}, \boldsymbol{History\_H})) \tag{2.9}$$

Here the flux density, ***B(H)***, has been specified more precisely as a function of ***H*** and the resulting magnetization, ***M(H, History_H),*** that depends not only on the present value of ***H*** but on past values of ***H***. Every type of material has some magnetic component, but ferromagnetic and ferrimagnetic materials yield significantly high magnitudes of ***M*** that make them ideal for the construction of inductors and transformers [19]. Ferromagnetic materials tend to be metal in composition while ferrimagnetic materials tend to be ceramic and more electronically insulating in composition. Ferromagnets and ferrimagnets differ primarily in that not all of the magnetic dipoles of a ferrimagnetic point in the direction of the applied field. Instead, some of the magnetic dipoles oppose the magnetic field, yet the net overall contribution to the resulting magnetization due to an applied magnetic field is still very high. The ***B-H*** loop for ferromagnets and ferrimagnets look very much the same.

It should be stated that the ***M-H*** loop appears in exactly the same form as the ***B-H*** loop because it is the magnetization, ***M***, that actually determines ***B***. Many times the contribution of the term $\mu_o \boldsymbol{H}$ added to the total ***B(H)*** is negligible in magnitude compared to the μ_o***M(H)*** term. A proper model of the ***B-H*** relationship is therefore a model of ***M(H)*** [19].

2.1.2. Magnet Domains

In considering the modeling of magnetic cores, the two types of fundamental ordering of dipoles in a material are classified as ferromagnetic and ferrimagnetic. Both materials are composed of regions of subdivided space called magnetic domains that

contain magnetic dipoles aligned to the same orientation. The model to be introduced can predict the ***B*-*H*** relationship for both ferromagnetic and ferrimagnetic materials. In fact, it is emphasized that the model to be presented is a phenomenological model of domain mechanics. The model has also been adapted to work with the domain mechanics of ferroelectric materials where the underlying physics for the domain formation are quite different [28]. Figure 2.6 represents an ideal single-crystal, ferromagnetic material.

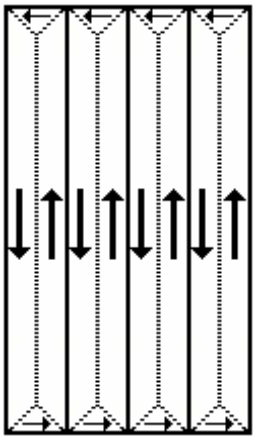

Figure 2.6 Sketch of an idealized single-crystal structure of a ferromagnetic material in equilibrium. Regions of homogenous magnetization are composed of magnetic dipole moments of atomic origin.

Figure adapted from [18].

Each region of the material is subdivided into regions called magnetic domains that contain many magnetic dipole moments of the type discussed in the last section. These moments possess a potential energy known as the magnetostatic energy. This energy can be expressed in terms of $\boldsymbol{M}$ and $\boldsymbol{H_M}$ as [29]

$$U_M = -\frac{\mu_o}{2}\int_V \boldsymbol{H}_{\boldsymbol{M}} \cdot \boldsymbol{M} d^3 r \tag{2.10}$$

$\boldsymbol{H_M}$ here is not the applied field, but the field that results when $\boldsymbol{M}$ diverges, where it can be shown mathematically that the divergence of $\boldsymbol{M}$ creates a magnetic field.

$$\nabla \cdot \boldsymbol{H}_{\boldsymbol{M}} = -\nabla \cdot \boldsymbol{M} \tag{2.11}$$

This allows the overall energy of the field created by the magnetic dipoles to be reduced, when $\boldsymbol{M}$ diverges and a demagnetizing field is created to fill the space. The result is a cost in energy of $B^2/2\mu_o$ [27]. The magnetostatic energy reaches a minimum when no net magnetization vector is measurable from the bulk material. The magnetostatic energy is at a maximum value when the core becomes saturated. To reduce this energy, the magnetization diverges and a domain wall is created. However, the creation and maintaining of a domain wall requires energy. A balance is therefore reached between the lowering of the magnetostatic energy and the creation of a domain wall.

Inside a given domain the dipoles themselves are aligned as the result of what is known as the exchange energy [27]. This causes an electrostatic coupling between dipoles that makes it more energetically favorable for them to align toward the direction of the applied magnetic field. This is primary reason for preferred alignment of the magnetic dipole moments inside a given domain. This exchange energy between neighboring magnetic dipole moments is much stronger than the magnetostatic energy, but the magnetostatic energy becomes more significant for dipoles separated by large distances [22].

It is also quite common for a material to have directions in the crystal structure that makes it energetically more favorable for the magnetic dipole moment to align

toward a specific direction [22]. Such crystallographic directions are known as the easy axis of magnetization. To contrast this, there are also crystallographic directions that are move difficult to magnetize termed hard axis. This means that a larger magnitude of $\boldsymbol{M}$ will occur when the applied field is in the direction of the easy axis. The energy required to make the net magnetization point in a direction not aligned toward the easy axis is called the anisotropy energy.

When the magnetostatic energy is lowered by the creation of a magnetic domain wall, the energy is spent in terms of exchange energy and anisotropy energy. At the domain wall boundary, the exchange energy and anisotropy energy are at equilibrium. This causes a finite transition region from one domain to the next. The length of this region is often approximated by setting a mathematical expression of the anisotropy energy to a mathematical expression of the exchange energy. The distance is then found by minimization of both energy terms.

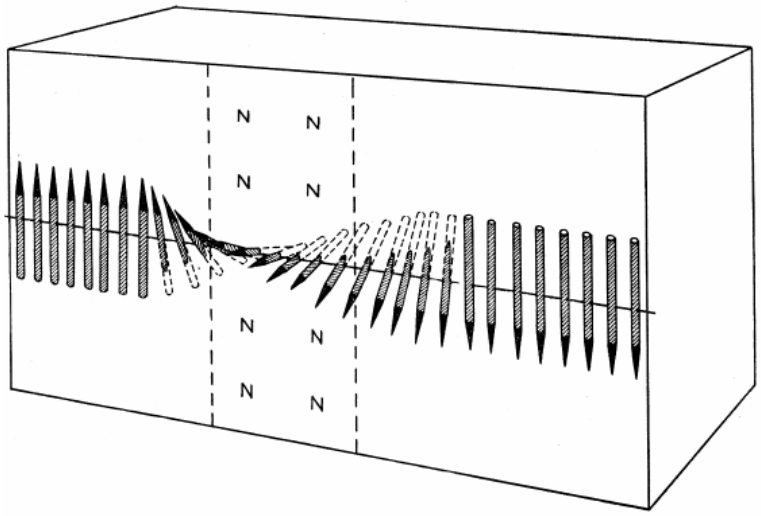

Figure 2.7 Schematic of the transition region between two domains. This specific type of domain wall configuration is known as a Bloch wall. The energy balance is maintained by a competition between the anisotropy and exchange energy.

Figure copied from [18].

The texture of a material takes advantage of a material's microstructure. The overall effect in terms of the microstructure is shown in Figure 2.9. A material becomes textured due to the alignment of its grains. Several magnetic domains may occupy a given grain.

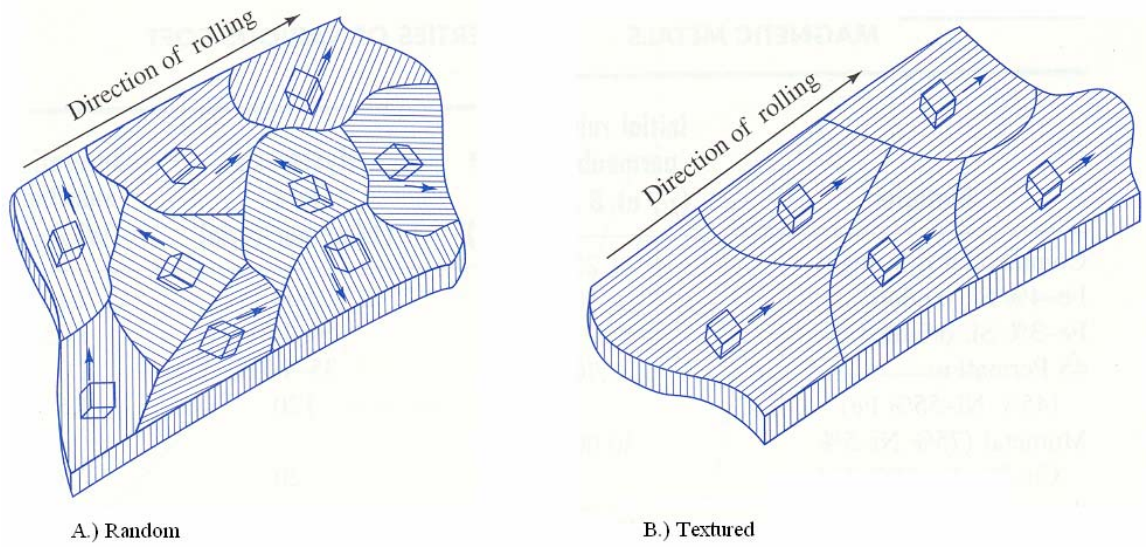

Figure 2.8 Polycrystalline iron-silicon sheets. The textured sheet is the result of cold rolling with the small cubes representing the orientation of the unit cell.

Figure copied from [30].

From the perspective of the magnetization of the material, this causes the easy axis in each crystal to be aligned. The net effect is that the there is a given distribution of domains pointing toward the same set of easy axes [31]. When this occurs, the average energy required energy to rotate a moment to its easy axis is less. For modeling purposes, texture and anisotropy are treated together as will be shown later in this chapter.

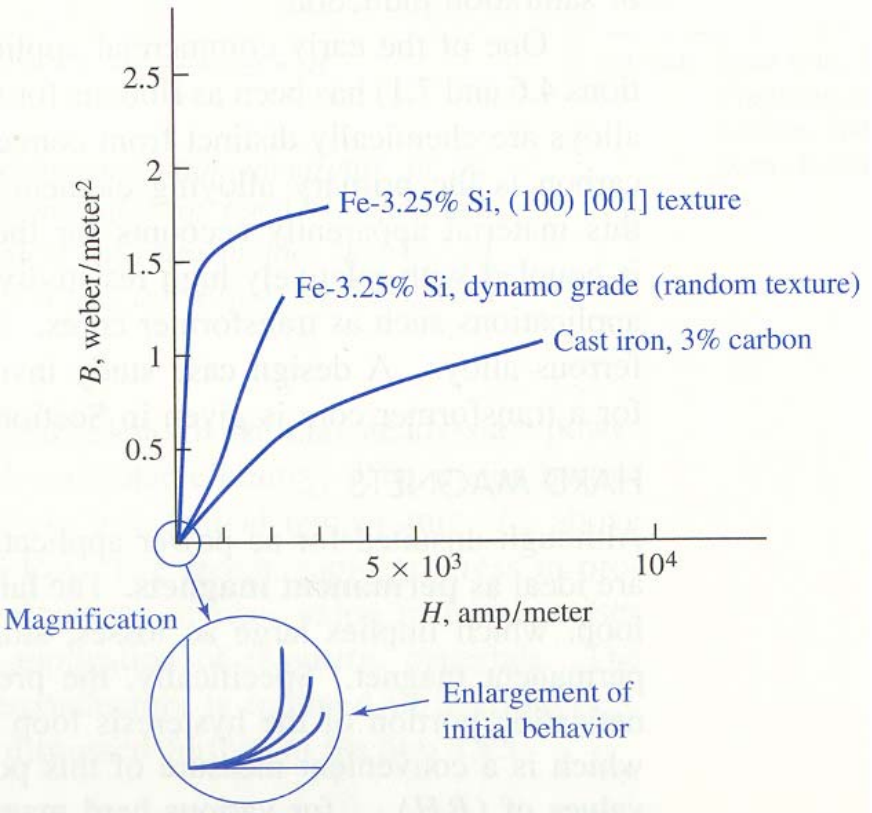

Figure 2.9 Influence of texture on the ***B*-*H*** characteristics of silicon iron. The texturing of the material aligns the easy axis toward a single direction. Less energy is then required to rotate the magnetic domains toward the easy axis. The resulting ***B*** increases at a much higher rate with the applied ***H***.

Figure copied from [30].

In summarizing and showing the formation of domains due to the minimization of the magnetostatic energy, we will rely on Figure 2.23 from the work of [18]. From Figure 2.2 (a) the magnetostatic energy is at its maximum value. There is no energy spent in creating magnetic domains. The material is in a saturated state.

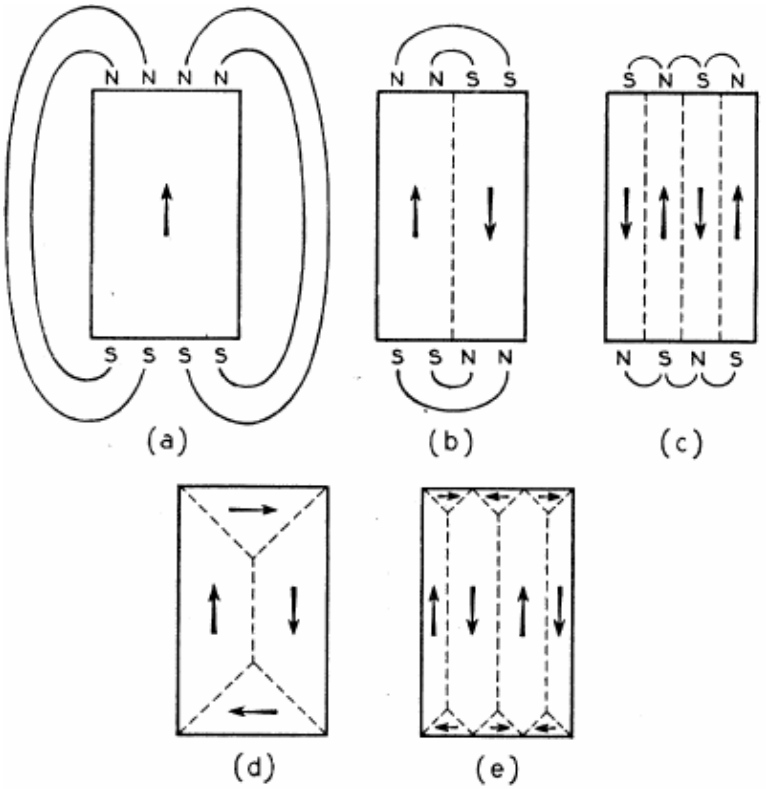

Figure 2.10 Schematic of the formation of magnetic domains in a single crystal ferromagnetic crystal. The process is governed by the minimization of three primary energy terms. They are the magnetostatic energy, exchange energy, and anisotropy energy.

Figure copied from [18].

Figure 2.11(b) the magnetostatic energy is lowered by creating and maintaining a domain wall. Figure 2.11(c) it is energetically favorable for the total domain configuration to subdivide again to lower the magnetostatic energy and create more domain walls. The reduction in magnetostatic energy compared to the saturated condition is approximately 1/N where N is the number of domain walls. Figure 2.11(d) the magnetostatic energy continues to lower and closure domains begin to form. The magnetic dipole moments have aligned normal to the surface and the net ***M*** over the volume begins to approach

zero. Figure 2.11(e) the magnetostatic energy, exchange energy, and anisotropy energy are balanced and have reached equilibrium. No external ***M*** is present from the material, and the material is in the demagnetized state.

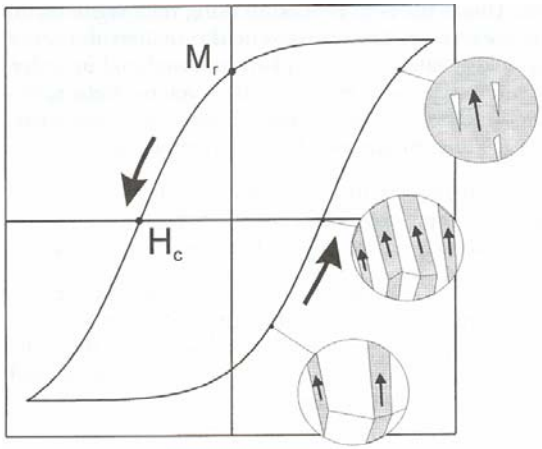

Figure 2.11 Magnetic domain structure changing as a result of the applied field. The domain structure is altered as energy is spent and minimized by creating and maintaining the boundaries between magnetic domains.

Figure copied from [29].

When an external magnetic field is applied to the material, the magnetostatic energy is altered [18], and the magnetic domain structure moves in response to the applied field. This change is averaged over the volume and seen as a change in the ***B-H*** loop is shown in Figure 2.12.

The domain wall can be envisioned as having a surface tension like that of a liquid [19]. When the wall moves it can become pinned to a defect(s) and its shape deforms by bowing. Domain walls with a high surface tension move as rigid walls. This can occur in highly pure materials where the probability of encountering a defect is much less. For more realistic types of materials with defects, the movement of domain walls is

impeded by defects in the material. The overall effect averaged over the volume is that defects cause an energy loss in the material and prevent the material from reaching its true equilibrium state known as the anhysteretic magnetization. The combination of the exchange energy, anisotropy energy, thermal energy, and magnetostatic energy along with the defects in the material create a random potential where a multitude of metastable states exist [29]. Such a series of states is seen by a domain in balancing the forces upon it. When a domain structure is placed in a given energy state by an applied field, it is surrounded by a large energy well as shown in Figure 2.12.

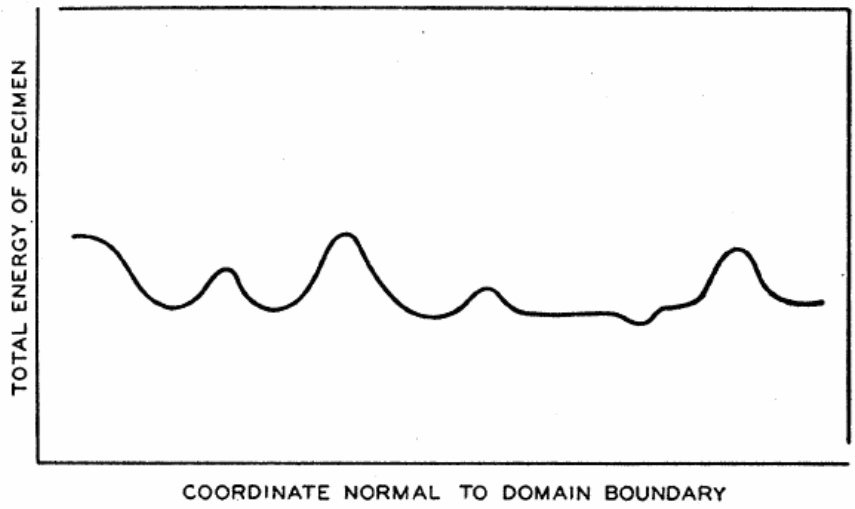

Figure 2.12 Example of a random potential seen by a magnetic domain. This random potential causes fluctuations in the domain walls which randomizes the net motion of the domains under the application of an external magnetic field.

Figure copied from [18].

The domain structure will remain in its present metastable state depending on the height of the energy barriers present, the energy provided by the environment, and the energy provided by the applied $\boldsymbol{H}$ as a function of time. When $\boldsymbol{H}$ is applied the local

minimum is transformed into a saddle point, and the domain structure is abruptly transformed into a new stable configuration. In the process, the system releases energy form of heat. Such a reaction by the domain structure is called a Barkhausen jump [29]. If the domain structure is left unperturbed for a period of time, thermal fluctuations to the domain structure can overcome the surrounding energy barriers and cause a Barkhausen jump. This is known as a thermally activated Barkhausen jump.[29] Because of the depth of some potential wells and the number of wells present in the material, a given structure may exist for an extremely long time. However, it should be noted that the natural Barkhausen jumps occur as the system approaches true thermodynamic equilibrium. When a given ***M-H*** loop is formed, the same domain structure is not repeatedly formed. Instead, the ***M-H*** loop is formed by an average over the volume. The presence of metastability in forming a domain structure shows how the history of ***M*** influences the magnitude of ***M*** [29].

2.2. Theory of Ferromagnetic Hysteresis

One theory of ferromagnetic hysteresis is the Jiles-Atherton model and is implemented in many simulation tools such as PSpice. When first postulated, the model's purpose was the development of an equation of state to describe the ***M-H*** relationship and therefore the ***B-H*** characteristics of a given magnetic material which would, in principle, be easy to apply with a limited number of extractable parameters [16].

The model can be divided into two key components. This section will begin with a brief description of both components followed by a detailed discussion of each

component. The anhysteretic magnetization, $M_{an}(H)$, is a single valued function representing the global equilibrium points on the ***M-H*** plane [16]. In this way the anhysteretic magnetization is thought of as the thermodynamic equilibrium curve of a given magnetic material. Another theory expounded upon by Jiles and Atherton is that the anhysteretic magnetization is the ideal magnetization curve that would occur if the material were free from defects. In this theory, defects were the cause of hysteresis in real magnetic materials. The anhysteretic magnetization would then represent the ***M-H*** relationship that would occur in an ideal defect free material. The theory of ferromagnetic hysteresis uses the anhysteretic magnetization to predict the present value of ***M(H)*** as an offset from the ideal anhysteretic magnetization [16]. In order to understand the Jiles-Atherton model, which is the theoretical basis for this dissertation research, we must first begin with a discussion of the anhysteretic magnetization.

2.2.1. The Anhysteretic Magnetization, $M_{an}(H)$

In this section, a development of $M_{an}(H)$ will be discussed. How Jiles and Atherton adapted $M_{an}(H)$ for predicting the present value of M will be discussed in the next section.

Before a correct interpretation of the exchange energy was provided by Heisenberg, it was postulated by Weiss that a molecular field existed in which electrons applied a force on each other in order to align themselves [19]. The term Weiss mean field was used to describe the average field that was experienced by a magnetic dipole moment. It was found that this force was of significant magnitude that it could overcome

the thermal agitation that existed in a real material and cause long range order to be present such as that seen inside a single domain.

In forming an equation of state for magnetic domains, Jiles and Atherton adopted the idea of an average field interaction between magnetic domains to describe how the domains react to one another. Normally, an average field interaction is used to calculate the dipolar field experienced between magnetic moments and the concept is not applied to magnetic domains. This resulted in an effective applied field, $\boldsymbol{H_e}$, [16]

$$\boldsymbol{H}_e = \boldsymbol{H} + \alpha \boldsymbol{M} \tag{2.12}$$

where α is the mean field parameter describing the inter-domain coupling and is determined experimentally. With this assumption, Jiles and Atherton stated that the energy of a magnetic domain per unit volume is given by [16]

$$E(\theta) = -\mu_o \boldsymbol{m} \cdot \boldsymbol{H}_e \tag{2.13}$$

where $\boldsymbol{m}$ is the magnetic moment per unit volume of a typical domain and is analogous to the energy of a single moment. The Langevin function was then used to mathematically estimate the probability that a magnetic domain would occupy a given energy state in an isotropic medium given the effective coupling α. The modified Langevin equation took the form [32]

$$M_{an} = M_s L\left(\frac{\mathrm{E}(\theta)}{\mathrm{k_B T}}\right) \tag{2.14}$$

where L is the Langevin function, M_s is the saturation magnetization and $E(\theta)$ is the energy of typical domain given as [32]

$$E(\theta) = -\mu_o < \boldsymbol{m} > \cdot(\boldsymbol{H} + \alpha \boldsymbol{M}) \tag{2.15}$$

where

$$< \boldsymbol{m} >= \frac{k_B T}{\mu_o a} \tag{2.16}$$

is the magnetic moment of a typical magnetic domain, k_B, is Boltzmann's constant, T is the ambient temperature, and a characterizes the shape of the anhysteretic magnetization curve and is determined experimentally [16]. The model of $M_{an}(H)$ would represent the ***M-H*** relationship that would occur if no defects were present in an isotropic magnetic material with dipolar coupling. This is why the anhysteretic magnetization curve is often referred to as the ideal magnetization of the core.

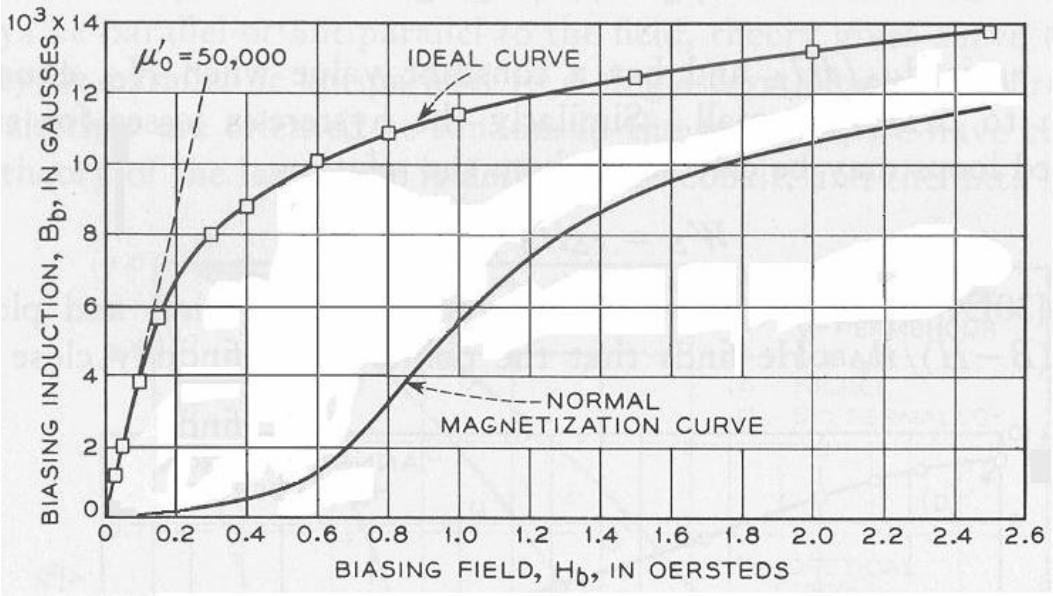

Figure 2.13 Original experimental data by Bozorth showing a methodology to measure the ideal magnetization curve $M_{an}(H)$. The normal (initial) magnetization curve is plotted for comparison.

Figure copied from [33].

It was noted by Jiles and Atherton that the modified Langevin equation was valid only for isotropic materials as the energy E of a magnetic domain depended only on a single angle θ between the magnetic domain and the applied $\boldsymbol{H}$ which was already stated to be $E = -\mu_o \boldsymbol{m} \cdot \boldsymbol{H}_e$ [16].

In other materials such as ferrites, the material cannot be considered isotropic. Work began after the original model to find alternate expressions for $M_{an}(H)$ based upon the type of anisotropy in the material. As an example, an expression for $M_{an}(H)$ based upon uniaxial anisotropy was developed. In Figure 2.15 the magnetic moment of the two domains are shown as m_1 and m_2. The energy of each domain depends on the angle formed between the domain and the applied field, θ, and also the angle formed between $\boldsymbol{H}$ and the unique axis, ψ. The unique axis can be either an easy axis or a hard axis and depends on the model parameters for this specific model of $M_{an}(H)$.

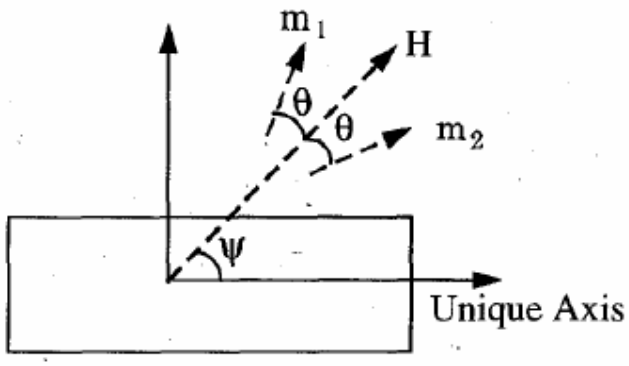

Figure 2.14 Representation of uniaxial anisotropy showing the vector representation of the resulting magnetic domain's magnetic moment, the applied field and the unique axis of the crystal.

Figure copied from [32].

When the Jiles-Atherton model was applied to magnetic cores with high levels of anisotropy without a proper model of the anhysteretic magnetization, the entire model lost accuracy [34]. Results reported for the application of the model with a hard magnetic material, $Nd_2Fe_{14}B$, verified this observation. Deviations of 10% to 20% were found between the predicted and measured ***B-H*** curves as shown in Figure 2.16 and Figure 2.17 [34].

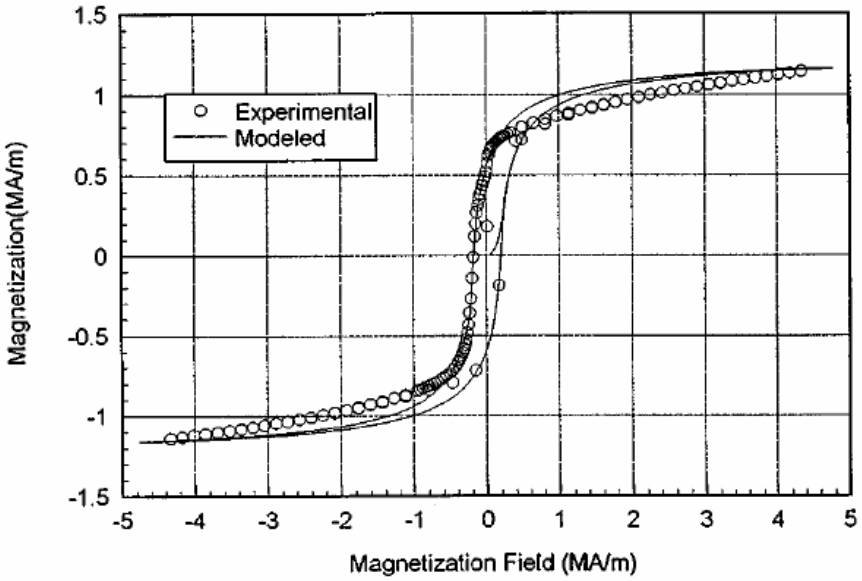

Figure 2.15 Comparison of experimental and modeled ***M-H*** loops. Error was introduced by using the modified Langevin equation to predict the ***M-H*** relationship in a material with a higher level of anisotropy.

Figure copied from [34].

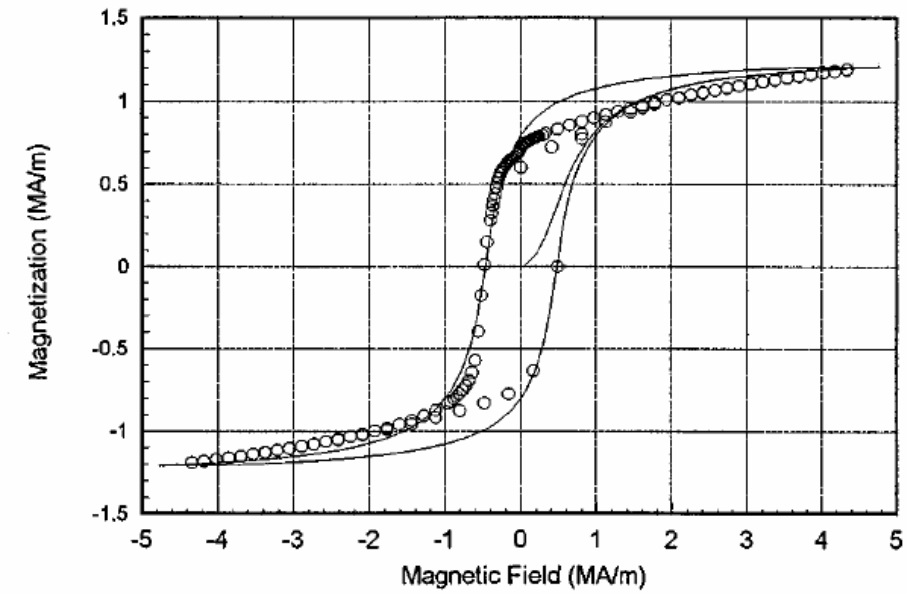

Figure 2.16 Errors in the predicted and measured ***B-H*** loops due to a poor model of $M_{an}(H)$. The circles represent the measured data and the line is the modeled ***M-H*** loop.

Figure copied from [34].

Further work was required to create models for the anhysteretic magnetization for materials with other types of anisotropy so that they can be properly modeled with the Jiles-Atherton model. It was found that the texture of a magnetic material like that shown in Figure 2.9 could be included in the Jiles-Atherton model by again altering the model of the anhysteretic magnetization [31]. It was concluded that both texture and anisotropy could be used as input parameters to model a magnetic material's anhysteretic magnetization [31].

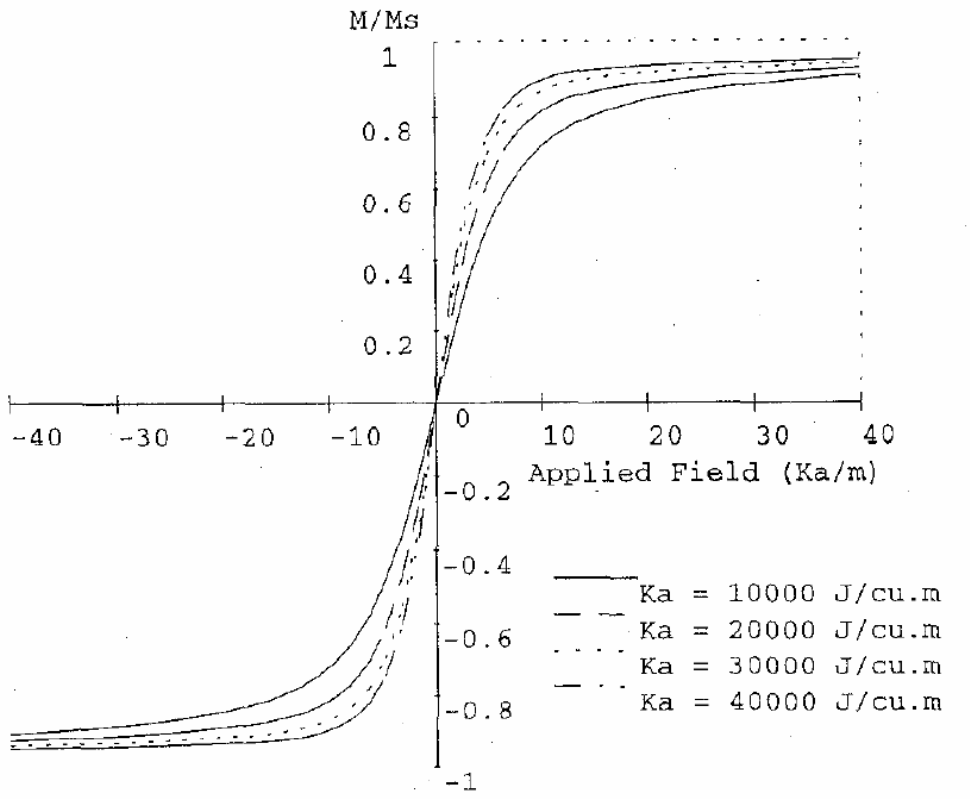

Figure 2.17 Predicted curves for $M_{an}(H)$ for uniaxial anisotropy. The anisotropy in the model is characterized by the anisotropy constant *Ka* and the parameter

Figure copied from[32].

In modeling $M_{an}(H)$ for commercially available magnetic cores, the type of anisotropy and texture are generally unknown. Furthermore, a common material can be listed under a trade name making it more difficult to identify. Technical data from the manufacturer does not provide any useful information concerning this subject. Thus, on a practical level, some type of test must be performed to properly model $M_{an}(H)$ for the purpose of achieving an accurate higher level circuit model. This need forms a substantial basis of this dissertation research.

Furthermore, the anhysteretic magnetization curve has a definite temperature dependence as the curve itself can be understood as representing a collection of thermal equilibrium states [29]. Jiles later work on the extraction of experimental parameters and in particular, a for the model described the parameter a as a form factor for $M_{an}(H)$ with a clear temperature dependence. He noted that the parameter a does not seem to represent the Boltzmann energy k_BT [35]. Therefore, the explicit temperature dependence from the modified Langevin equation is not correct. The work of Wilson showed this by curve fitting the parameter a as a function of temperature to the modified Langevin equation [36]. If the temperature dependence of $M_{an}(H)$ is not accounted for in the modeling process, a systematic error will occur for a given change in core temperature. This is similar to the error measured when the modified Langevin equation was applied to materials with higher levels of anisotropy. This is because the total magnetization, $M(H)$, is predicted as an offset from $M_{an}(H)$. When the temperature of the material changes, the initial point where the offset is predicted will change.

To overcome these challenges in the modeling process, and to provide for a correct and precise mathematical model for $M_{an}(H)$ for a commercially available magnetic core, an automated test system was constructed to measure $M_{an}(H)$ as a function of temperature which will be described in Chapter 3. This system resolves several difficulties. It removes the difficulty of properly identifying the correct $M_{an}(H)$based upon the anisotropy and texture of the core material. This allows custom cores to be used and does not limit the material type in the design process. It circumvents the need for complex models of $M_{an}(H)$, which could possibly differ in real materials due to defects. The system also allows for the prediction of a precise temperature dependence to of $M_{an}(H)$. Finally measured data can be

used as experimental validation of $M_{an}(H)$ to confirm its accuracy. The construction of this system and its experimental data is the subject of Chapter 3.

2.2.2. The Theory of Ferromagnetic Hysteresis

The domain mechanics modeled by Jiles and Atherton is the second component of the Jiles-Atherton model. The derivation of their theory begins with the total work done per volume by a magnetic field. However, some related energy terms that are derived from the Poynting Theorem [29] are not present in the derivation in the original paper that would require certain assumptions. The energy loss due to eddy-currents has been neglected with the assumption that the present model is valid for low frequencies. This derivation of the original model will follow with one that shows how temperature and frequency dependent effects can be included.

The following original theory by Jiles and Atherton begins by considering the work done on a volume of material by a magnetic field [16].

$$E = \int_0^B HdB = \frac{1}{\mu_o}\int_0^B BdB + \int_0^B MdB \tag{2.17}$$

where

$$E = \int_0^B HdB \tag{2.18}$$

is the work done on the sample by the externally applied field $\boldsymbol{H}$.

The two terms on the right hand side of equation (2.17) are

$$\frac{1}{\mu_o}\int_0^B BdB$$

which is the work done on the environment and

$$\int_0^B MdB$$

which is the work done on the sample.

In the Theory of Ferromagnetic Hysteresis, the fields are considered effective fields following the form of the previous section so that $H_e = H + \alpha M$ [16]. Using this relationship the work done on the sample with no defects would be equal to the work done by $M_{an}(H)$. The magnetization, $M(H)$**,** would then be given by $M_{an}(H)$ for a material with no defects. This means that the work done on the same volume is equal to the work done by $M_{an}(H_e)$ given by [16]

$$\int_0^{Be} MdB_e = \int_0^{Be} M_{an}(H_e)dB_e \tag{2.19}$$

For real materials, defects can cause irreversible changes. Jiles and Atherton highlighted the work of Globus [16] in their original work in noting that irreversible changes in $M(H)$ are caused when domain walls become pinned by defects. Recall that it is the domain wall that is considered to move as the result of the applied field due to the delicate energy balance being maintained. The model is not concerned with the underlying physics of each type of defect present in the material as the purpose is to predict the *M-H* relationship, so the model then makes the assumption that all defects can be treated equally and are collectively referred to as pinning sites [16]. This allows the extraction of a single parameter, k, referred to as the pinning constant for the model.

Consider two magnetic domains. One has a magnetic moments per unit volume $\boldsymbol{m}$ aligned toward $\boldsymbol{H}$ and another with magnetic moment per unit volume $\boldsymbol{m}'$ aligned at some arbitrary angle to $\boldsymbol{H}$. Assume that a defect is located on the wall so that the wall that separates these two domains is pinned. The energy required to overcome this

pinning site is proportional to the change in energy per unit volume of $\boldsymbol{m}'$ caused by rotating the net moment $\boldsymbol{m}'$ given by [16]

$$\Delta E = m \cdot B_e - m' \cdot B_e \tag{2.20}$$

Jiles and Atherton point out that the energy to rotate the domain is a function of the pinning site itself [16]. This means that the energy related to the pinning site, ε_{pin}, is proportional to the change in energy [16] which is given as

$$\varepsilon_{pin} \propto mB_e(1-\cos\theta) \tag{2.21}$$

where θ is the angle formed between $\boldsymbol{m}'$ and $\boldsymbol{H}$. We will consider a domain wall where the magnetization is pointing in the opposite direction on the other side of the wall. If the pinning energy for a 180° domain wall is ε_π and ε_π is proportional to $2mB_e$, then the pinning energy can be specified in terms of ε_π. Adjacent magnetic domains separated by a domain wall often point 180° in the opposite direction as shown in

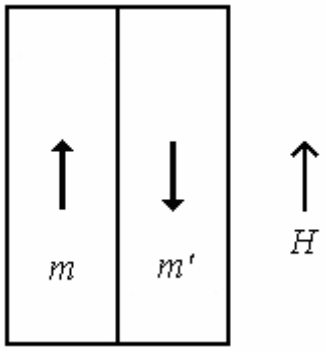

Figure 2.18 Two domains with magnetic moments m and m'. m is aligned with *H* and m' is aligned 180° from *H*.

If the wall is not 180°, the extracted parameter governing the pinning process will reflect this. Now the average pinning energy can be placed in terms of the pinning site [16]

$$< \varepsilon_{pin} >= \frac{1}{2} < \varepsilon_{\pi} > (1 - \cos\theta) \tag{2.22}$$

When a domain wall moves, the magnetic moment per unit volume $\boldsymbol{m'}$ is reduced. **m** by symmetry is increased. If the domain wall has an area, A, that is moved by a distance, x then it follows that the total energy lost by the pinning site is [16]

$$E_{pin}(x) = \int_{0}^{x} \frac{n < \varepsilon_{pin} >}{2} (1 - \cos\theta) A \mathrm{dx} \tag{2.23}$$

where n is the average density of defect sites throughout the material. The magnetic domain with magnetic moment per unit volume $\boldsymbol{m}$ increases as the domain wall moves. The increased area will be equal to the area lost by the magnetic domain with magnetic moment per unit volume $\boldsymbol{m'}$. Because the magnetic moment per unit volume $\boldsymbol{m}$ already points in the direction of the applied field, it follows that the change in $\boldsymbol{M(H)}$ is [16]

$$dM = m(1 - \cos\theta) A \mathrm{dx} \tag{2.24}$$

Substituting into the total energy lost from pinning yields a relationship for total pinning lost in terms of the magnetization, $\boldsymbol{M(H)}$ [16]

$$E_{pin}(M) = \frac{n < \varepsilon_{\pi} >}{2\boldsymbol{m}} \int_{0}^{M} \mathrm{d}\boldsymbol{M} \tag{2.25}$$

where

$$k = \frac{n < \varepsilon_{\pi} >}{2\boldsymbol{m}} \tag{2.26}$$

is put in terms of the model parameter k that is determined experimentally. The equation for hysteresis may now take a more realistic form consisting of an ideal component,

M_{an}(H) and an irreversible loss term due to the pinning of rigid domain walls by defects [16].

$$\int_0^{Be} M dB_e = \int_0^{B_e} M_{an}(H_e) dB_e - k\int_0^{Be} \frac{dM}{dB_e} dB_e \tag{2.27}$$

Here the work done per unit volume is equal to the ideal lossless case minus the hysteresis loss. Differentiating with respect to $\boldsymbol{B_e}$ yields the basic equation of state for a ferromagnetic material [16]

$$M(B_e) = M_{an}(B_e) - \delta k\left(\frac{dM}{dB_e}\right) \tag{2.28}$$

The present value of M depends on the ideal value minus some offset from the ideal value caused by loss. In its present form the equation is of limited use as the equation is really in terms of its natural output $\boldsymbol{B_e}$. The equation can be placed in terms of its natural input and response using [16]

$$\boldsymbol{B_e} = \mu_o(\boldsymbol{H} + \alpha \boldsymbol{M}(\boldsymbol{H}))$$

This yields an irreversible component of the magnetization given originally as [16]

$$\frac{dM_{irr}(H)}{dH} = \frac{M_{an}(H) - M_{irr}(H)}{\delta k / \mu_o - \alpha(M_{an}(H) - M_{irr}(H))} \tag{2.29}$$

where δ becomes -1 when $\boldsymbol{H}$ is decreasing and +1 when $\boldsymbol{H}$ is increasing. In later years, the k parameter was redefined in terms of A/m and the permeability of free space μ_o removed.

The reversible component of magnetization results when the domain wall bulges, and then returns to its shape once the applied field is removed. In considering the

reversible component of the magnetization, the pinning of a domain wall between two pinning sites was considered.

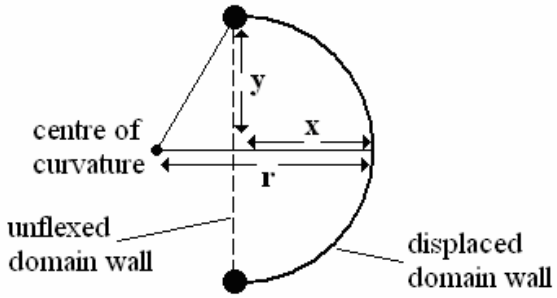

Figure 2.19 Pinning of domain wall by two pinning sites. The wall bows in a reversible fashion and returns to its original position.

Adapted from [16].

The pressure, P, exerted on the wall by the applied field is related to the surface energy, *E*, by [16]

$$P = \frac{2E}{r} \tag{2.30}$$

If the geometry of Figure 2.20 is used, the x-coordinate can be placed in terms of the radius and y-coordinate. Once substituted into the expression for wall pressure, the x coordinate takes the following form [16].

$$x = \frac{2E}{P} - \sqrt{\left(\frac{2E}{P}\right)^2 - y^2} \tag{2.31}$$

When the pressure applied by *H* is small, the displacement shown in Figure 2.20 can approximated by the first terms of the binomial expansion so that [16]

$$\mathrm{x} \approx \frac{1}{2}\frac{\mathrm{y}^2 P}{2E} \tag{2.32}$$

The ferromagnetic material applies a resulting force so that the effective magnetostatic energy is proportional to [16]

$$E \propto \frac{1}{2}(M_{rev}(H) - M_{an}(H))^2 \tag{2.33}$$

So that the force on the domain walls is

$$F \propto (M_{an}(H) - M_{rev}(H)) \tag{2.34}$$

The pressure on the domain walls is then specified by the constant C'.

$$P = C'(M_{an}(H) - M_{rev}(H)) \tag{2.35}$$

Substituting P into the binomial approximation for x yields an expression for the bowing of a domain wall [16]

$$x = \left(\frac{y^2}{4E}\right)\boldsymbol{C'}\left(M_{an}(H) - M_{rev}(H)\right) \tag{2.36}$$

It is now assumed that the volume swept out by M_{rev} is given the work of Globus and Duplex [16]

$$\Delta V\left(\frac{\pi}{6}\right)x\left(3y^2 + x^2\right) \tag{2.37}$$

and the change in the reversible component of magnetization is $M_{rev}(H)=2\Delta Vm$ for two parallel or antiparallel domains. The total reversible component of magnetization is then given by [16]

$$M_{rev}(H) = \frac{m\pi\pi y4\,C'}{4E}\left(M_{an}(H) - M(H)\right) + m\frac{\pi}{3}\left(\frac{y^2}{4E}C'(M_{an}(H) - M(H)\right)^3 \tag{2.38}$$

The higher order terms were neglected in the model again following the analysis performed by Globus. The lower order term was given the coefficient [16]

$$c = \frac{\text{m}\pi\pi\text{y4C}'}{\text{4E}} \tag{2.39}$$

which again is determined experimentally and describes the reversible component of magnetization which is now written [16]

$$M_{rev}(H) = c(M_{an}(H) - M_{rev}(H)) \tag{2.40}$$

We finally arrive at the goal of Jiles and Atherton – a single equation for *M(H)* which is the addition of the irreversible and reversible components [16].

$$M(H) = M_{irr}(H) + M_{rev}(H) \tag{2.41}$$

Now that the basic mechanics of the Jiles-Atherton model have been discussed including the anhysteretic magnetization and the equation of state, we are ready to delve into temperature and frequency dependent effects. From the viewpoint of the anhysteretic magnetization, the equation as-is lacks a basic temperature dependence. In fact from the viewpoint of the mechanics of the model, no temperature dependence exists. The discussion now turns toward the primary goal of the present research in adding temperature dependence to the present model.

2.3. Static and Dynamic Temperature Modeling

In the present equation, the work done on a given magnetic sample equals the ideal case minus the loss and was given by [16]

$$\int_0^{Be} M_{irr}\,dB_e = \int_0^{Be} M_{an}(H_e)\,dB_e - k\int_0^{Be} \frac{dM_{irr}}{dB_e}\,dB_e$$

Yet as the first law of thermodynamics states, the change in internal energy equals the work done on the system plus the heat absorbed by it [29]

$$dU = \delta L + \delta Q \tag{2.42}$$

where δQ is the heat absorbed by the system. If one makes the wrong assumption that the hysteresis loss governed by k, is only a result in the change in internal energy, the heat flux dQ/dt will provide an additional offset from the anhysteretic magnetization curve. This is not the case. The dynamic experiments presented in Chapter 4 show that there is no change in the ***B-H*** characteristics of a magnetic core due to heat flux being present. Thus, the thermodynamic ***B-H*** characteristics can be quantified using the present temperature of the core.

Theoretically if that were not true then the following derivation shows how such a heat flux would change the width of a measured ***M-H*** loop. Accounting for the work terms in the previous equation shows that the change in internal energy is given by

$$dU = \int_0^{Be} M_{an}(H_e)dB_e - k\int_0^{Be} \frac{dM_{irr}}{dB_e} dB_e \tag{2.43}$$

With the work done on the sample given by

$$\delta L = \int_0^{Be} M_{irr} dB_e \tag{2.44}$$

For the irreversible component of magnetization shown above, the work done by the environment is added so that the irreversible component becomes

$$\int_0^{Be} M_{irr} dB_e = \int_0^{Be} M_{an}(H_e)dB_e - k\int_0^{Be} \frac{dM_{irr}}{dB_e} dB_e - \delta Q \tag{2.45}$$

where δQ represents the energy loss as the work performed on the sample by the environment. Similar to the analysis performed before, the equation is differentiated with respect to $\boldsymbol{B_e}$ and the heat term is specified only by Q. This assumes the heat is not from the pinning loss in the material, which is not true. In doing so, the equation of state takes the following form.

$$M_{irr}(B_e) = M_{an}(B_e) - \delta k\left(\frac{dM_{irr}}{dB_e}\right) - \frac{dQ}{dB_e} \tag{2.46}$$

Now, the new equation of state must be placed in terms of *M* and *H*. This has been done before for the term involving pinning as it has been done before and must be done for the term involving heat.

$$\frac{dQ}{dB_e} = \frac{\left(\frac{dQ}{dt}\right)}{\left(\frac{dB_e}{dt}\right)}$$

Given again that

$$B_e = \mu_o(H + \alpha M(H))$$

a substitution is made for $\left(\frac{dB_e}{dt}\right)$ can be formed based upon the assumption that the heat loss in the core is not caused by pinning. The dynamic experiments in Chapter 4 show this is not true, so that *M(H)* can be modeled only as a function of the materials temperature.

$$\frac{dM_{irr}(H,t,Q)}{dH} = \frac{M_{an}(H) - M_{irr}(H,t,Q)}{\delta k/\mu_o - \alpha(M_{an}(H) - M_{irr}(H,t,Q))} - \frac{\left(\frac{dQ}{dt}\right)}{\mu_o\left(\frac{dH(t)}{dt}\right) + \mu_o\alpha\left(\frac{dM_{irr}(H,t,Q)}{dt}\right)} \tag{2.47}$$

Here the term $\frac{dQ}{dt}$ represents the diffusion of heat into the material, and would provide a natural coupling to the heat equation if the hysteresis loss were not responsible for the self-heating and energy loss of the sample. For thermodynamic equilibrium, the $M_{irr}(H)$ component again predicts the magnetization as an offset from $M_{an}(H)$ and the

equation obtains its static form. A solution of $\frac{dQ}{dt}$ is met by solving the diffusion equation given as [37]

$$\frac{dQ}{dt} = \lambda(t)\nabla^2 q \tag{2.48}$$

where λ is the diffusivity specified as

$$\lambda = \frac{k}{\rho c} \tag{2.49}$$

and k is the thermal conductivity, ρ is the density of the material, and c is the specific heat [37].

One must realize that if equation 2.48 were true, then an additional offset from the anhysteretic magnetization curve would occur when a heat flux is present. Because this is not true, the temperature dependence of $M_{an}(H)$ governs the core's behavior, and is itself a function of temperature. Recall also that $M_{an}(H)$ has a functional dependence on the anisotropy and texture of a given material, and recognize that no accurate temperature dependence is present in the many $M_{an}(H)$ equations. For instance, it is known experimentally that the pinning coefficient k that governs the loss for the irreversible component has a function of temperature. This is not a dynamic case, but a static case or rather a thermodynamic equilibrium case. In fact, all of the parameters have a static temperature dependence, which can be found experimentally. This was shown by Wilson, who previously curve fitted the parameters of the model as a function of temperature. In doing so, the modified Langevin equation was assumed, meaning the material was assumed to be highly isotropic [36]. To model the anhysteretic magnetization correctly, an automated test system was constructed to plot $M_{an}(H,T)$ as a

function of temperature. The system is also capable of plotting ***B-H*** loops as a function of temperature, which is required for the parameter extraction in the model. The following Chapter will discuss the experimental component of this research and how the required experimental data was obtained. But first a discussion of the frequency-dependent modeling component is provided to conclude this theoretical Chapter.

2.4. Frequency Dependent Model

The previous expression involving the energy supplied to a material was given as

$$E = \int_0^{Be} H dB_e = \frac{1}{\mu_o}\int_0^{Be} B dB_e + \int_0^{Be} M dB_e$$

which is a consequence of the Poynting Theorem. In assuming that the total energy supplied to the field was

$$\int_0^{Be} M_{irr} dB_e$$

it was an inferred assumption that the eddy-current distribution within the material was negligible. At higher frequencies this is clearly not true. To correct this problem, Jiles on a later paper applied the classical equation for instantaneous power loss per unit volume due to of eddy currents given as [17]

$$\frac{dW_{EC}}{dt} = \frac{d^2}{2\rho\beta}\left(\frac{dB}{dt}\right)^2 = \frac{\mu_0^2 d^2}{2\rho\beta}\left(\frac{dM}{dt}\right)^2 \tag{2.50}$$

where ρ is the material resistivity, d is the cross-sectional dimension of the core, β is a geometrical factor which varies for the type of sample. This loss component was simplified by the assumption of a sinusoidal excitation so that [17]

$$\frac{dW_{EC}}{dt} \approx \frac{\pi^2 B_{MAX}^2 d^2 f^2}{\rho\beta} \tag{2.51}$$

Such would not be the case in the application of power electronics. The classical anomalous loss term was also added to the total energy loss equation in the form of [17]

$$\frac{dWA}{dt} = \left(\frac{GdwH_o}{\rho}\right)^{\frac{1}{2}} \left(\frac{dB}{dt}\right)^{\frac{3}{2}} \tag{2.52}$$

This term results from the random reordering of the domain structure. G is a geometrical factor [29]. w is the width of the core laminations. d is the thickness of the core. ρ is the resistivity. H_o is a parameter representing the internal potential energy experienced by a domain wall. To add these terms to the model, Jiles first added the reversible and irreversible components together. Following this, the loss terms were added to the total magnetization. The expression was then differentiated again. Jiles reported the following result for the equation of state with these two loss terms [17]

$$\begin{aligned} &\left(\frac{\mu_o \boldsymbol{d}^2}{2\rho\beta}\frac{\boldsymbol{dH}}{\boldsymbol{dt}}\right)\left(\frac{\boldsymbol{dM}}{\boldsymbol{dH}}\right)^2 + \left(\frac{\mu_o \boldsymbol{GdwH}_o}{\rho}\right)^{\frac{1}{2}} \left(\frac{\boldsymbol{dH}}{\boldsymbol{dt}}\right)^{\frac{1}{2}} \left(\frac{\boldsymbol{dM}}{\boldsymbol{dH}}\right)^{\frac{3}{2}} \\ &+\left(\boldsymbol{k\delta} - \alpha\left(\boldsymbol{M}_{an} - \boldsymbol{M} + \boldsymbol{k\delta c}\frac{\boldsymbol{dM}_{an}}{\boldsymbol{dH}_e}\right)\right)\left(\frac{\boldsymbol{dM}}{\boldsymbol{dH}}\right) \\ &-\left(\boldsymbol{M}_{an} - \boldsymbol{M} + \boldsymbol{k\delta c}\frac{\boldsymbol{dM}_{an}}{\boldsymbol{dHe}}\right) = \boldsymbol{0} \end{aligned} \tag{2.53}$$

The equation was solved iteratively and could at most moderately predict the ***B-H*** relationship at higher frequencies. A sample of predicted and measured ***B-H*** loops is shown in Figure 2.21. It was noted that this model assumes a sinusoidal excitation, neglects the depth of penetration of the field into the material, and assumes that the domain structure can in fact return to thermodynamic equilibrium.

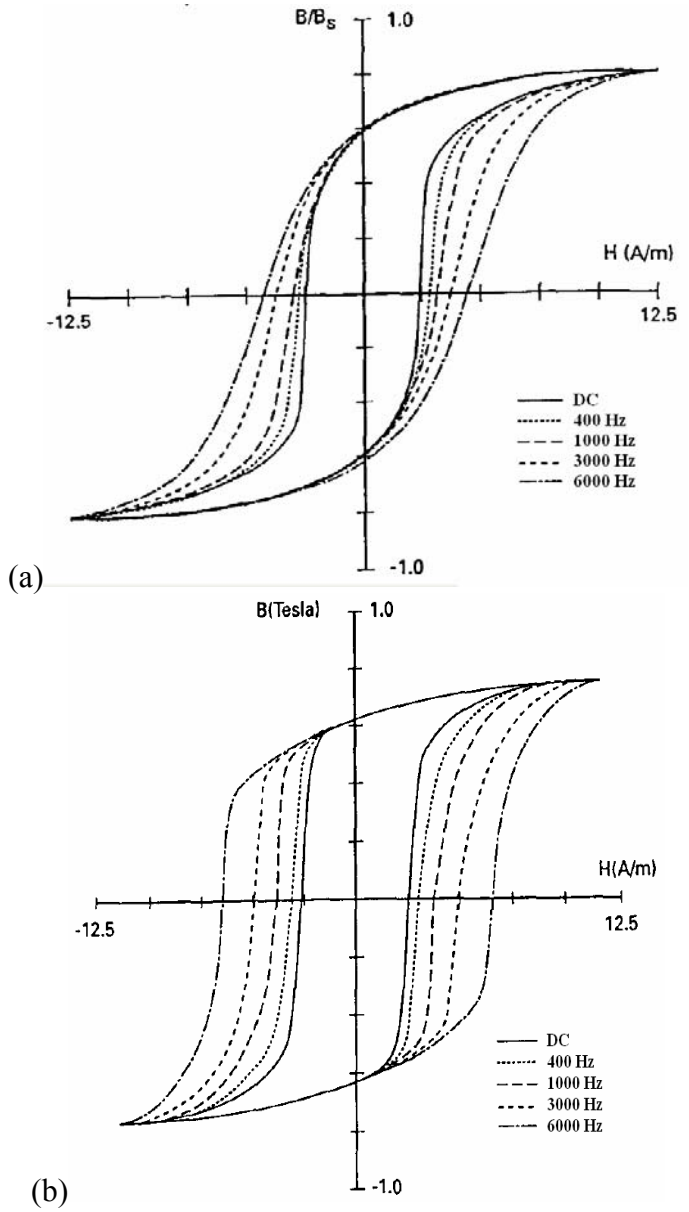

Figure 2.20 ***B-H*** curves for a permalloy 80 core as a function of frequency. (a) modeled performance and (b) measured performance. Note the large discrepancies between modeled and measured performance. Clearly a more accurate method to model frequency-dependent affects on such cores is needed and will be discussed in Chapter 3 of this dissertation.

Figures copied from [17].

For the ***B-H*** relationship to depend on the frequency of the applied field (i.e. rate), a change in magnetization occurs during a Barkhausen jump. If the jump is interrupted, then the material cannot return to its equilibrium state before another force is applied to it. In this simple terminology, the system cannot return to equilibrium. It is the belief of this author that this will result in an effective equilibrium state for a given frequency that can be verified experimentally.

From a macroscopic level, the equilibrium not only involves the competition of magnetostatic, anisotropy, exchange, and thermal energies but also the energy incurred in balancing the frequency dependent terms in steady state. Chapter 5 will entail the experimental component of this research that will verify this result by introducing higher frequency losses in the measurement of the core's anhysteretic magnetization. $M_{an}(H)$ will then become a function of both applied field, frequency, and temperature. It should also be noted that the loss due to heating must also be included with the frequency dependent loss terms.

In formulating a total equation for hysteresis as function of frequency, it should be noted, that investigations of loss in prior work have shown that higher frequency losses are seen as an increase in pinning energy [38]. As the frequency of the applied field increases, eddy-currents form around the domain wall boundary and effect the movement of the wall [29]. When the wall overcomes the additional force applied to it by the eddy-current distribution, this will be seen as increase in the pinning energy. It is therefore the opinion of this author that the loss mechanisms as a function of heat cause only irreversible changes to the magnetization. While hysteresis loss was treated as a reversible effect during the original derivation of the model, the eddy-current loss and

anomalous loss were treated as having reversible components. At higher frequencies, the applied field created by these eddy-currents causes a change in the bowing of the domain walls, and the entire bowing process will be a strong function of frequency. This means that the parameter *c* governing the reversible magnetization process will be a function of frequency.

So that if we begin again with the energy supplied to the material and also add the additional losses due to eddy-currents with only the irreversible component of magnetization and the heat term we will have

$$\mu_o \int_0^{H_e} M_{irr} dH_e = \mu_o \int_0^{He} M_{an}(H_e) dH_e - \mu_o k\delta \int_0^{H_e} \frac{dM_{irr}}{dH_e} dH_e - \int \frac{\mu_0^2 d^2}{2\rho\beta} \left(\frac{dM_{irr}}{dt} \right)^2 dt - \int \left(\frac{GdwH_o}{\rho} \right)^{\frac{1}{2}} \left(\frac{\mu_o dM_{irr}}{dt} \right)^{\frac{3}{2}} dt \quad (2.54)$$

In following latter derivations of the model, it was found that the extraction of parameters was made easier by altering the work terms. Jiles noted that the mechanics of the model do not change. Similar to Jiles the substitution [38] of the fourth term on the right hand can be changed using the following substitution

$$\left(\frac{dM_{irr}}{dt} \right)^2 dt = \left(\frac{dM_{irr}}{dt} \right) \left(\frac{dM_{irr}}{H_e} \right) dH_e$$

Using this to replace the

$$\left(\frac{dM_{irr}}{dt} \right)^2 dt$$

term on the right hand side yields

$$\int \frac{\mu_0^2 d^2}{2\rho\beta}\left(\frac{dM_{irr}}{dt}\right)^2 dt = \frac{\mu_0^2 d^2}{2\rho\beta}\int\left(\frac{dM_{irr}}{dt}\right)\frac{dM_{irr}}{dH_e}dH_e \tag{2.55}$$

Likewise a substitution for the fifth term from (2.54) on the right hand side can be made by

$$\left(\frac{dM_{irr}}{dt}\right)^2 dt = \left(\frac{dM_{irr}}{dt}\right)\left(\frac{dM_{irr}}{dH_e}\right)dH_e \tag{2.56}$$

So that the fifth term from (2.54) becomes

$$\int\left(\frac{GdwH_o}{\rho}\right)^{\frac{1}{2}}\left(\frac{\mu_o dM_{irr}}{dt}\right)^{\frac{3}{2}} dt = \left(\frac{GdwH_o}{\rho}\right)^{\frac{1}{2}}\mu_o\int\left(\frac{dM_{irr}}{dt}\right)^{\frac{1}{2}}\frac{dM_{irr}}{dH_e}dH_e \tag{2.57}$$

Substituting back into (2.54) and dividing by μ_o yields

$$\begin{aligned}&\int_0^{H_{ee}} M_{irr}dH_e = \int_0^{H_{ee}} M_{an}(H_e)dB_e - k\delta\int_0^{H_{ee}}\frac{dM_{irr}}{dH_e}dH_e - \\ &\frac{\mu_0^2 d^2}{2\rho\beta}\int_0^{H_e}\left(\frac{dM_{irr}}{dt}\right)\frac{dM_{irr}}{dH_e}dH_e - \left(\frac{GdwH_o}{\rho}\right)^{\frac{1}{2}}\mu_o\int_0^{H_e}\left(\frac{dM_{irr}}{dt}\right)\frac{1}{2}\frac{dM_{irr}}{dH_e}dH_e\end{aligned} \tag{2.58}$$

Differentiating with respect to the applied field yields

$$\begin{aligned}&M_{irr}(H) = M_{an}(H) - k\delta\frac{dM_{irr}}{dH} - \\ &\frac{\mu_0^2 d^2}{2\rho\beta}\frac{dM_{irr}}{dt}\frac{dM_{irr}}{dH} - \left(\frac{GdwH_o}{\rho}\right)^{\frac{1}{2}}\left(\frac{dM_{irr}}{dt}\right)^{\frac{1}{2}}\frac{dM_{irr}}{dH_e}\end{aligned} \tag{2.59}$$

Substituting this into (2.58) yields the component of magnetization governing loss.

$$M_{irr}(H) = \frac{M_{an}(H) - M_{irr}(H)}{k\delta - \alpha[M_{an}(H) - M_{irr}(H)]} - \frac{\mu_0^2 d^2}{2\rho\beta}\frac{dM_{irr}(H)}{dt}\frac{dM_{irr}(H)}{dH} - \left(\frac{GdwH_o}{\rho}\right)^{\frac{1}{2}}\left(\frac{dM_{irr}(H)}{dt}\right)^{\frac{1}{2}}\frac{dM_{irr}(H)}{dH} \quad (2.60)$$

This is only the irreversible component, and the form of the reversible component remains unchanged. Once the irreversible component is solved, it can be added to the reversible component to find the total magnetization.

In dealing with the penetration depth of the field, it is recognized that the field will perform work only on a given volume of the core. The penetration of the field should be able to be treated in the same manner as minor loops in which a working volume of the core is approximated. In this way, the field performs work on a given volume of the core.

2.5. Chapter Summary

The basics of magnetic dipoles and magnetic domains have introduced for the purpose of describing the present theory of ferromagnetic hysteresis. A derivation of the model following the original work of Jiles and Atherton showed that no temperature dependence existed in the model despite the use of the mean field approach and the use of the Langevin function. In later work, Jiles acknowledged that no such temperature dependence can be given based upon the Boltzmann statistics in the modified Langevin equation, thus motivating a modification of the Jiles-Atherton model which is the core goal of this dissertation.

Multiple anhysteretic magnetization equations exist for a multitude of different material types and textures. The anhysteretic curve was identified as representing thermodynamic equilibrium as well as the ideal curve for magnetization with both interpretations being correct. A thermodynamic relationship was found for the low frequency case of the model which is required in the expanded high frequency case.

The present high frequency model is limited in several respects due to the lack of the inclusion of the field penetration into the core via the skin depth. It is believed that the high frequency loss terms should be included only in the irreversible component of the magnetization. The next two Chapters will offer the experimental validation of the ideas and theories presented for the purpose of formulating practical design models that can assist in the practical design of power electronics.

Chapter 3: Experimental Measurement System

3.1. Introduction to Measurement System

As shown in Chapter 2, $M_{an}(H)$ represents the defect free magnetization curve and contains no hysteresis. Using $M_{an}(H)$ with the Jiles-Atherton model, the $\boldsymbol{B}$-$\boldsymbol{H}$ relationship can be predicted. The measurement of $M_{an}(H)$ has been studied repeatedly [33], but no satisfactory method exist for measuring the curve without cutting the core to use a magnetic sensor. Pearson has studied the anhysteretic magnetization of magnetic cores, and his experimental approach [39] is closest to the one adopted here. The purpose of the measurement is to allow for the modeling the anhysteretic magnetization curve as a function of temperature, and its further study as a function of frequency.

A point on the curve is measured by demagnetizing the core with a static value of magnetic field [33]. This has been well established, but it is the practical reading of this point that is difficult. Each value of static H then yields a static B when the demagnetization process is complete, where B and H are not bolded to indicate the magnitude of the vector field. The material's magnetization is then found from Eq. (3.1)

$$\boldsymbol{M(H)} = \frac{\boldsymbol{B(H)}}{\mu_0} - \boldsymbol{H} \tag{3.1}$$

where, $M(H)$ is the magnetization, $B(H)$ is the flux density, H is the magnetic field, and μ_0 is the permeability of free space.

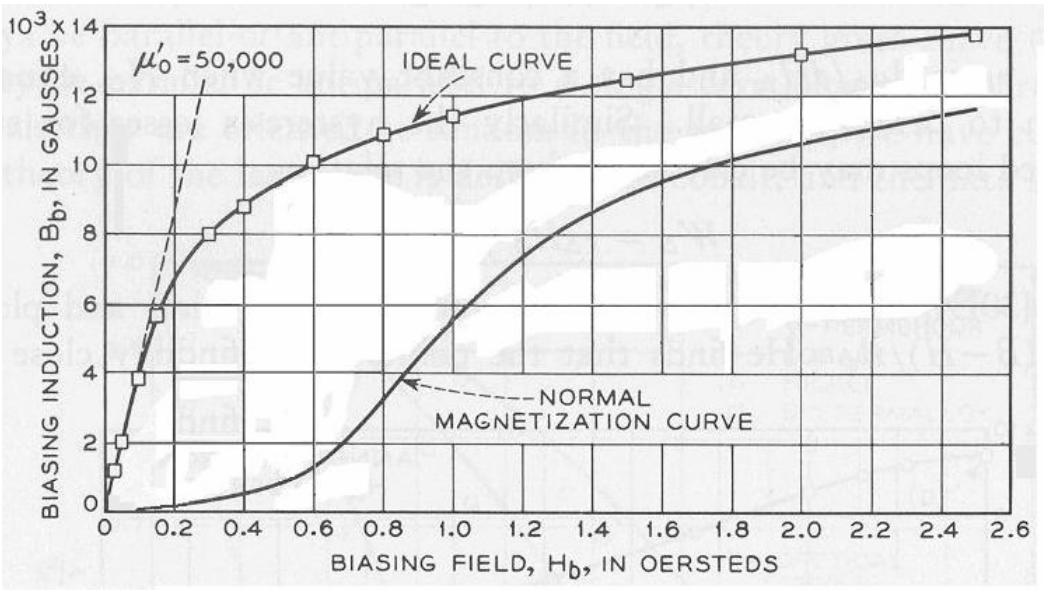

Figure 3.1 Original experimental measurement of $M_{an}(H)$ after Bozorth.

Figure copied from [33].

A major difficulty in the measurement of $M_{an}(H)$ arises from determining exactly where on the ***M-H*** plane a point forms. In measuring the magnitude of ***B***, the voltage induced slowly becomes zero because a static ***B*** cannot induce a voltage. Measurement of ***B*** should proceed after the demagnetization process is complete to ensure that ***B*** has come to its final value and to avoid reading of any induction caused by the demagnetizing waveform [40]. It is for this reason that magnetic sensors are employed to measure $M_{an}(H)$.

While it is possible to use a magnetic sensor to measure a residual ***B*** this requires the core to be cut and the sensor to be inserted. This alters the magnetostatic energy, the effective magnetic path length , the ***B*** field in the gap, and the overall ***M-H*** relationship [41]. Figure 3.2 shows the resulting change in the ***M-H*** relationship when a magnetic core is cut.

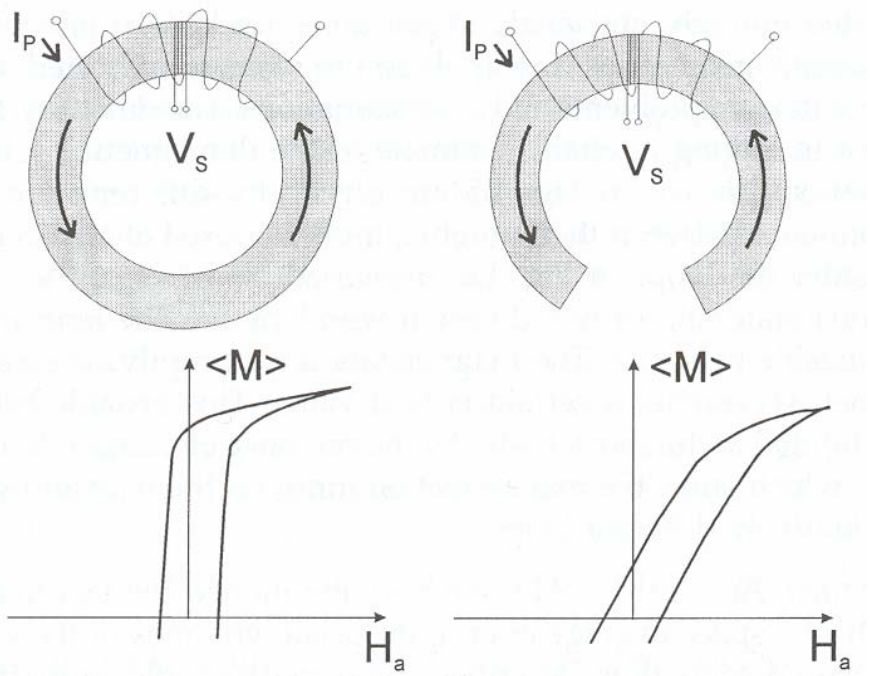

Figure 3.2 Alteration of the ***M-H*** characteristics due to a gap. This work avoids the use of magnetic sensors to avoid this alteration.

Figure copied from [29].

Commercial sensors can also have very limited temperature range, temperature dependent output, and require constant nulling of their offset [42]. It is for these reasons that a winding should be used to measure the actual ***B*** remaining in the material after demagnetization, yet it is not till this work that such a measurement has been successfully been reported.

H is directly proportional to the applied bias current and can be found using Ampere's Law as shown in Eq. (2)

$$H = \frac{Ni(t)}{l_e} \qquad 3.2$$

where, N is the number of turns on the winding, $i(t)$ is the current and l_e is the mean magnetic path length.

The determination of $\boldsymbol{B}$, however, is more difficult because the flux density is static after the demagnetization process is completed. We shall refer to the point that forms from both fields as (H_{DC}, B_{DC}) to emphasize the fact that the point on the $\boldsymbol{B}$-$\boldsymbol{H}$ plane corresponds to the magnitudes of the static H-field and the static $\boldsymbol{B}$-field present after the demagnetization process is completed. It should be noted that the $\boldsymbol{B}$-field will remain in its forced state if the applied $\boldsymbol{H}$-field and temperature remain constant.

The following magnetic characterization system is composed of seven major components, shown in Figure 3.3 in block diagram form and Figure 3.4 as a photograph. The system is integrated using National Instrument's LabVIEW™ programming language.

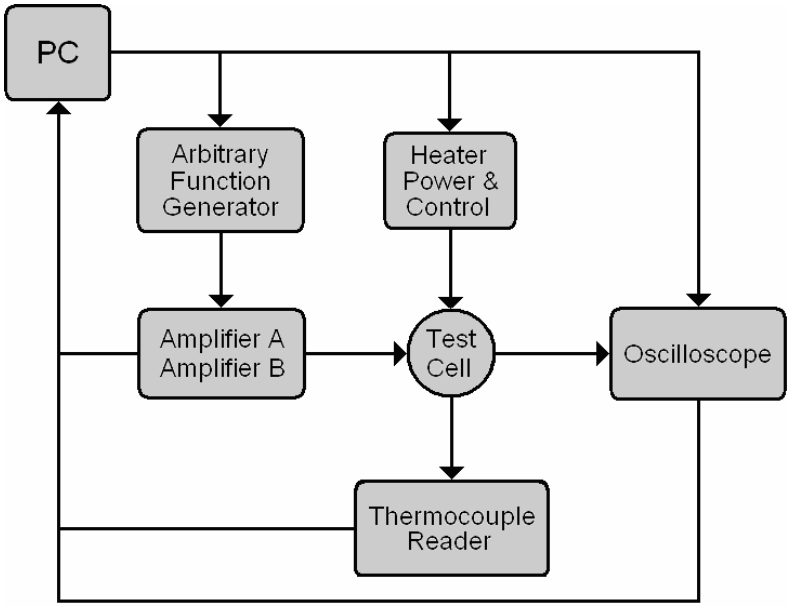

Figure 3.3 Block diagram of the characterization system showing the major components.

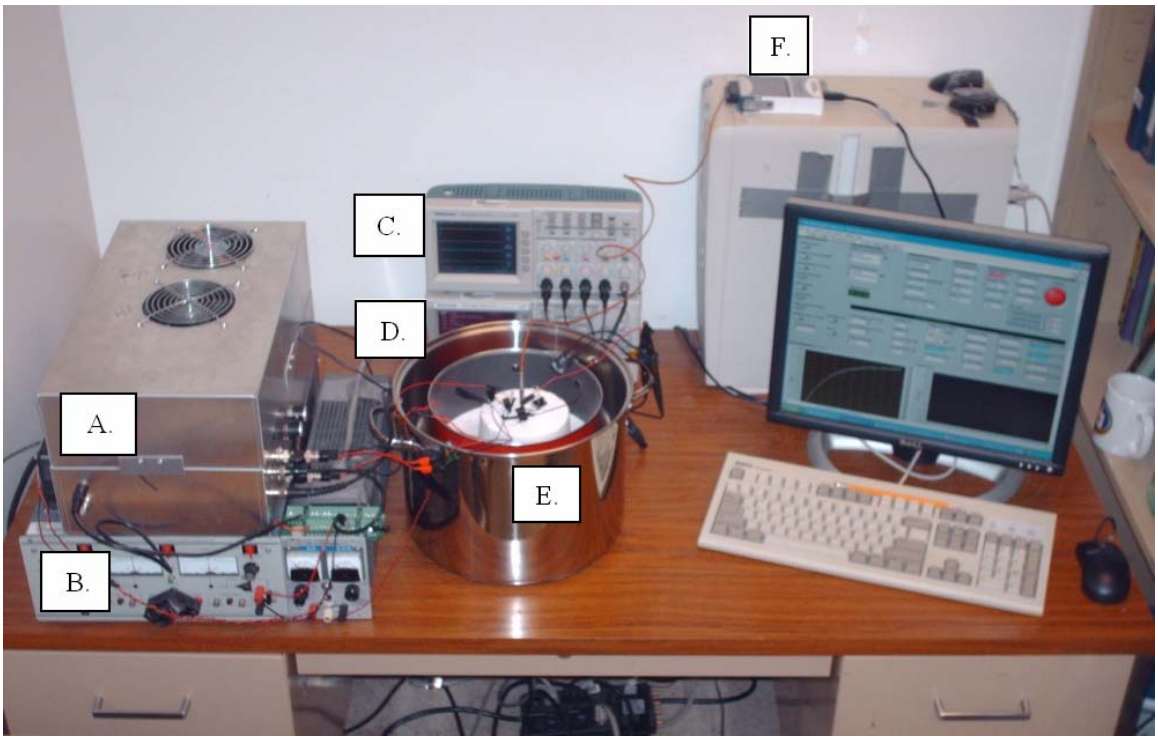

Figure 3.4 Photograph of the magnetization characterization system. The system is shown with its major components as follows A.) power amplifiers A and B, B.) heater power and control, C.) oscilloscope, D.) arbitrary function generator, E.) test cell, and F.) thermocouple reader.

All of the components, except the test cell and transconductance amplifiers, are commercially available products and may be easily substituted. The function generator and personal computer (PC) generate the AC and DC current waveform, respectively. Sample temperature is maintained by the heater and thermocouple reader through a PC-based control algorithm. Response and stimulus waveforms are capture by a digital oscilloscope and transferred to the PC for analysis.

The custom test cell, shown in Figure 3.5, is constructed of a closed copper cylinder that is uniformly heated along its perimeter and bottom by a pair of metal foil heaters. The

cylindrical heatsink enclosing the sample is surrounded by ceramic insulation to permit the system to achieve thermal equilibrium. The core-under-test is suspended inside the cell by its windings and a thermocouple is attached to monitor temperature. The temperature response had a measured deviation of +/– 0.3 °C.

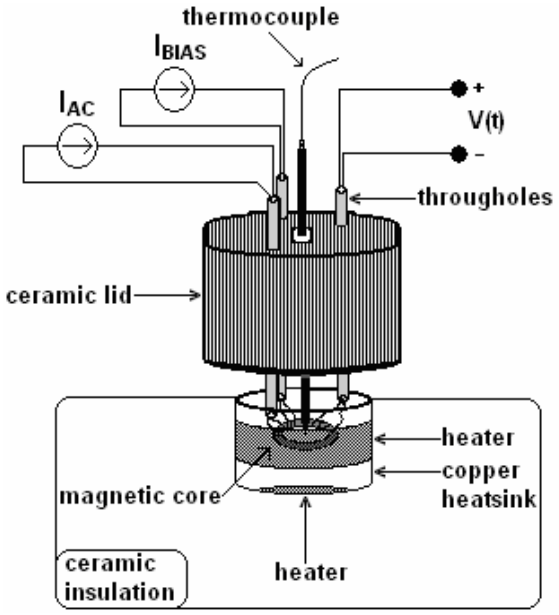

Figure 3.5 Test cell diagram showing the integrated heating elements and current sources connected to the toroidal core under test.

The current sources which produce the magnetic fields are implemented by a pair of high-speed, high-slew rate operational-amplifiers namely the PA09 manufactured by Apex Mircotechnology. These are labeled amplifiers A and B in Figure 3.3 and A.) in Figure 3.4. One current source, I_{BIAS}, maintains a DC current through one winding to establish the static *H*-field, while another current source, I_{AC}, provides the AC excitation on a separate winding. Previous work has relied upon voltage control to provide current excitation [43]. The total current will add together to produce the applied magnetic field to the core. I_{AC} will also be used to demagnetize the core and excite the core after the demagnetization process is

complete to obtain B_{DC}. The current sources were designed using the Apex Microtechnology PA09 Video Power Operational Amplifier to provide precision magnetic deflection [44]. Figure 3.6 shows the schematic of the current sources.

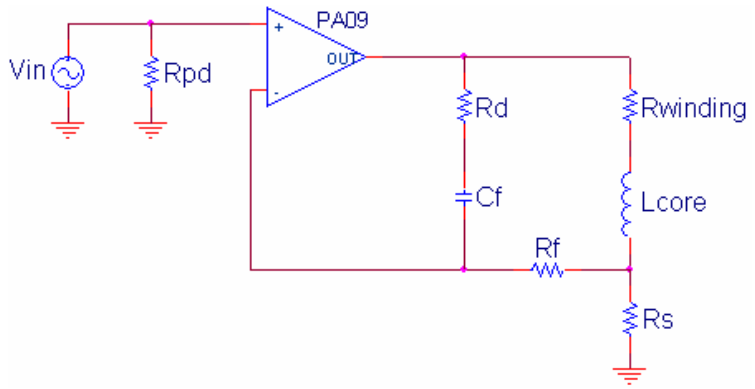

Figure 3.6 Schematic of the current sources used to generate I_{BIAS} and I_{AC}.

The operational-amplifier supplying I_{AC} is controlled by the arbitrary function generator. The inductance of the core creates a zero in the frequency response, which is cancelled by the pole created by *Rf*, *Rd*, and *Cf*. The number of turns on the I_{AC} winding must be balanced by the magnitude of the applied magnetic field needed to demagnetize the core [45]. For example, if 500 A/m is required to saturate the core during the demagnetization process, and the peak current from the amplifiers is 2.5A, then one can simply calculate the number of turns required using Ampere's Law, magnetic path length, and peak current. The number of turns will give a certain inductance value and therefore a known zero in the frequency response. The demagnetization process has to saturate the core. If the number of turns is too small, the core cannot be driven into saturation using the available peak current of the amplifier.

It should be noted that I_{AC} will induce a voltage on the bias winding where it is desired to only have a DC current flowing. In order for the operational amplifier producing I_{BIAS} to properly regulate the DC current through its winding, the induced voltage must be summed to zero. For example, when the DC input voltage is zero, the amplifier will produce at its output a voltage that has the same magnitude as the induced voltage yet opposite in polarity. This will cause zero current to flow through the bias winding. When the voltage on the positive input of the operational amplifier is incremented, the output will respond to force a DC current through its winding. In this way, the bias current can be regulated.

3.2. Measurement Procedure

In contrast to the method attributed to Bozorth[33], our method excites the core after the demagnetization process is complete to avoid cutting the core. The reading of the value of $M_{an}(H)$ is then decoupled from the excitation to place the core in a proper state.. The method does not cut the core to ensures that the magnetostatic, anisotropy, exchange energy and are not altered. By not cutting the sample, this energy balance is maintained and the actual $M_{an}(H)$ curve can be measured. Furthermore, it provides for the first time a methodology to measure the true $M_{an}(H,T)$ of a magnetic core.

The measurement process is summarized in Figure. 3.7. Once the sample's temperature is stabilized, H_{DC} is applied to the core in the form of a DC current via the I_{BIAS} winding. The demagnetization process is then initiated. The system generates a series of ten-cycle waveforms that will cause the current source I_{AC} to produce a decaying sinusoidal current in its winding. Each cycle has a magnitude that is approximately 1% less than the previous cycle in following the IEEE and ANSI standard for proper demagnetization.[45]

Lower decay rates of the demagnetization waveform have shown not to alter the final state of a core.[39] Once the initial ten cycles are complete, another ten cycles are initiated, and I_{AC} excites the core again with the demagnetizing current. This process is repeated. The final ten cycles of the demagnetization process utilize the lowest amplitude of the arbitrary function generator and the waveform generated decays to zero. This method of demagnetizing is performed for three reasons:

1. The amplitude of the demagnetizing waveform must decrease very slowly, so that the domain structure is allowed to reach thermodynamic equilibrium.

2. The arbitrary function generator has a limited sampling rate to recreate a single waveform with a very large number of cycles.

3. The system avoids excessive heating of the sample so that its temperature can be properly regulated.

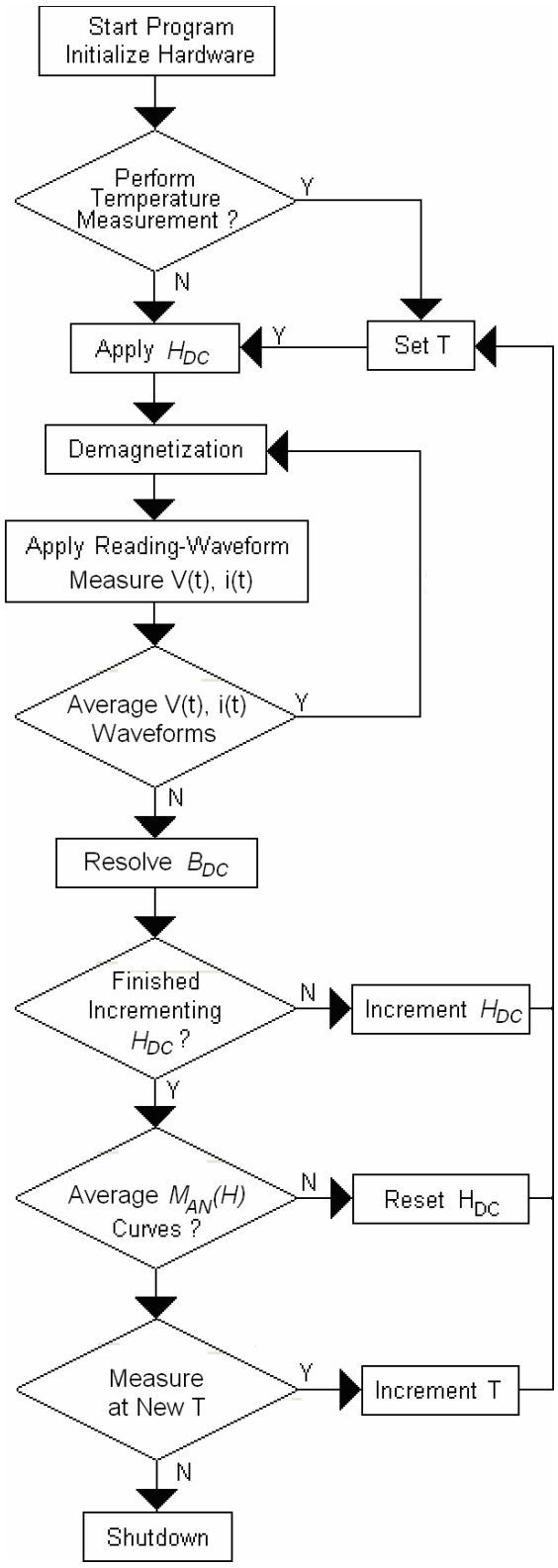

Figure 3.7 Flowchart showing the automated procedure to measure $M_{an}(H)$

Once the demagnetization process is complete the core is in a proper state to read the static B-field now held constant by I_{DC} and the present temperature**.** To accomplish this, the B-H loop is traversed while maintaining H_{DC}. Recall H_{DC} has already been set. Because a separate winding is used for the bias current, H_{DC} can be regulated throughout the measurement process.

To read B_{DC}, the present value of I_{BIAS} is passed to a subroutine that generates a nonsymmetrical sinusoid. This sinusoid is designed so that the total current, $I_{BIAS} + I_{AC}$, will cause the total applied H to have equal magnitudes in the positive and negative directions while still maintaining a constant median value, H_{DC}, as shown in Figure 3.8.

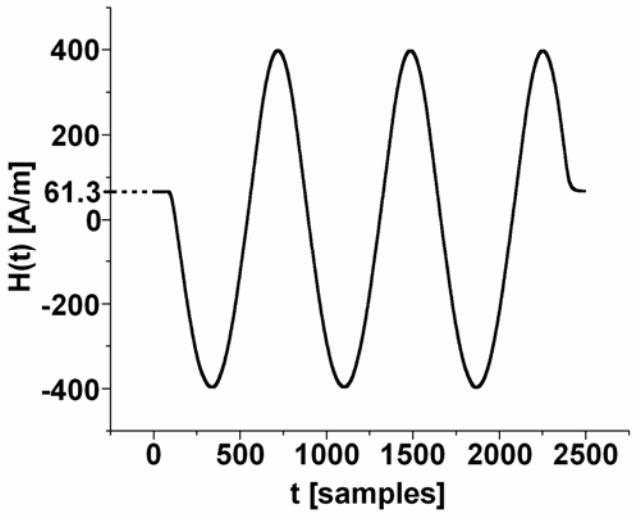

Figure 3.8 Total measured H created by $I_{AC} + I_{BIAS}$. By traversing H with equal magnitudes in the positive and negative direction, the magnitude of $\boldsymbol{B}$ in the positive and negative direction will also be the same. Here I_{BIAS} has produced an average $\boldsymbol{H}$-field of 61.3 A/m.

We will refer to this waveform as the *reading-waveform* as its purpose is to cause $\boldsymbol{B}$ to respond so that a point-of-reference can be established to correctly identify the magnitudes of B. This is necessary because only a change in flux induces a voltage as

shown in Figure 3.9. The induced, secondary voltage, $V(t)$, and the reading-waveform are captured by a Tektronix TDS 2014 Digital Storage Oscilloscope. Each channel on the oscilloscope is programmed to capture either a positive or negative portion of either the voltage or current waveform. The total waveform is then formed. Using (3.2) the flux is calculated from the measured $V(t)$.

$$\Phi = -\frac{1}{N}\int_{t_0}^{t_f} V(t)dt \tag{3.3}$$

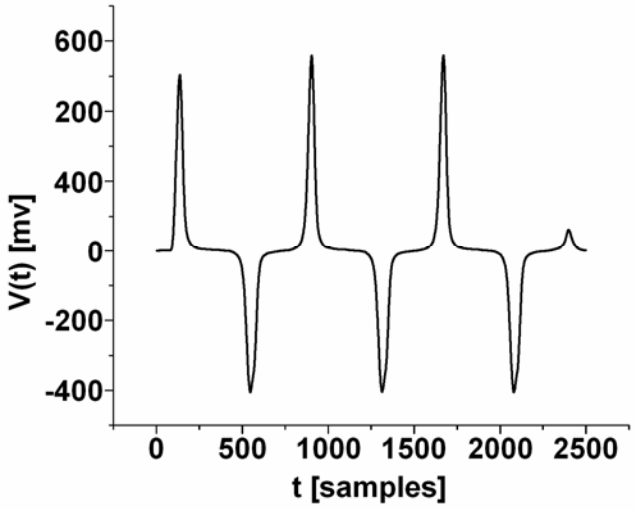

Figure 3.9 Measured secondary voltage generated by the reading-waveform.

Once $V(t)$ is measured, it is digitally re-sampled using an FIR filter with aliasing rejection of 120 dB. The mean value of the induced voltage is numerically calculated and subtracted from the entire voltage waveform. If this offset is not removed, the integration process will produce errors as the offset will be integrated with the induced voltage. The voltage offset present in the induced voltage waveform can result from the resistance in the windings and noise. From the consideration previously discussed in determining the number of windings, the offset due to the wire resistance can be minimized by using fewer turns.

The amplitude of the reading-waveform is then finely adjusted to null the offset after the first initial measurement. Once the flux is found by digital integration, the ***B*** field can be computed by dividing by the cross-sectional area, A, of the core. After the ***B***-field waveform is calculated, it will still have an apparent offset of the form

$$B = -\frac{1}{AN}\int_{t_0}^{t_f}[V(t) + V_{offset}]dt \tag{3.4}$$

remaining from the integrated voltage. This occurs as the final value of B linearly decays to zero as shown in Figure. 3.10. The cause of this is that a static B-field cannot induce a voltage. As a result, the final value of the ***B*** field appears to be zero according to the integration of the induced voltage. Physically, the initial and final values of B should be different. It can be observed from Figure 3.11 that the waveform decreases by a linear amount as the integrated waveform attempts to come to rest at zero instead of a final static value of ***B***.

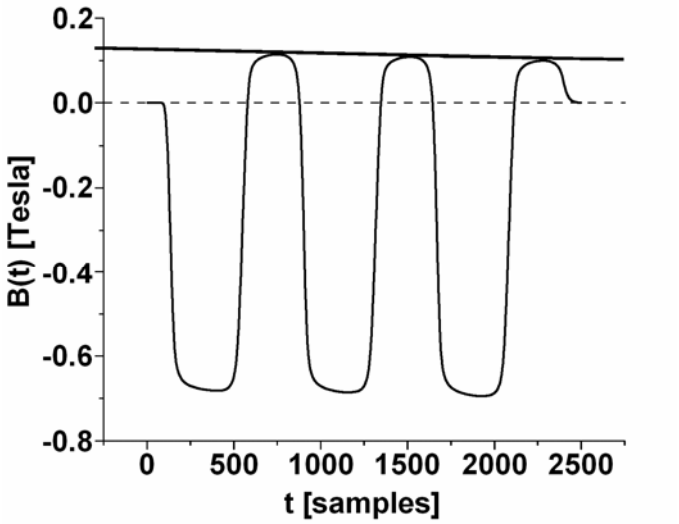

Figure 3.10 Measured *B* field response – not aligned. This is the unprocessed measured *B*-field waveform resulting from application of the reading-waveform. The *B*-field linearly decays to zero because the flux is not directly measuring the final static field.

The final value of ***B***-field waveform appears to be zero, but in reality an offset from the initial value should be present. The peaks and valleys should also have the same magnitude. To correct for this linear decay, an offset voltage is added to the induced voltage and it is reintegrated to causes a linear rise in the ***B***-field waveform. This is done iteratively until the midpoints between the peaks and valleys of the ***B***-field waveform align as they should with excitation of equal magnitude as shown in Figure 3.11.

The ***B***-field plotted over time will then cycle about zero. However, because the change in ***B*** is equal in both the positive and negative directions, it can be said with certainty that the value of zero ***B*** is at the midpoint of the peaks and valleys. This is the reference point that has been established by the reading-waveform. If the reading waveform had not traversed ***H*** with equal magnitude, the value of zero ***B*** could not be identified with certainty.

This would be the same value of zero ***B*** that would be identified on a ***B*-*H*** plot under cyclic excitation.

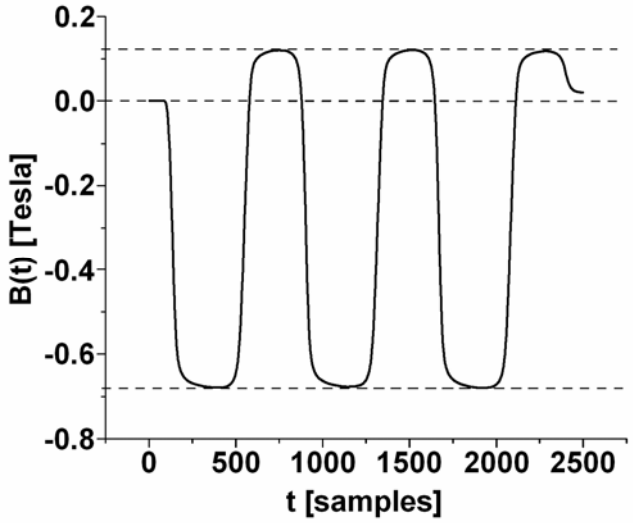

Figure 3.11 Measured *B* field response – aligned. This is the *B*-field waveform resulting from application of the reading-waveform. The corrected *B*-field now cycles about zero. The peaks and valleys now have equal magnitude for equal excitation.

To properly identify B_{DC}, which is the static field left after the demagnetization, the magnitudes of the peaks are averaged and the mid-point between them is identified so that B_{DC} is given by

$$B_{DC} = \frac{\left| \frac{\sum_{i=n} V_{peaks}}{n} - \left| \frac{\sum_{i=n} V_{valley}}{n} \right| \right|}{2} \tag{3.5}$$

where n is equal to the number of cycles used in the reading waveform. This midpoint will be negative and its absolute value will be added to the total ***B***-field waveform.

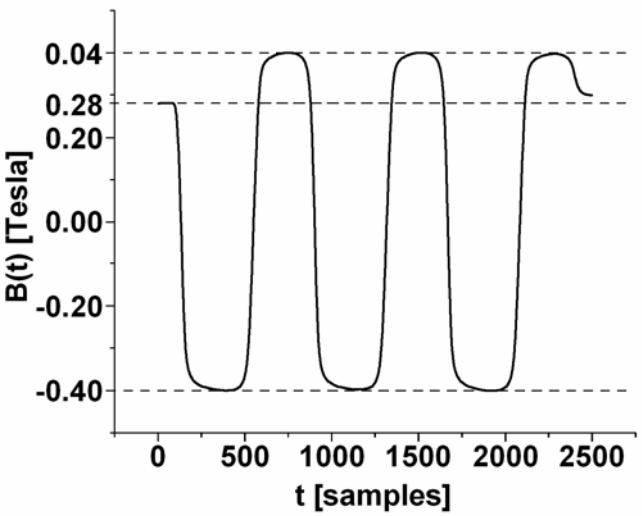

Figure 3.12 *B*-field resulting from B_{DC} being properly identified. The value is read after the demagnetization process. Here the value of B_{DC} is equal to 0.28T.

It can be observed from Figure 3.12 that saturation of the ***B***-field now occurs at the same magnitude of ***B*** in both the positive and negative directions, which is expected when applying ***H*** with equal magnitudes in the positive and negative direction. Clearly, if the reading-waveform does not have equal magnitudes in the positive and negative direction, then identification of the midpoint will introduce an error. Measurement and nulling of the offset in the reading-waveform after an initial measurement greatly minimized this error.

Once H_{DC} and B_{DC} are found, the value of M_{DC} can be determined using

$$M(H) = \frac{B(H)}{\mu_0} - H \tag{3.6}$$

Thus, a single point on the anhysteretic magnetization curve is known. Once a single point is measured, the measurement may be repeated and averaged to increase accuracy. Before each point is measured, the core undergoes the same demagnetization process

with the same value of H_{DC}. In this way, the core is placed in the same state and signal averaging can be performed.

3.3. Chapter Summary

The experimental setup involving the measurement of anhysteretic magnetization curve has been demonstrated. The setup is capable of performing non-destructive testing on magnetic cores by applying a wave-form to read the resulting ***B*** field of a core. This resulting ***B*** field can be placed in terms of ***M*** and the resulting magnetization can be measured.

The applied reading-waveform takes the form of a sinusoid with a median value, and traces through the complete ***B***-***H*** loop. If the static H applied in the bias winding is set to zero, then the initial magnetization curve is traced from the origin of the ***B***-***H*** plot, and the normal ***B***-***H*** loop is formed. This allows the normal extraction of model parameters directly from a normal ***B***-***H*** loop.

Chapter 4: Temperature Dependent Data

4.1. Measured Anhysteretic Magnetization Curves

The measurement of the anhysteretic magnetization was performed using the experimental setup described in Chapter 3 of this dissertation on a MnZn ferrite core manufactured by Magnetics Inc. (part# 0P40401TC). The core was suspended in the test cell using MWS 31AWG NEMA MW16-C high-temperature copper wire. The temperature was incremented at 17°C increments, and the family of curves for the anhysteretic magnetization was measured as shown in Figure 4.1.

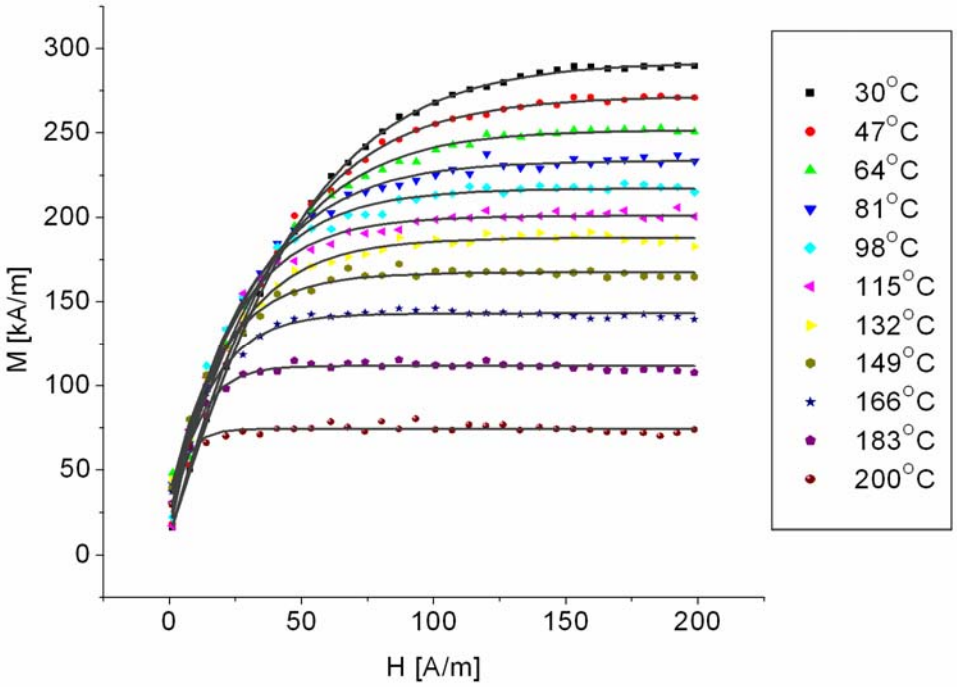

Figure 4.1 A family of anhysteretic magnetization curves measured for a MnZn ferrite manufactured by Magnetics Inc. (part # 0P40401TC) as a function of core temperature. Two waveforms were averaged for each point.

As a point of reference to the above given data, data is shown below from a different author attempting to measure the same curve experimental curve being demonstrated here. Figure 3.14 shows the measurement of the anhysteretic magnetization curve for a sample of pure, polycrystalline nickel (99.98%) wire 150mm long and 1mm in diameter performed by Pearson.

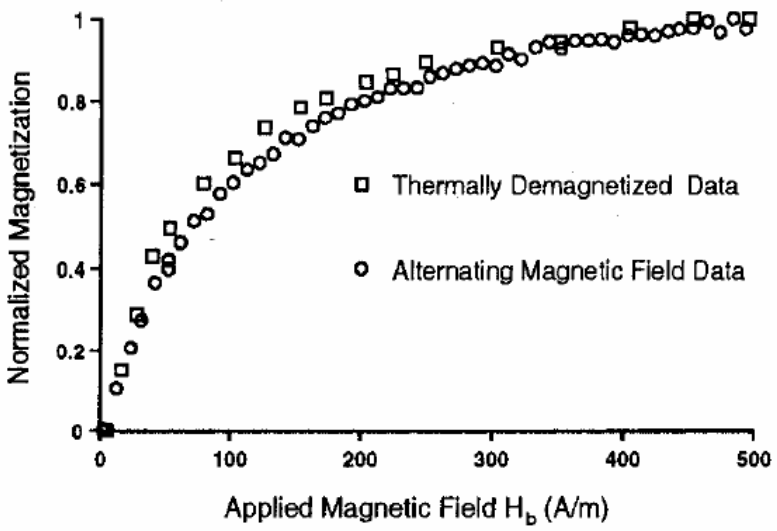

Figure 4.2 Measurement of the $M_{an}(H)$ curve of nickel performed by J. Pearson.

Figure copied from [39].

Pearson summarizes how he resolved the point on the curve by stating, "…anhysteretic magnetization could be deduced by measuring the flux change to saturation."[39] This is the only information provided as to how he resolved the static $\boldsymbol{B}$ field on the curve for a given bias current. Details on how the waveforms were measured or excited were not provided.

This author would like to note that he too attempted to resolve the anhysteretic magnetization curve using the saturation magnetization as a point of reference, and found using only the distance to saturation unsatisfactory. This was due to the fact that magnetization saturation is not a fixed point of reference because the saturation magnetization increases for a larger magnitude of applied field. There is therefore a distinction made between technical saturation and complete saturation [19]. This is one of the reasons why the methodology of the previous section was adopted.

Pearson must also assume that the core is in the zero state after demagnetization. In doing so, the anhysteretic remanence magnetization must be assumed to be zero. Even in the symmetrical torrid used for these experiments, this is not true. In simpler terms, the experimental anhysteretic curve will possess a remnant value of magnetization which will change the value of the resulting anhysteretic magnetization curve.

4.2. Data Analysis and Model at Static Temperature

Now that $M_{an}(H,T)$ has been properly measured the data analysis portion of the work can begin. The static temperature model requires an equation to represent $M_{an}(H,T)$ along with the other model parameters

4.2.1. Curve Fitting for $M_{an}(H,T)$

The data presented in this section is that of a commercially available MnZn, power ferrite (Part# 0F-40401-TC) manufactured by Magnetics Inc [8]. Microcal Origin was used to perform a nonlinear least squares fit for the collected data for the data shown in Figure 3.13. It was found that the Boltzmann Function given as

$$M_{an}(H,T) = \frac{M_1(T) - M_2(T)}{1 + e^{\left(\frac{H - H_o}{H_f(T)}\right)}} + M_2(T) \tag{3.1}$$

represents $M_{an}(H,T)$ for the MnZn ferrite sample, where M_2, and dH are linearly dependent upon temperature. A_1 and H_o are temperature independent constants and provide the form factor for the curve. Figure 3.15 shows the curve fit of $M_{an}(H,T)$ with the collected data.

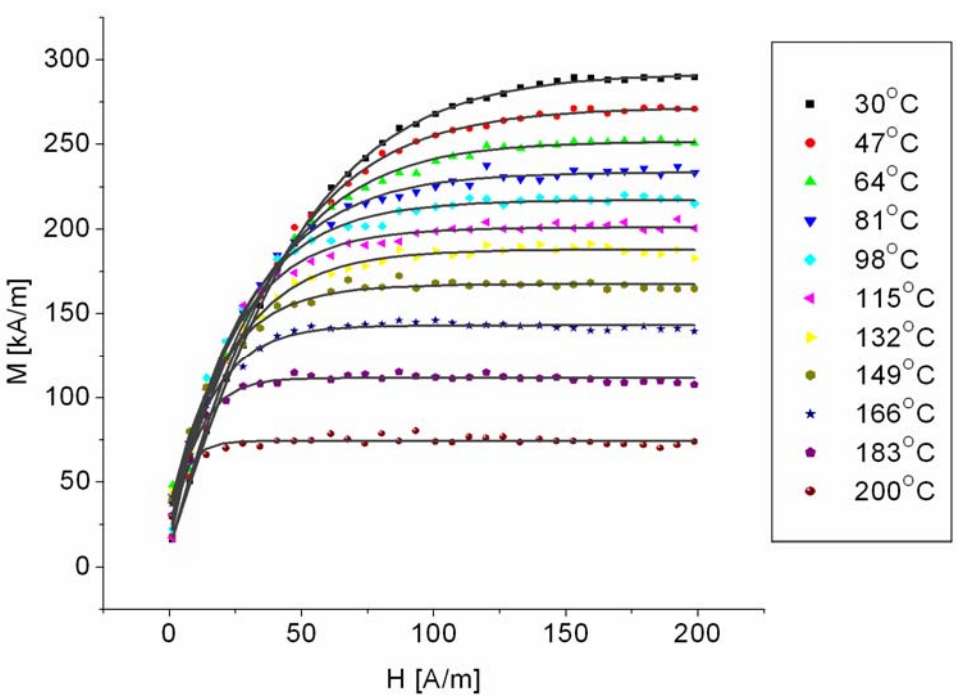

Figure 4.3 Curve fit of $M_{an}(H,T)$ for the data of a MnZn ferrite sample. The Boltzmann Function ideally models the temperature and field characteristics of $M_{an}(H,T)$.

It is pointed out that the magnitude of $\boldsymbol{M}$ in Figure 4.3 does not become zero for a zero value of applied $\boldsymbol{H}$. This is expected. If the curve is examined closer to the origin in Figure 4.4, this is more easily observed.

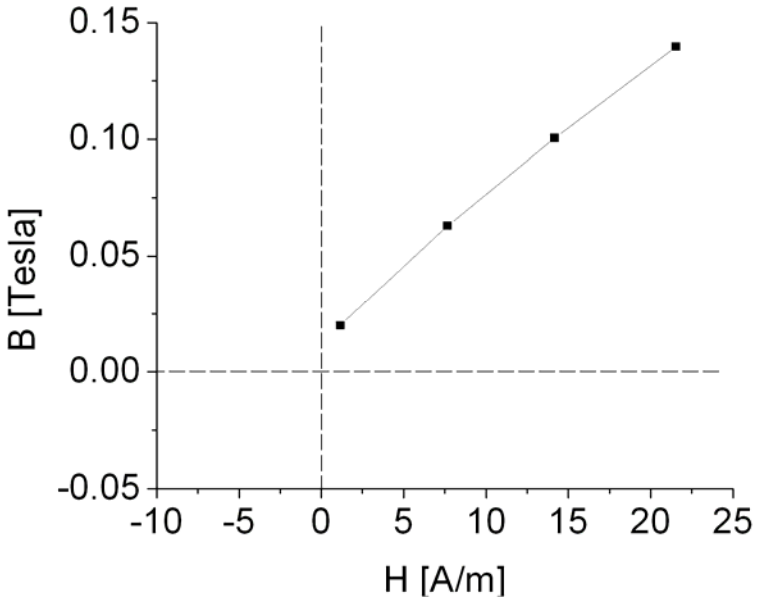

Figure 4.4 Zoomed in view of $M_{an}(H)$ measured at 30°C. Note the crossing the y-axis and the nonzero B field value. Measurement performed for the MnZn ferrite sample.

This phenomena is called anhysteretic remanence or ARM (i.e., anhysteretic remanence magnetization), and is a result of the applied $\boldsymbol{H}$ being different than the internal $\boldsymbol{H}$ experienced in the bulk material. This is well known in the area of magnetic media recording where the anhysteretic magnetization is measured for the purposes of linearizing the media [46]. To compensate for the internal $\boldsymbol{H_{IN}}$ of the bulk having a different magnitude of magnetic field than that which is applied, demagnetization factors are often calculated of the form

$$\boldsymbol{H_{IN}} = \boldsymbol{H_A} - k_{df}\boldsymbol{M} \tag{3.2}$$

where H_{IN} is the internal magnetic field, H_A is the applied magnetic field and k_{df} is the demagnetization factor.

To minimize this effect in the measurements performed, a small toroidal sample was used with equal height and width. However, it was found that the demagnetizing field that

truly results from the divergence of the magnetization is still present. Toroidal magnetic cores produced by modern manufacturers are actually cylindrically-shaped, and the demagnetizing field of such ring cores has been studied by D.B. Clarke who sought to model the effect [47].

In modeling the anhysteretic magnetization as a function of temperature, the H intercept was calculated using the linear portion of the anhysteretic magnetization curve near the origin. This was then added to the total applied H to represent the internal value. For all temperatures curves, the internal and external H varied by 2A/m irrespective of temperature. This allowed $M_{an}(H,T)$ to be modeled as

$$M_{an}(H,T) = \frac{M_1(T) - M_2(T)}{1 + e^{\left(\frac{H}{H_f(T)}\right)}} + M_2(T) \tag{3.3}$$

Equation (4.3) is modified slightly from (4.1) in that H_o has been removed as the curve now intersects the origin. The following curves are shown shifted to zero and modeled with (3.3).

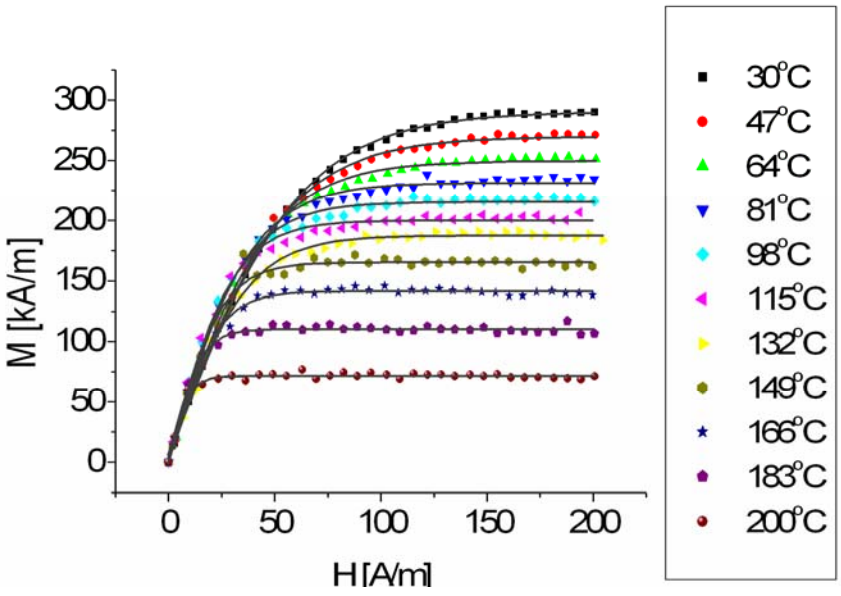

Figure 4.5 Curve fit of $M_{an}(H)$ intersecting at the origin.

It follows then that $M_2(T)$ displays the trend shown in Figure 3.19, and is easily represented by a linear fit.

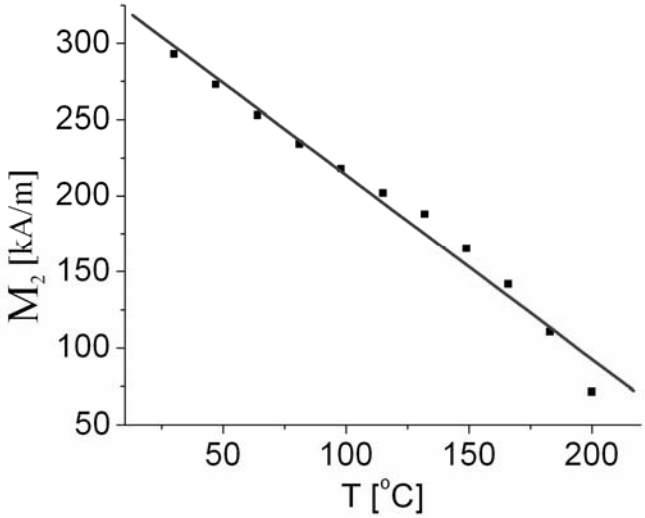

Figure 4.6 Linear curve-fit for M_2 as a function of temperature.

Where M_2 is now given by

$$M_2 = M_{sp}T + M_{INT} \tag{3.4}$$

From Figure 3.19 M_{SP} = -1118.98 and M_{INT} = 325496.80.

M_1 is plotted as a function of temperature in Figure 4.7 and can also be shown to be a linear function of temperature.

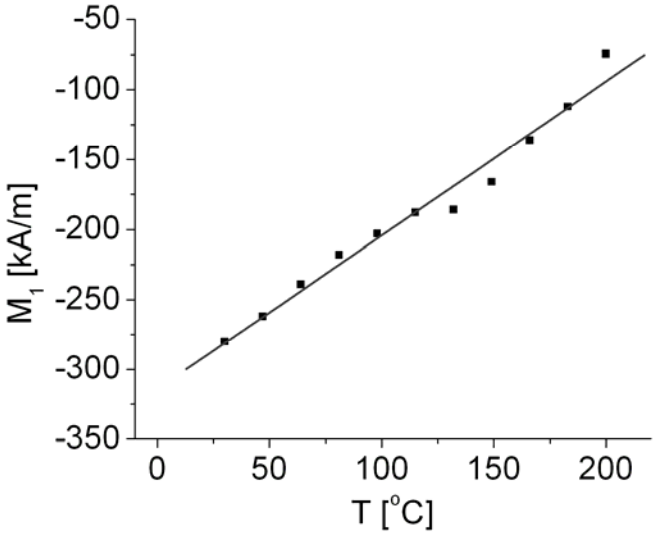

Figure 4.7 Linear curve-fit for M_1 as a function of temperature.

Having seen that M_1 and M_2 are both linear functions of temperature; a boundary condition on each will now be implemented. If $M_{an}(0,T) = 0$, then it follows from equation (4.3) that

$$M_{an}(H,T) = 0 = \frac{M_1(T) - M_2(T)}{1 + e^{\left(\frac{0}{H_f(T)}\right)}} + M_2(T)$$

Therefore,

$$0 = \frac{M_1(T) - M_2(T)}{1+1} + M_2(T)$$

And it is easy to see that

$$M_1(T) = -M_2(T)$$

M_1 can be eliminated from the equation of $M_{an}(H,T)$.

Substituting $M_1(T) = -M_2(T) = M_f(T)$ into the equation of $M_{an}(H,T)$ yields

$$M_{an}(H,T) = \frac{-2M_f(T)}{1+e^{\left(\frac{H}{H_f(T)}\right)}} + M_f(T) \tag{3.5}$$

In dealing with the remain term in the equation for $M_{an}(H)$, we also discover a linear dependence on the term H_f.

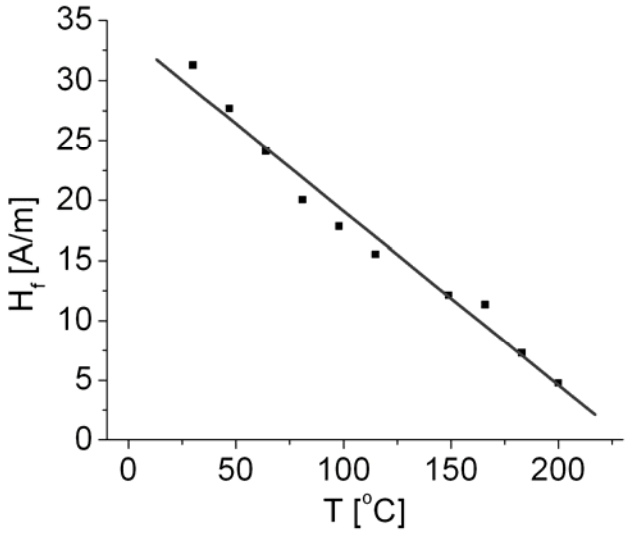

Figure 4.8 Linear dependence of the curve-fit parameter H_f as a function of temperature.

So that

$$H_f = H_{SP}T + H_{INT} \tag{3.6}$$

where H_{SP} = -0.1454 and H_{INT} = 33.672 for the data shown in Figure 4.5. $M_{an}(H,T)$ is know only a function of two parameters H_f and M_f.

4.2.2. Static Temperature Model

Continuing with the building of the static model for the MnZn core, the static temperature model, the parameter extraction from the *B-H* loop must be performed as a function of temperature. Following this $M_{an}(H,T)$ is used to predict the temperature

dependence of the core. In doing so, we will modify the extraction procedure for the model parameters. It should be noted that a very important point in the new dynamic equations introduced that both the temperature and frequency equation revert back to their original forms for the static, low frequency case. Therefore, model parameter extraction is performed on the static model.

4.2.2.1. Customized Extraction Procedure using $M_{an}(H,T)$

One of the biggest disadvantages of the Jiles-Atherton model is known to be the difficulty involved with parameter extraction. Since its introduction the extraction process of the model parameters has seen major refinement, but it still involves solving several sets of transcendental equations [35]. Part of the difficulty also involves what is considered a lack of "fixed points" reference points on the ***B-H*** loop. A modification of the standard extraction procedure will follow. The use of the new equation describing $M_{an}(H,T)$ will be used. In doing so the extraction procedure is greatly eased and the model parameters can be solved explicitly. Beginning with the irreversible component of magnetization,

$$\frac{dM_{irr}(H)}{dH} = \frac{M_{an}(H) - M_{irr}(H)}{k\delta - \alpha(M_{an}(H) - M_{irr}(H))}$$

The value of k is set to that of the coercive field [48] as found from the M-H loops shown Figure 3.9.

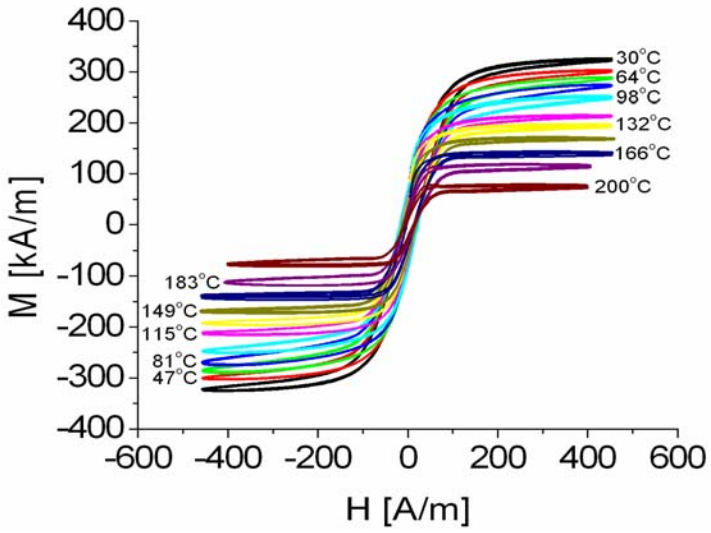

Figure 4.9 Measured family of *M-H* loops. The measurement performed on MnZn ferrite was used to extract the parameters of the Jiles-Atherton model as a function of temperature. The temperature is incremented by 17°C for each loop.

The coercivity was measured to be approximately 17A/m. For the MnZn ferrite sample modeled here k will be treated as a constant. In finding the other parameters, we will we will look at the irreversible component of magnetization.

$$\frac{dM_{irr}(H)}{dH} = \frac{M_{an}(H) - M_{irr}(H)}{k\delta - \alpha(M_{an}(H) - M_{irr}(H))}$$

Here k = 17A/m. $M_{an}(H,T)$ was measured. Jiles noted that when $H = H_c$, that the magnetization processes involved were only irreversible, and used this in the extraction procedure [35]. This author will also make use of this knowledge. So that

$$\frac{dM_{irr}(H_c)}{dH} = \frac{M_{an}(H_c) - M_{irr}(H_c)}{k\delta - \alpha(M_{an}(H) - M_{irr}(H))}$$

and

$$M_{irr}(H_c) = 0$$

and $\frac{dM_{irr}(H_c)}{dH}$ is given the slope of M at H_c.

The irreversible component then becomes at H_c is given by

$$\frac{dM_{irr}(H_c)}{dH} = \frac{M_{an}(H_c)}{k\delta - \alpha M_{an}(H_c)}$$

The author would like to point out that according to the model being used when M is measured it is measured with the inter-domain coupling coefficient α so that

$$\boldsymbol{B} = \mu_o(\boldsymbol{H} + \alpha \boldsymbol{M})$$

according to the model. So that the measured anhysteretic magnetization curve does not represent $M_{an}(H)$ alone, but rather $\alpha M_{an}(H)$. At this point, $\alpha M_{an}(H)$ is treated as the known term and is used to find $M_{an}(H_c)$. Once this is done, then $M_{an}(H_c)$ can be used to calculate the model parameter α. Figure 3.23 shows alpha plotted as a function of temperature. The parabolic fit shows good agreement with Figure 3.23.

$$\alpha = (2.85\text{E} - 4) - (1.17\text{E} - 6)\text{T} + (8.74\text{E} - 9)\text{T}^2 \tag{3.7}$$

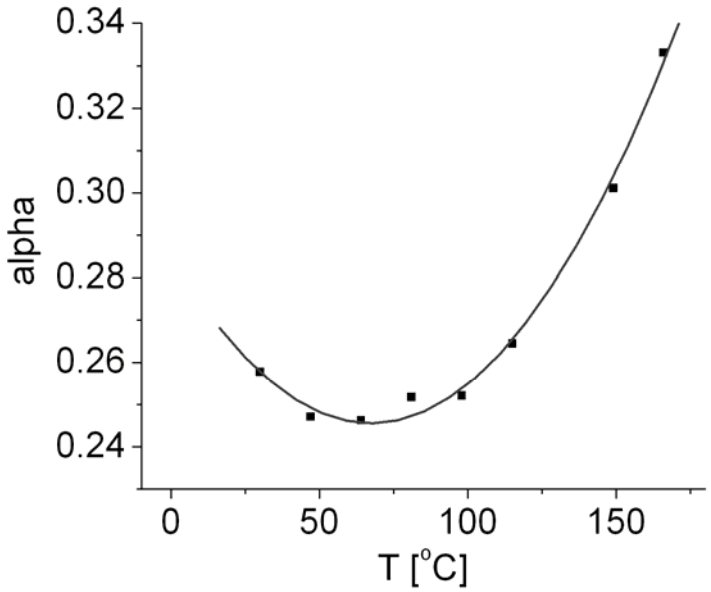

Figure 4.10 The model parameter α modeled as a function of temperature using a simple parabolic fit.

Now that the parameters for the irreversible components have been found the parameter governing the reversible component can be found. For the reversible component of magnetization,

$$M_{rev}(H) = c(M_{an}(H) - M_{irr}(H))$$

it is known [35] that the irreversible component of magnetization is essentially zero near the origin for small deviations. In setting $M_{irr}(H) = 0$ near the origin, $M_{an}(H)$ will be related to $M(H)$ by the parameter c. Because both $M_{an}(H)$ and M(H) will be zero near the origin, we will use the relationship between their slopes to find c. So that

$$c = \frac{\frac{dM_{rev}(H,T)}{dH}}{\frac{dM_{an}(H,T)}{dH}} \tag{3.8}$$

These expressions can be evaluated numerically. The slope of the initial magnetization curve can then be taken as the reversible component. However, it is helpful to simply take the derivative of $M_{an}(H,T)$ and evaluate it at the origin.

$$\frac{dM_{an}(H,T)}{dH} = \frac{2M_f(T)e^{\frac{H}{H_f(T)}}}{H_f(T)\left(1+e^{\frac{H}{H_f(T)}}\right)} \tag{3.9}$$

Here a similar result as before is presented. Contrary to the results of Wilson [36], Figure 3.24 shows that the parameter *c* did not vary with temperature. The average value measured at each temperature will then be used for the value of c. Therefore c = .242 for the data presented here and the last parameter for the static temperature model is known.

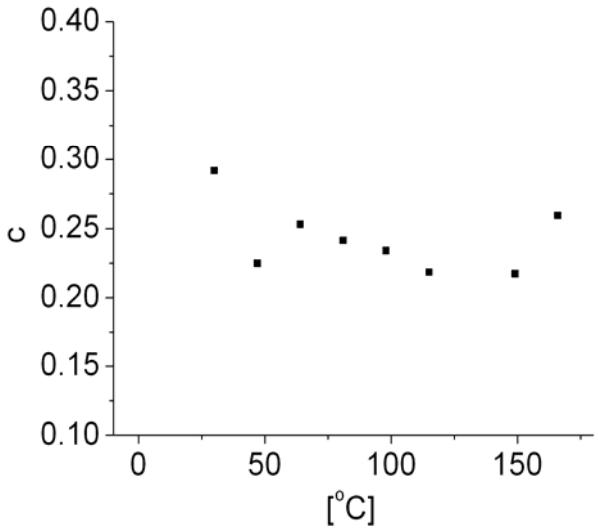

Figure 4.11 The model parameter *c* governing the reversible component of magnetization was found not to vary with temperature.

4.2.2.2. Predicted and Compared Results at Static Temperature

The model was implemented in Maple 11 from Maplesoft [49] using the data collected in the previous section. The following is a comparison of predicted and simulated results.

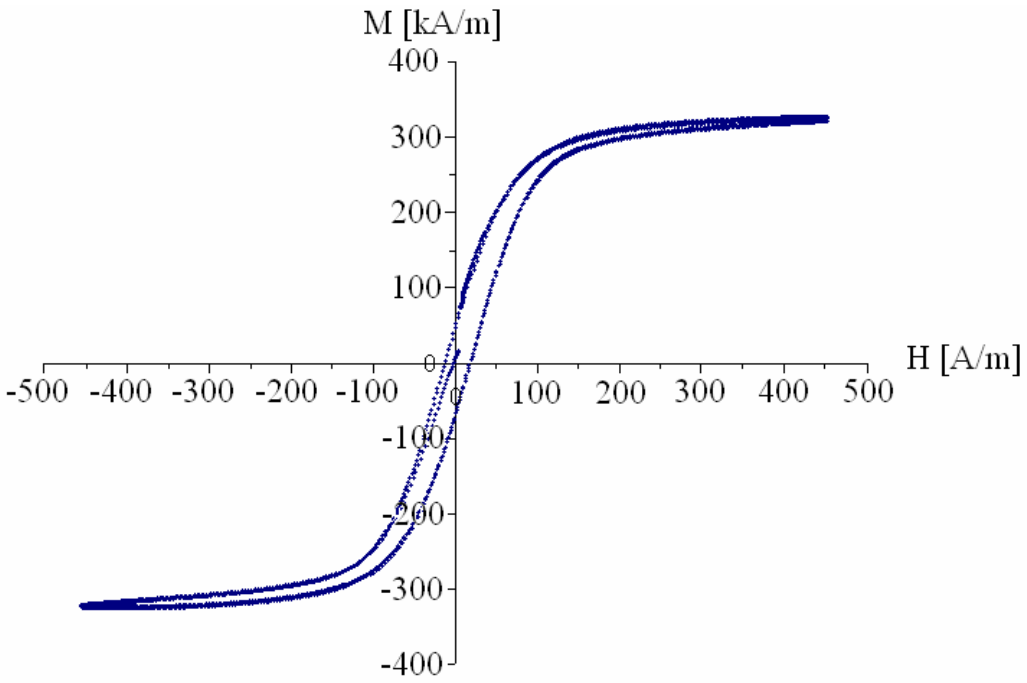

Figure 4.12 Measured ***B*-*H*** curve at 30°C of the MnZn ferrite sample.

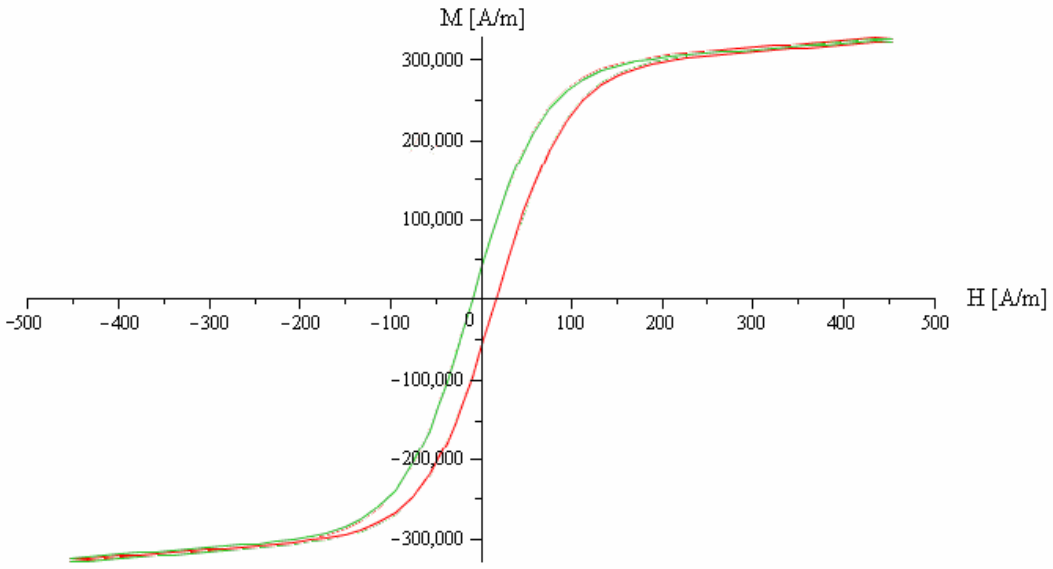

Figure 4.13 Predicted ***M-H*** curve at 30°C of the MnZn ferrite sample. The red curve is formed by the setting of the initial condition in the differential equation to begin at negative saturation. Likewise the green curve is formed by the setting of the initial condition to begin at positive saturation.

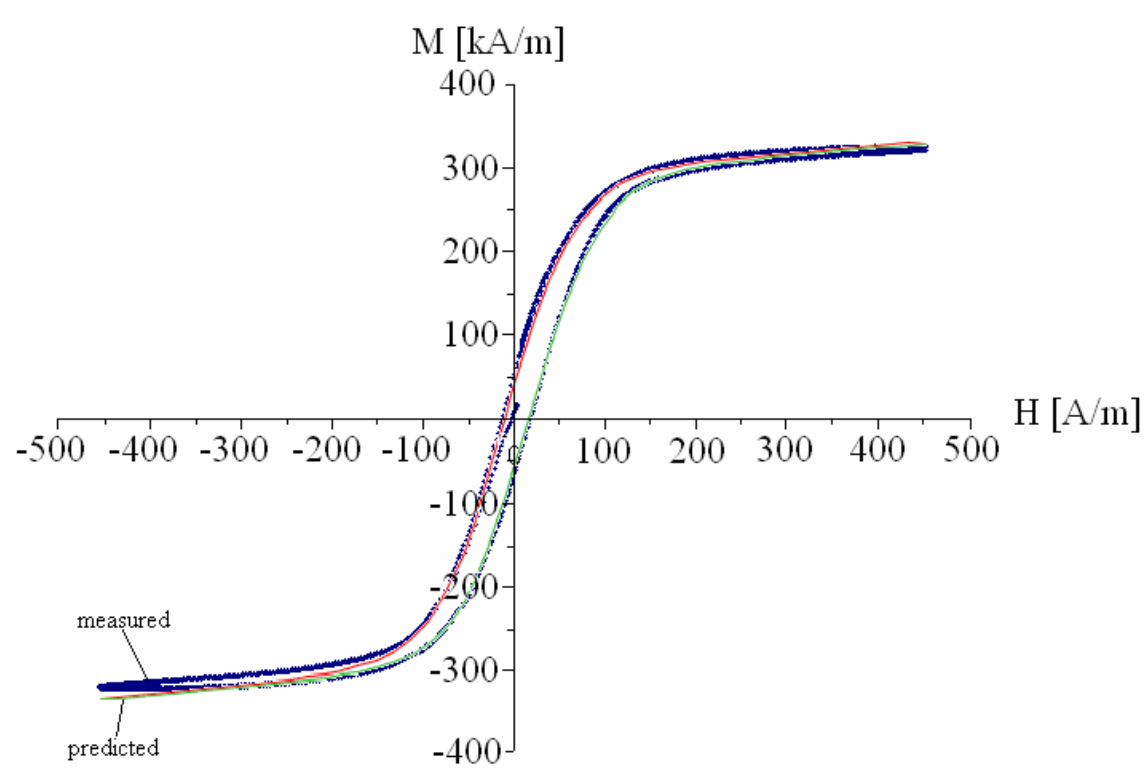

Figure 4.14 Direct comparison of measured and predicted ***B*-*H*** curves. The curve from Figure 4.12 is overlaid on top of the curve from Figure 4.13. The predicted and measured ***B*-*H*** curves match very well. Measurement and prediction are made at 30°C.

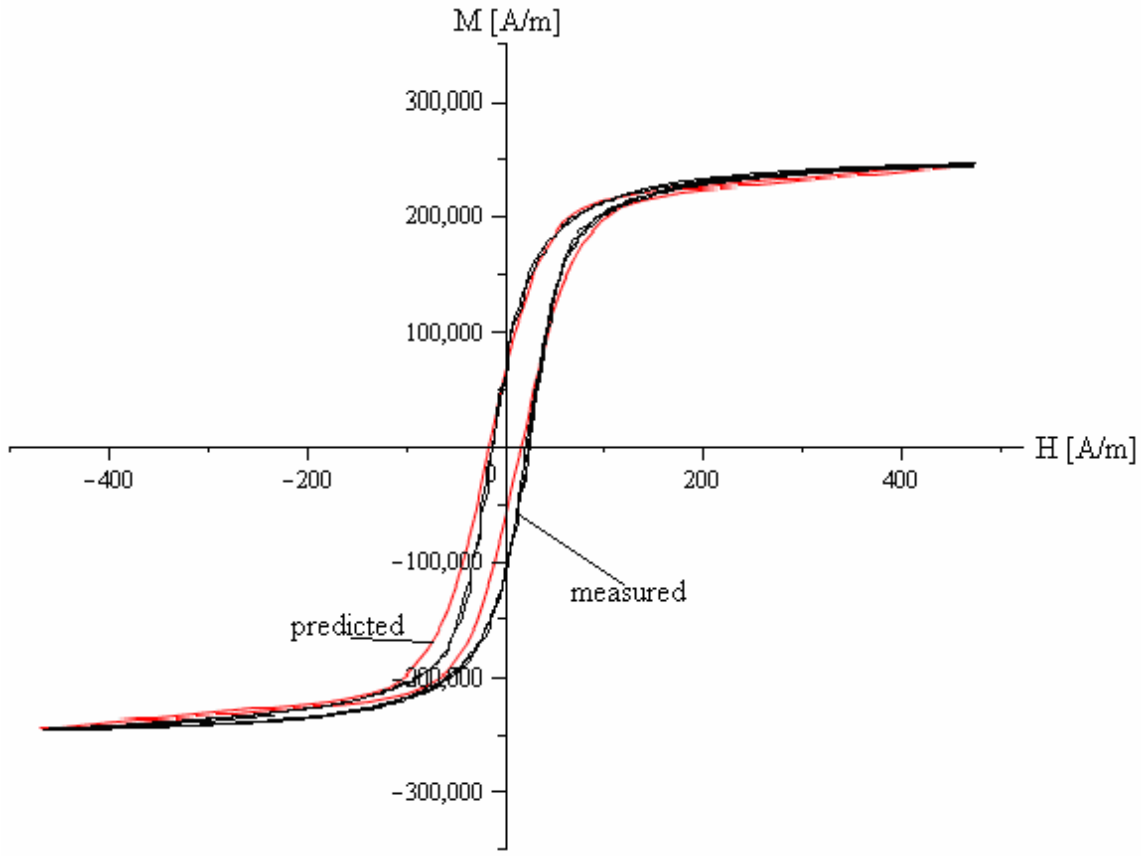

Figure 4.15 Direct comparison of predicted ***M-H*** loop at 98°C.

4.3. Dynamic Heating Experiments

In Chapter 2, the idea of a heat flux changing the work done on the sample was presented to show that if the work done on the sample cannot be accounted for by the hysteresis loss, then the heat flux will cause an offset from the anhysteretic magnetization curve. To prove that this does not occur, the following experiment was performed. The magnetization characterization system was adapted to allow instantaneous triggering of the function generator by the thermocouple. The lid of the test cell was removed, and a Thermolyne type 1900 hotplate was used to heat one cup of household vegetable oil to approximately 70°C. The magnetic core at room temperature was submerged into the

70°C oil. When the temperature of the core began to change, the trigger of the arbitrary function generator excited the core with a sinusoidal waveform at approximately three kilohertz for three cycles. The magnitude of the saturation magnetization was used to determine the temperature of the core, and the change in the width of the ***B-H*** loop was examined.

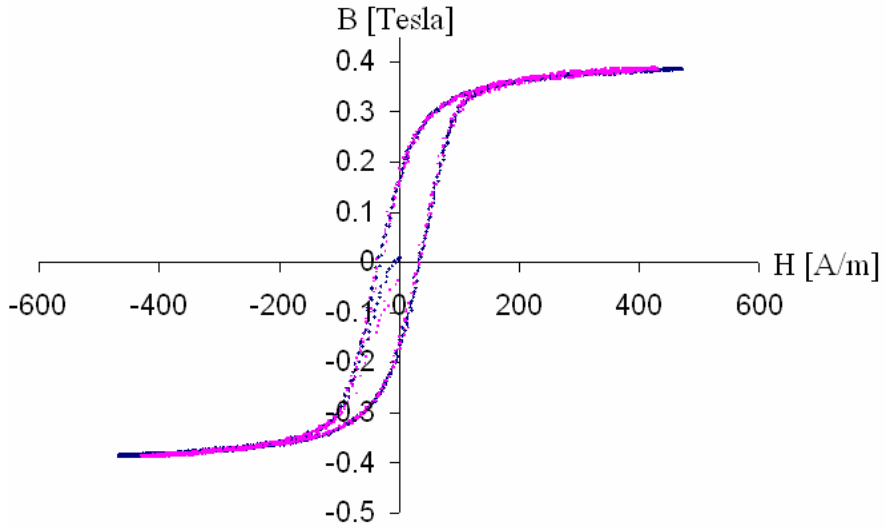

Figure 4.16 Dynamic heating experiment showing two ***B-H*** curves at the same temperature. Both curves overlap each other. The heat flux into or out of the core has no effect on the ***B-H*** characteristics of the core. The ***B-H*** characteristic is only a function of the present temperature of the core.

4.4. Dynamic Temperature Simulation

In formulating a proper dynamic model for the heat flux, it can be said with certainty due to the results from the previous section that the pinning loss or hysteresis loss rather of the core is directly responsible for core temperature rise at low frequencies. Therefore, the Jiles-Atherton model has been reformulated in terms of time using the following substitution

$$\frac{dM(H)}{dH} = \frac{\frac{dM(t)}{dt}}{\frac{dH(t)}{dt}} \qquad 4.10$$

The new model in terms of time takes the form

$$M_{irr}(t) = M_{an}(t) - \frac{\delta(t) \cdot k \left(\frac{\mathrm{d}}{\mathrm{d}t} M_{irr}(t) \right)}{\frac{\mathrm{d}}{\mathrm{d}t} H(t) + \alpha \left(\frac{\mathrm{d}}{\mathrm{d}t} M_{irr}(t) \right)} \qquad 4.11$$

with $M_{an}(t)$ being placed in terms of time by replacing H with its associated time-varying function. In this way, $M_{an}(t)$ creates a time varying waveform that it used to predict $M(t)$ can be predicted. $M_{an}(t)$ is given by the following equation

$$M_{an}(t) = \frac{2 M_S}{\left(1 + \mathrm{e}^{\frac{-H(t)}{Hf}} \right)} - M_S \qquad 4.12$$

where the time base is due to the applied field, $H(t)$. Having $M(t)$ in terms of time allows the heat equation to combined, allows the hysteresis loss to be dynamically predicted, and therefore allows the heat equation to predict the temperature rise. Higher frequency would follow the same method. Figure 3.17 shows the simulation of the $M_{an}(t)$ now as a waveform. Such a waveform would exist in the MnZn ferrite tested in these experiments if hysteresis loss did not exist.

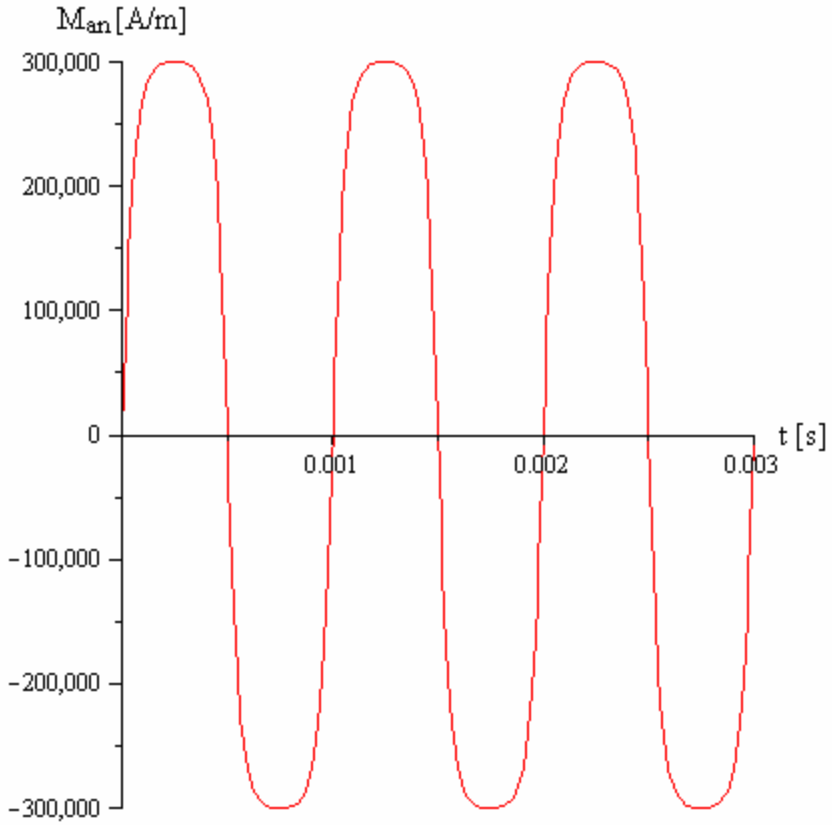

Figure 4.17 Prediction of the $M_{an}(t)$ waveform as a function of time. The time-based $M_{an}(t)$ is used to predict $M(t)$. Once applied with the remainder of the model, simple application of Faraday's Law will yield a prediction of the corresponding voltage waveform.

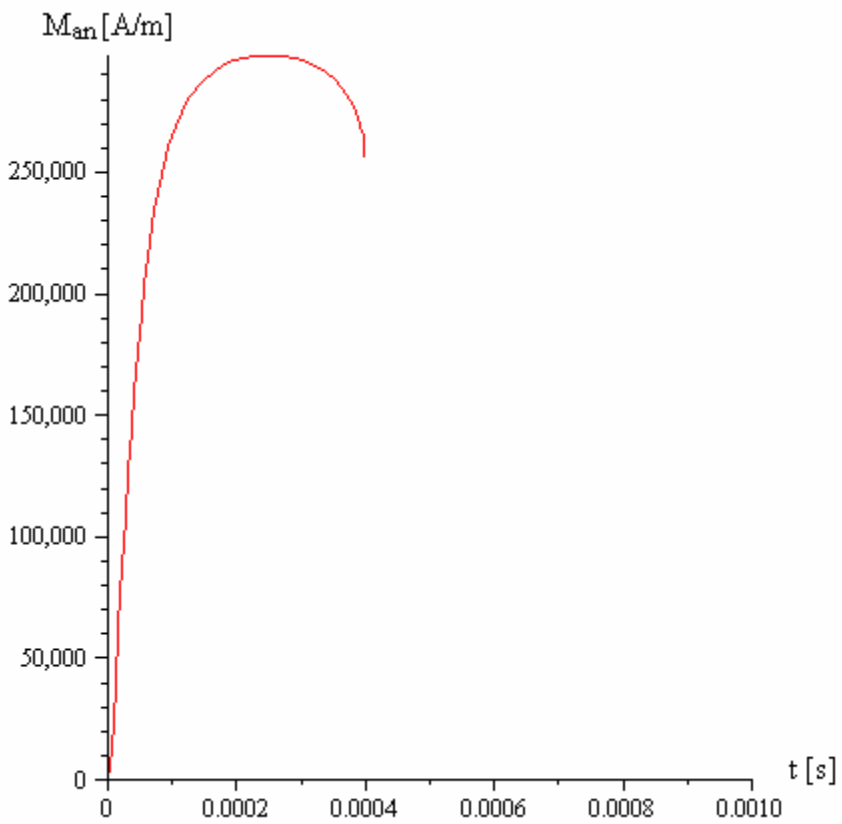

Figure 4.18 Dynamic prediction of the magnitude of ***M(t)***. A periodic singularity now exists in the model equation due to the emergence of two time based derivatives in the denominator of the pinning loss term.

If the model is to be truly dynamic, then the static model must be evaluated at the instantaneous temperature. To evaluate the instantaneous temperature, the heat equation is symbolically solved in cylindrical coordinates for Robin conditions (i.e., Newton's Law of Cooling) on each side of a cylinder that is equal to the dimensions of the core [37]. The forcing function of the heat equation (internal heating) is then related directly to the pinning loss that has now a function of time by the thermal diffusivity of the material as proven by the previous set of dynamic experiments. The expression for

temperature is then substituted out of the model and the remaining model expression can be evaluated for ***M(t)***.

The following is the analytical expression governing the instantaneous temperature of the core that was formulated with the aid of USFKAD [50]. For this expression the thermal diffusivity is considered a constant, and is added to the final expression once a numerical approximation is performed. For the expression below, $f_{interrior}$, denotes the substitution of the pinning expression and Ψ denotes the present temperature of the core.

$$\Psi = \Psi_{steady\ state} + \Psi_{transient}$$

$$\Psi_{steady\ state} = \Psi_1 + \Psi_2 + \Psi_3 + \Psi_4 + \Psi_5$$

$$\Psi_1 = \sum_{\kappa_\theta=-\infty}^{\infty} \sum_{\kappa_{r\,\vartheta}} e^{i\kappa_\theta\theta} \{[\alpha_a Y_{\kappa_\theta}(\kappa_{r:\vartheta}a) + \kappa_{r:\vartheta} Y'_{\kappa_\theta}(\kappa_{r:\vartheta}a)] J_{\kappa_\theta}(\kappa_{r\,\vartheta}r) - [\alpha_a J_{\kappa_\theta}(\kappa_{r:\vartheta}a) + \kappa_{r\,\vartheta} J'_{\kappa_\theta}(\kappa_{r\,\vartheta}a)] Y_{\kappa_\theta}(\kappa_{r:\vartheta}r)\}$$
$$\times \quad \eta_z(z;\kappa_{r\,\vartheta})\ A(\kappa_\theta, \kappa_{r\,\vartheta})$$

where

$\{\kappa_{r\,\vartheta}\}$ are the roots of
$[\alpha_a Y_{\kappa_\theta}(\kappa_{r:\vartheta}a) + \kappa_{r\,\vartheta} Y'_{\kappa_\theta}(\kappa_{r\,\vartheta}a)][\alpha_b J_{\kappa_\theta}(\kappa_{r:\vartheta}b) + \kappa_{r\,\vartheta} J'_{\kappa_\theta}(\kappa_{r:\vartheta}b)] = [\alpha_a J_{\kappa_\theta}(\kappa_{r:\vartheta}a) + \kappa_{r\,\vartheta} J'_{\kappa_\theta}(\kappa_{r\,\vartheta}a)][\alpha_b Y_{\kappa_\theta}(\kappa_{r\,\vartheta}b) + \kappa_{r\,\vartheta} Y'_{\kappa_\theta}(\kappa_{r\,\vartheta}b)]$

$$\eta_z(z;\kappa_{r\,\vartheta}) = \begin{cases} 1 + \alpha_Z(Z - z) \text{ if } \kappa_{r\,\vartheta} = 0; \text{ otherwise} \\ \kappa_{r\,\vartheta} \cosh \kappa_{r:\vartheta}(Z - z) + \alpha_Z \sinh \kappa_{r\,\vartheta}(Z - z) \end{cases}$$

$$A(\kappa_\theta, \kappa_{r:\vartheta}) = \int_0^{2\pi} d\theta \int_a^b dr\ e^{-i\kappa_\theta\theta} \frac{1}{2\pi}$$
$$\times \{[\alpha_a Y_{\kappa_\theta}(\kappa_{r:\vartheta}a) + \kappa_{r:\vartheta} Y'_{\kappa_\theta}(\kappa_{r:\vartheta}a)] J_{\kappa_\theta}(\kappa_{r\,\vartheta}r) - [\alpha_a J_{\kappa_\theta}(\kappa_{r\,\vartheta}a) + \kappa_{r\,\vartheta} J'_{\kappa_\theta}(\kappa_{r\,\vartheta}a)] Y_{\kappa_\theta}(\kappa_{r:\vartheta}r)\} r\ N_{\kappa_{r\,\vartheta}}\ M_{\kappa_{r\,\vartheta}}\ f_{z=0}(\theta, r)$$

$$N_{\kappa_{r\,\vartheta}} = \{\int_a^b \{[\alpha_a Y_{\kappa_\theta}(\kappa_{r:\vartheta}a) + \kappa_{r\,\vartheta} Y'_{\kappa_\theta}(\kappa_{r\,\vartheta}a)] J_{\kappa_\theta}(\kappa_{r:\vartheta}r)$$
$$- [\alpha_a J_{\kappa_\theta}(\kappa_{r:\vartheta}a) + \kappa_{r\,\vartheta} J'_{\kappa_\theta}(\kappa_{r:\vartheta}a)] Y_{\kappa_\theta}(\kappa_{r\,\vartheta}r)\}^2 r\ dr\}^{-1}$$

$$M_{\kappa_{r\,\vartheta}} = \begin{cases} \frac{1}{\alpha_{z=0}(1+\alpha_Z Z) - \alpha_Z} \text{ if } \kappa_{r:\vartheta} = 0; \text{ otherwise,} \\ \frac{1}{\alpha_{z=0}(K \cosh KZ + \alpha_Z \sinh KZ) - K(K \sinh KZ + \alpha_Z \cosh KZ)} \\ (\text{ where } K = \kappa_{r:\vartheta}) \end{cases}$$

$\Psi_2 = \sum_{\kappa_\theta=-\infty}^{\infty} \sum_{\kappa_z} \; e^{i\kappa_\theta \theta} \; \eta_z(z;\kappa_z) \; \eta_r(r,\kappa_\theta,\kappa_z) \; A(\kappa_\theta,\kappa_z)$
where

$\eta_z(z;\kappa_z) = \sin[\kappa_z z + \arctan(\frac{-\kappa_z}{\alpha_{z=0}})]$ where $\{\kappa_z\}$ are the nonzero solutions (maybe imaginary) to $-\alpha_Z \sin[\kappa_z Z + \arctan(\frac{-\kappa_z}{\alpha_{z=0}})] = \kappa_z \cos[\kappa_z Z + \arctan(\frac{-\kappa_z}{\alpha_{z=0}})]$;
also if $\alpha_Z - \alpha_Z \alpha_{z=0} Z - \alpha_{z=0} = 0$ include $\kappa_z = 0, \eta_z(z;0) = 1 - \alpha_{z=0} z$.

$$\eta_r(r,\kappa_\theta,\kappa_z) = \begin{cases} \alpha_b \ln \frac{r}{b} - \frac{1}{b} \text{ if } \kappa_\theta = \kappa_z = 0; \\ \kappa_\theta \cosh(\kappa_\theta \ln \frac{r}{b}) - b\alpha_b \sinh(\kappa_\theta \ln \frac{r}{b}) \text{ if } \kappa_\theta \neq 0 \text{ and } \kappa_z = 0; \text{ otherwise} \\ [\alpha_b K_{\kappa_\theta}(\kappa_z b) + \kappa_z K'_{\kappa_\theta}(\kappa_z b)] I_{\kappa_\theta}(\kappa_z r) \\ \quad -[\alpha_b I_{\kappa_\theta}(\kappa_z b) + \kappa_z I'_{\kappa_\theta}(\kappa_z b)] K_{\kappa_\theta}(\kappa_z r) \\ (\text{ use } I_{-\kappa_\theta} \text{ for } K_{\kappa_\theta} \text{ if } \kappa_\theta \text{ is not an integer.}) \end{cases}$$

$A(\kappa_\theta,\kappa_z) = \int_0^{2\pi} d\theta \int_0^Z dz \; e^{-i\kappa_\theta \theta} \; \frac{1}{2\pi} \; \eta_z(z;\kappa_z) \; N_{\kappa_z} \; N_r \; f_{r=a}(\theta, z)$

$$N_{\kappa_z} = \begin{cases} \frac{3}{3Z - 3\alpha_{z=0} Z^2 + \alpha_{z=0}^2 Z^3} & \text{if } \kappa_z = 0; \\ \frac{2}{Z + \frac{\alpha_Z}{\alpha_Z{}^2 + \kappa_z{}^2} - \frac{\alpha_{z=0}}{\alpha_{z=0}^2 + \kappa_z{}^2}} & \text{otherwise.} \end{cases}$$

$N_r = \frac{1}{\alpha_a \eta_r(a,\kappa_\theta,\kappa_z) + \frac{\partial}{\partial r}\eta_r(r,\kappa_\theta,\kappa_z)\big]_{r=a}}$

$\Psi_3 = \sum_{\kappa_\theta=-\infty}^{\infty} \sum_{\kappa_{r\,\vartheta}} \; e^{i\kappa_\theta \theta} \; \{[\alpha_a Y_{\kappa_\theta}(\kappa_{r:\vartheta} a) + \kappa_{r:\vartheta} Y'_{\kappa_\theta}(\kappa_{r:\vartheta} a)] J_{\kappa_\theta}(\kappa_{r\,\vartheta} r) - [\alpha_a J_{\kappa_\theta}(\kappa_{r:\vartheta} a) + \kappa_{r\,\vartheta} J'_{\kappa_\theta}(\kappa_{r\,\vartheta} a)] Y_{\kappa_\theta}(\kappa_{r:\vartheta} r)\}$
$\times \quad \eta_z(z;\kappa_{r\,\vartheta}) \; A(\kappa_\theta,\kappa_{r\,\vartheta})$
where

$\{\kappa_{r\,\vartheta}\}$ are the roots of
$[\alpha_a Y_{\kappa_\theta}(\kappa_{r:\vartheta} a) + \kappa_{r\,\vartheta} Y'_{\kappa_\theta}(\kappa_{r\,\vartheta} a)][\alpha_b J_{\kappa_\theta}(\kappa_{r:\vartheta} b) + \kappa_{r\,\vartheta} J'_{\kappa_\theta}(\kappa_{r:\vartheta} b)] = [\alpha_a J_{\kappa_\theta}(\kappa_{r:\vartheta} a) + \kappa_{r\,\vartheta} J'_{\kappa_\theta}(\kappa_{r\,\vartheta} a)][\alpha_b Y_{\kappa_\theta}(\kappa_{r\,\vartheta} b) + \kappa_{r\,\vartheta} Y'_{\kappa_\theta}(\kappa_{r\,\vartheta} b)]$

$$\eta_z(z;\kappa_{r\,\vartheta}) = \begin{cases} 1 - \alpha_{z=0} z \text{ if } \kappa_{r\,\vartheta} = 0; \text{ otherwise,} \\ \kappa_{r\,\vartheta} \cosh \kappa_{r:\vartheta} z - \alpha_{z=0} \sinh \kappa_{r\,\vartheta} z \end{cases}$$

$A(\kappa_\theta,\kappa_{r:\vartheta}) = \int_0^{2\pi} d\theta \int_a^b dr \; e^{-i\kappa_\theta \theta} \; \frac{1}{2\pi}$
$\times \; \{[\alpha_a Y_{\kappa_\theta}(\kappa_{r:\vartheta} a) + \kappa_{r:\vartheta} Y'_{\kappa_\theta}(\kappa_{r:\vartheta} a)] J_{\kappa_\theta}(\kappa_{r\,\vartheta} r) - [\alpha_a J_{\kappa_\theta}(\kappa_{r\,\vartheta} a) + \kappa_{r\,\vartheta} J'_{\kappa_\theta}(\kappa_{r\,\vartheta} a)] Y_{\kappa_\theta}(\kappa_{r:\vartheta} r)\} r \; N_{\kappa_{r\,\vartheta}} \; M_{\kappa_{r\,\vartheta}} \; f_{z=Z}(\theta, r)$

$N_{\kappa_{r\,\vartheta}} = \{\int_a^b \{[\alpha_a Y_{\kappa_\theta}(\kappa_{r:\vartheta} a) + \kappa_{r\,\vartheta} Y'_{\kappa_\theta}(\kappa_{r\,\vartheta} a)] J_{\kappa_\theta}(\kappa_{r:\vartheta} r)$
$- [\alpha_a J_{\kappa_\theta}(\kappa_{r:\vartheta} a) + \kappa_{r\,\vartheta} J'_{\kappa_\theta}(\kappa_{r:\vartheta} a)] Y_{\kappa_\theta}(\kappa_{r\,\vartheta} r)\}^2 r \; dr\}^{-1}$

$$M_{\kappa_{r\,\vartheta}} = \begin{cases} \frac{1}{\alpha_Z(1 - \alpha_{z=0} Z) - \alpha_{z=0}} \text{ if } \kappa_{r\,\vartheta} = 0; \text{ otherwise,} \\ \frac{1}{\alpha_Z[K \cosh KZ - \alpha_{z=0} \sinh KZ] + K[K \sinh KZ - \alpha_Z \cosh KZ]} \\ (\text{ where } K = \kappa_{r:\vartheta}) \end{cases}$$

$\Psi_4 = \sum_{\kappa_\theta=-\infty}^{\infty} \sum_{\kappa_z} \; e^{i\kappa_\theta \theta} \; \eta_z(z;\kappa_z) \; \eta_r(r,\kappa_\theta,\kappa_z) \; A(\kappa_\theta,\kappa_z)$
where

$\eta_z(z;\kappa_z) = \sin[\kappa_z z + \arctan(\frac{-\kappa_z}{\alpha_{z=0}})]$ where $\{\kappa_z\}$ are the nonzero solutions (maybe imaginary) to $-\alpha_Z \sin[\kappa_z Z + \arctan(\frac{-\kappa_z}{\alpha_{z=0}})] = \kappa_z \cos[\kappa_z Z + \arctan(\frac{-\kappa_z}{\alpha_{z=0}})]$;
also if $\alpha_Z - \alpha_Z \alpha_{z=0} Z - \alpha_{z=0} = 0$ include $\kappa_z = 0, \eta_z(z;0) = 1 - \alpha_{z=0} z$.

$$\eta_r(r,\kappa_\theta,\kappa_z) = \begin{cases} \alpha_a \ln\frac{r}{a} - \frac{1}{a} \text{ if } \kappa_\theta = \kappa_z = 0; \\ \kappa_\theta \cosh(\kappa_\theta \ln\frac{r}{a}) - a\alpha_a \sinh(\kappa_\theta \ln\frac{r}{a}) \text{ if } \kappa_\theta \neq 0 \text{ and } \kappa_z = 0; \text{ otherwise} \\ [\alpha_a K_{\kappa_\theta}(\kappa_z a) + \kappa_z K'_{\kappa_\theta}(\kappa_z a)] I_{\kappa_\theta}(\kappa_z r) \\ \quad -[\alpha_a I_{\kappa_\theta}(\kappa_z a) + \kappa_z I'_{\kappa_\theta}(\kappa_z a)] K_{\kappa_\theta}(\kappa_z r) \\ (\text{ use } I_{-\kappa_\theta} \text{ for } K_{\kappa_\theta} \text{ if } \kappa_\theta \text{ is not an integer.}) \end{cases}$$

$A(\kappa_\theta,\kappa_z) = \int_0^{2\pi} d\theta \int_0^Z dz \; e^{-i\kappa_\theta\theta} \; \frac{1}{2\pi} \; \eta_z(z;\kappa_z) \; N_{\kappa_z} \; N_r \; f_{r=b}(\theta,z)$

$$N_{\kappa_z} = \begin{cases} \frac{3}{3Z - 3\alpha_{z=0} Z^2 + \alpha_{z=0}^2 Z^3} & \text{if } \kappa_z = 0; \\ \frac{2}{Z + \frac{\alpha_Z}{\alpha_Z{}^2 + \kappa_z{}^2} - \frac{\alpha_{z=0}}{\alpha_{z=0}^2 + \kappa_z{}^2}} & \text{otherwise.} \end{cases}$$

$$N_r = \frac{1}{\alpha_b \eta_r(b,\kappa_\theta,\kappa_z) + \left[\frac{\partial}{\partial r}\eta_r(r,\kappa_\theta,\kappa_z)\right]_{r=b}}$$

$\Psi_5 = \sum_{\kappa_\theta=-\infty}^{\infty} \sum_{\kappa_z} \sum_{\kappa_{r\,\theta}} \; e^{i\kappa_\theta\theta} \; \eta_z(z;\kappa_z) \; \{[\alpha_a Y_{\kappa_\theta}(\kappa_{r:\theta} a) + \kappa_{r\,\theta} Y'_{\kappa_\theta}(\kappa_{r\,\theta} a)] J_{\kappa_\theta}(\kappa_{r:\theta} r) -$
$[\alpha_a J_{\kappa_\theta}(\kappa_{r\,\theta} a) + \kappa_{r\,\theta} J'_{\kappa_\theta}(\kappa_{r\,\theta} a)] Y_{\kappa_\theta}(\kappa_{r:\theta} r)\}$
$\times \quad A(\kappa_{r\,\theta}, \kappa_\theta, \kappa_z)$
where

$\eta_z(z;\kappa_z) = \sin[\kappa_z z + \arctan(\frac{-\kappa_z}{\alpha_{z=0}})]$ where $\{\kappa_z\}$ are the nonzero solutions (maybe imaginary) to $-\alpha_Z \sin[\kappa_z Z + \arctan(\frac{-\kappa_z}{\alpha_{z=0}})] = \kappa_z \cos[\kappa_z Z + \arctan(\frac{-\kappa_z}{\alpha_{z=0}})]$;
also if $\alpha_Z - \alpha_Z \alpha_{z=0} Z - \alpha_{z=0} = 0$ include $\kappa_z = 0, \eta_z(z;0) = 1 - \alpha_{z=0} z$.

$\{\kappa_{r\,\theta}\}$ are the roots of
$[\alpha_a Y_{\kappa_\theta}(\kappa_{r:\theta} a) + \kappa_{r\,\theta} Y'_{\kappa_\theta}(\kappa_{r\,\theta} a)][\alpha_b J_{\kappa_\theta}(\kappa_{r:\theta} b) + \kappa_{r\,\theta} J'_{\kappa_\theta}(\kappa_{r:\theta} b)] = [\alpha_a J_{\kappa_\theta}(\kappa_{r:\theta} a) +$
$\kappa_{r\,\theta} J'_{\kappa_\theta}(\kappa_{r\,\theta} a)][\alpha_b Y_{\kappa_\theta}(\kappa_{r\,\theta} b) + \kappa_{r\,\theta} Y'_{\kappa_\theta}(\kappa_{r\,\theta} b)]$

$A(\kappa_{r\,\theta}, \kappa_\theta, \kappa_z) = \int_0^{2\pi} d\theta \int_0^Z dz \int_a^b dr \; e^{-i\kappa_\theta\theta} \; \frac{1}{2\pi} \; \eta_z(z;\kappa_z) \; N_{\kappa_z}$

$\times \{[\alpha_a Y_{\kappa_\theta}(\kappa_{r:\theta} a) + \kappa_{r:\theta} Y'_{\kappa_\theta}(\kappa_{r:\theta} a)] J_{\kappa_\theta}(\kappa_{r\,\theta} r) - [\alpha_a J_{\kappa_\theta}(\kappa_{r\,\theta} a) +$
$\kappa_{r\,\theta} J'_{\kappa_\theta}(\kappa_{r\,\theta} a)] Y_{\kappa_\theta}(\kappa_{r:\theta} r)\} r \; N_{\kappa_{r\,\theta}}$
$\times \frac{f_{interior}(r,\theta,z)}{\kappa_{r\,\theta}^2 + \kappa_z^2}$

$$N_{\kappa_z} = \begin{cases} \frac{3}{3Z - 3\alpha_{z=0} Z^2 + \alpha_{z=0}^2 Z^3} & \text{if } \kappa_z = 0; \\ \frac{2}{Z + \frac{\alpha_Z}{\alpha_Z{}^2 + \kappa_z{}^2} - \frac{\alpha_{z=0}}{\alpha_{z=0}^2 + \kappa_z{}^2}} & \text{otherwise.} \end{cases}$$

$N_{\kappa_{r\,\theta}} = \{\int_a^b \{[\alpha_a Y_{\kappa_\theta}(\kappa_{r:\theta} a) + \kappa_{r\,\theta} Y'_{\kappa_\theta}(\kappa_{r\,\theta} a)] J_{\kappa_\theta}(\kappa_{r:\theta} r)$
$- [\alpha_a J_{\kappa_\theta}(\kappa_{r:\theta} a) + \kappa_{r\,\theta} J'_{\kappa_\theta}(\kappa_{r:\theta} a)] Y_{\kappa_\theta}(\kappa_{r\,\theta} r)\}^2 r \, dr\}^{-1}$

$$\Psi_{transient} = \sum_{\kappa_\theta=-\infty}^{\infty} \sum_{\kappa_z} \sum_{\kappa_{r\,g}} e^{i\kappa_\theta\theta}\ \eta_z(z;\kappa_z)\ \{[\alpha_a Y_{\kappa_\theta}(\kappa_{r\,g}a) + \kappa_{r:g} Y'_{\kappa_\theta}(\kappa_{r:g}a)] J_{\kappa_\theta}(\kappa_{r\,g}r) - [\alpha_a J_{\kappa_\theta}(\kappa_{r\,g}a) + \kappa_{r\,g} J'_{\kappa_\theta}(\kappa_{r\,g}a)] Y_{\kappa_\theta}(\kappa_{r:g}r)\}$$
$$\times$$
$$e^{-(\kappa_{r\,g}^2+\kappa_z^2)t}\ A(\kappa_{r\,g},\kappa_\theta,\kappa_z)$$

where

$\eta_z(z;\kappa_z) = \sin[\kappa_z z + \arctan(\frac{-\kappa_z}{\alpha_{z=0}})]$ where $\{\kappa_z\}$ are the nonzero solutions (maybe imaginary) to $-\alpha_Z \sin[\kappa_z Z + \arctan(\frac{-\kappa_z}{\alpha_{z=0}})] = \kappa_z \cos[\kappa_z Z + \arctan(\frac{-\kappa_z}{\alpha_{z=0}})]$;
also if $\alpha_Z - \alpha_Z\alpha_{z=0}Z - \alpha_{z=0} = 0$ include $\kappa_z = 0, \eta_z(z;0) = 1 - \alpha_{z=0}z$.

$\{\kappa_{r\,g}\}$ are the roots of
$[\alpha_a Y_{\kappa_\theta}(\kappa_{r:g}a) + \kappa_{r\,g} Y'_{\kappa_\theta}(\kappa_{r\,g}a)][\alpha_b J_{\kappa_\theta}(\kappa_{r:g}b) + \kappa_{r\,g} J'_{\kappa_\theta}(\kappa_{r:g}b)] = [\alpha_a J_{\kappa_\theta}(\kappa_{r:g}a) + \kappa_{r\,g} J'_{\kappa_\theta}(\kappa_{r\,g}a)][\alpha_b Y_{\kappa_\theta}(\kappa_{r\,g}b) + \kappa_{r\,g} Y'_{\kappa_\theta}(\kappa_{r\,g}b)]$

$$A(\kappa_{r\,g},\kappa_\theta,\kappa_z) = \int_0^{2\pi} d\theta \int_0^Z dz \int_a^b dr\ e^{-i\kappa_\theta\theta}\ \tfrac{1}{2\pi}\ \eta_z(z;\kappa_z)\ N_{\kappa_z} \times \{[\alpha_a Y_{\kappa_\theta}(\kappa_{r:g}a) + \kappa_{r:g} Y'_{\kappa_\theta}(\kappa_{r:g}a)] J_{\kappa_\theta}(\kappa_{r\,g}r) - [\alpha_a J_{\kappa_\theta}(\kappa_{r\,g}a) + \kappa_{r\,g} J'_{\kappa_\theta}(\kappa_{r\,g}a)] Y_{\kappa_\theta}(\kappa_{r:g}r)\} r\ N_{\kappa_{r\,g}} \times [\Psi(r,\theta,z;0) - \Psi_{steady\ state}]$$

$$N_{\kappa_z} = \begin{cases} \frac{3}{3Z - 3\alpha_{z=0}Z^2 + \alpha_{z=0}^2 Z^3} & \text{if } \kappa_z = 0; \\ \frac{2}{Z + \frac{\alpha_Z}{\alpha_Z{}^2 + \kappa_z{}^2} - \frac{\alpha_{z=0}}{\alpha_{z=0}^2 + \kappa_z{}^2}} & \text{otherwise.} \end{cases}$$

$$N_{\kappa_{r\,g}} = \{\int_a^b \{[\alpha_a Y_{\kappa_\theta}(\kappa_{r:g}a) + \kappa_{r\,g} Y'_{\kappa_\theta}(\kappa_{r\,g}a)] J_{\kappa_\theta}(\kappa_{r:g}r) - [\alpha_a J_{\kappa_\theta}(\kappa_{r:g}a) + \kappa_{r\,g} J'_{\kappa_\theta}(\kappa_{r:g}a)] Y_{\kappa_\theta}(\kappa_{r\,g}r)\}^2 r\ dr\}^{-1}$$

4.5. Chapter Summary

The measurement of the anhysteretic magnetization curve as function of temperature was performed with the magnetization characterization system. A highly-accurate curve-fit for the anhysteretic magnetization curve was performed for a commercially-available, MnZn ferrite magnetic core. Parameter extraction for the purpose of modeling the magnetic core as a function of temperature was performed. All model parameters including the anhysteretic magnetization curve have been given a static temperature dependence. A dynamic temperature dependence was described, but the comparison to measured data is left to future work. Using this static temperature dependence, predictions of ***M-H*** loops were made based upon the measured curves. Correlation of experimental and predicted results was good.

A series of dynamic experiments were setup to investigate the effect of a heat flux on the core from the environment. In this set of experiments, a MnZn ferrite core was dropped in a bath of oil at substantially higher temperature (i.e., approximately 70°C). The heat flux on the core was shown to have no effect on the ***B-H*** characteristics of the core. This indicated as shown in Chapter 2 that the heat loss is directly related to the hysteresis loss of the core and that the hysteresis loss can be used to predict the temperature rise of the core.

An expression for the temperature of the core including dynamic heating was formulated using USFKAD [50]. The expression was found by solving the non-homogenous heat equation with Robin boundary conditions on each side to represent the cooling of the core as a function of time. The expression of temperature contains the forcing function, $f_{interrior}$, to denote the heating caused by the pinning term. A complete dynamic expression for ***M(t)*** can then be formulated. Comparison to of this dynamic heating expression to measured data is left to future work.

Chapter 5: Frequency Dependent Results.

5.1. Experimental Procedure and Results

It was postulated in Chapter 2 that the anhysteretic magnetization curve would essentially change shape depending on the frequency of the applied demagnetizing waveform. In applying higher frequency demagnetizing waveform, it was thought possible that the magnetic domains could not return to their equilibrium condition as represented by the low frequency anhysteretic magnetization curve.

To test this hypothesis, the characterization system of Chapter 2 was used with a modification of the demagnetizing waveform. The pauses in the demagnetizing waveform that were placed with the intent of regulating the core temperature were removed. Two hundred cycles of a continuous decaying sinusoid was programmed. The magnitude of the applied field was kept substantially high past the knee of the ***M*-*H*** loop where it is prescribed by IEEE standard [45] to demagnetize the core. The demagnetization process and biasing process as described in Chapter 3 were performed at several different frequencies. In doing so, the demagnetizing waveform was made contentious. The following results were obtained for demagnetizing frequencies of 10kHz, 50kHz, and 100kHz.

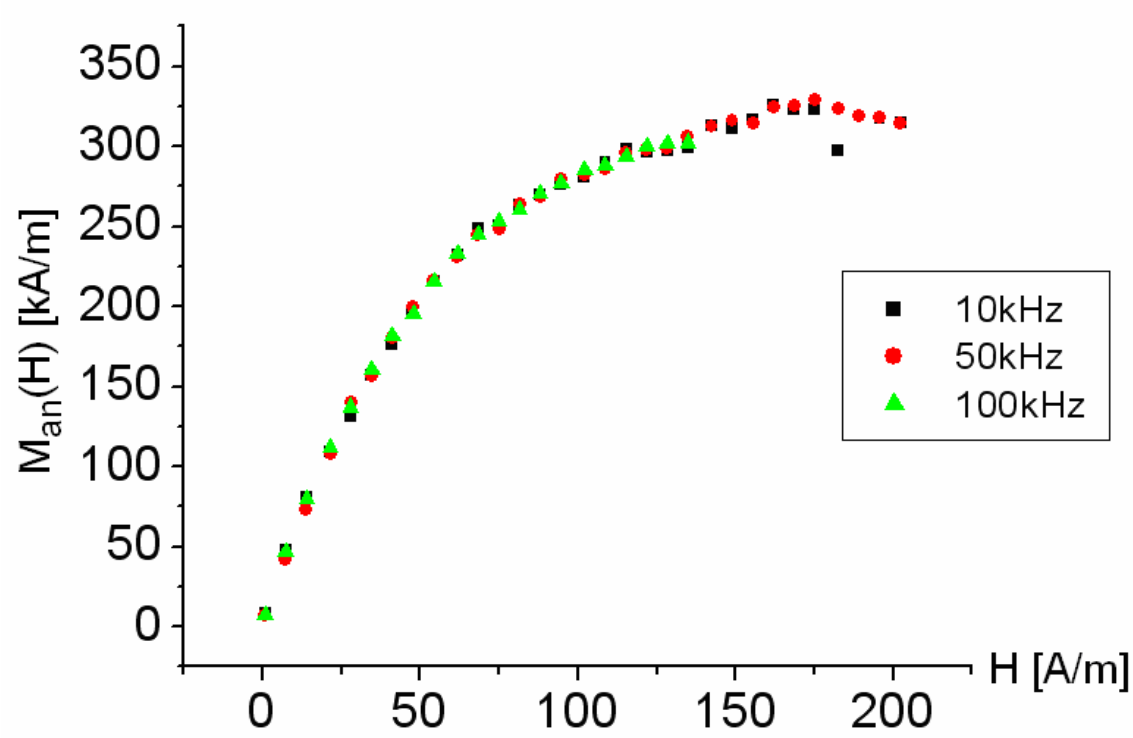

Figure 5.1 $M_{an}(H)$ measured with different demagnetizing frequencies. The curve was measured at 30°C for a MnZn ferrite.

The decline of $M_{an}(H)$ in saturation observed in Figure 5.1has been witnessed in the measurement of the anhysteretic magnetization in the area of magnetic recording media [51]. How the mechanisms involved in particular the inability of the core to reach true equilibrium would be the subject of future work.

The most striking characteristic of the curve is that the initial rise of the curve has not been altered by a change in the frequency of the applied field. From a modeling point of view, it indicates a few possibilities. Either no steady state anhysteretic magnetization curve exists. The curve cannot be approached properly. The overall effect is negligible for the experimental range investigated. The physical loss at higher frequencies is too small for the volume of the core under test.

5.2. Chapter Summary

The anhysteretic magnetization curve of magnetic core was measured by applying a sequence of higher-frequency demagnetizing waveforms at constant temperature. The response of the demagnetizing waveforms was compared, and a change in saturation was noted. The behavior of the waveforms will be the subject of future work.

Chapter 6: Conclusions and Future Work

Present day electrical systems depend heavily on the area of power conversion to supply highly efficient power conversion systems. A major component paving the way for power conversion is the switching power supply, which depends heavily on high-frequency transformers. This high-frequency operation is a direct result of the shrinking of the magnetic core used to construct transformers and inductors as the shrinkage of volume of the core greatly reduces the power loss in the core and the volume occupied by the core.

The nonlinear *I-V* characteristics of the core depend on the ***B-H*** characteristics core. This fundamental relationship is usually termed hysteretic in that the present value of ***B*** depends on the past value of ***B***. This nonlinear behavior is difficult to predict and can changes as a function of temperature and frequency. In the area of power electronics the application of nonlinear waveforms further complicate the prediction of a magnetic component's *I-V* characteristics.

To aid in the design of electrical systems especially power electronics, the development of a mathematical model began. In particular, it was noted that because of the nonlinearities involved with temperature and frequency that the modern Spice based model, namely the Jiles-Atherton model, did not possess a temperature or frequency dependence.

The Jiles-Atherton model was investigated, and it was found to depend upon the anhysteretic magnetization of a magnetic core. The anhysteretic magnetization of a core has two fundamental definitions. In the Jiles-Atherton model it is known to be the defect free magnetization. This is due to theory that hysteresis is caused by a sort of frictional loss that results in the material due to the application of an applied magnetic field. The anhysteretic magnetization is also theorized to be thermodynamic equilibrium.

Because the effects of temperature could be separated from frequency effects at low frequencies of operation, the modification of the Jiles-Atherton model to posses a temperature dependency was approached first. The research therefore concentrated on the measurement and modeling of the anhysteretic magnetization, which is a singled valued function that could be measured and modeled mathematically. In doing so, the basic temperature model could be formed.

During the investigation of the anhysteretic magnetization curve, it was found that several different functions existed to represent the curve. Each expression for the anhysteretic curve existed not for the purpose of temperature, but for the purpose of describing the anisotropy and texture of the material. None of the present equations correctly model the temperature effects of the core with Jiles noting himself that the original model did not have a temperature dependence.

To aid in the research and measurement of the anhysteretic magnetization, an experimental setup was constructed consisting of drive electron, a programmable function generator, a customized test cell with heating capabilities, and a control program designed to measure both the ***B*-*H*** loop and the anhysteretic magnetization curve. During

the design of the system, it was found that no method existed for measuring the anhysteretic magnetization of a core without cutting the core. In doing so, the characteristics being measured would change. The primary difficulty in measuring the anhysteretic magnetization of a magnetic core was that it requires the reading of a static in time $\boldsymbol{B}$ field (i.e., no induced voltage would be present on the core to read the field.)

The system was constructed with the advent of a new methodology to measure the anhysteretic magnetization by applying a sinusoidal magnetic field to the core by the application of two independent current sources. Data for the anhysteretic magnetization was measured as a function of temperature, and the anhysteretic curve was modeled as a function of temperature.

While a primary difficulty in the Jiles-Atherton model is known to be the parameter extraction process, the singled-valued function modeled using the described measurement technique eased the process. This is mainly due to the ability to know the anhysteretic magnetization directly instead of attempting to model it based on theory. The overall extraction process for the model parameters is then simplified.

For dynamic temperature performance, it was found that the $\boldsymbol{I}$-$\boldsymbol{V}$ behavior of the magnetic core depends solely on the present temperature of the core. This was proven by a set of dynamic experiments in which a temperature gradient was created around a core sample using heated oil. An equation describing the present temperature of the core was formulated using USFKAD with the internal self-heating of the core based on the energy loss due to hysteresis.

In examining the frequency dependent effects of hysteresis, it was noted that Jiles attempted previously to add frequency dependent effects to the model while neglecting

temperature dependent effects. The equation was reconstructed under a different set of assumptions. The proving of this equation is left to future work.

It was also postulated, that the anhysteretic magnetization curve could form a type of steady state frequency dependency. In other words, the core would not return to thermal equilibrium or the actual anhysteretic magnetization curve because the material would not be allowed to relax at higher frequencies. A set of experiments was performed to test this hypothesis. The magnetic core was demagnetized at different frequencies and its value was measured. While the results are different than that of the low-frequency, anhysteretic magnetization curves, the interpretation of the results is not fully understood. The remaining frequency work and its interpretation is left to future work.

References

[1] "Generation and Consumption of Fuels for Electricity Generation", Energy Information Administration/ Electric Power Monthly May 2007.

[2] IDC, "IDC's Worldwide Quarterly PC Tracker," IDC, Press Release 2007.

[3] CTIA, "End-of-Year 2006 Top-Line Survey Results," 2006.

[4] N. Mohan, T. M. Undeland, and W. P. Robbins, *Power Electronics Converters, Applications, and Design 3rd Eddition*. Hoboken, NJ: John Wiley & Sons, 2003.

[5] C. Calwell and T. Reeder, "Power Supplies: A Hidden Opportunity for Savings," NRDC, San Francisco 2002.

[6] A. I. Pressman, *Switching Power Supply Dsign*, 2nd ed. Dubuque, IA McGraw-Hill Professional, 1997.

[7] J. C. Maxwell, "A Treatise on Electricity and Magnetism," London, 1891.

[8] Magnetics, "MAGNETICS® Ferrite Cores Design Manual and Catalog," Pittsburgh.

[9] R. Petkov, "Optimum design of a high-power high-frequency transformer," *IEEE Transaction on Power Electronics,* vol. 11, pp. 32-42, 1996.

[10] C. Jie, "Advancement and trends of power electronics for industrial applications," 2003, pp. 3021-3022 Vol.3.

[11] B. J. Swart, J. A. Ferreira, and J. D. van Wyk, "Temperature as function of frequency in multiple core magnetic assemblies with variable core size and flux density," 1994, pp. 1261-1268 vol.2.

[12] Cadence Design Systems, "PSpice A/D User's Guide Schematic Version," San Jose, CA, 2000.

[13] Ansoft, "Simplorer JA6 Core Model," Ansoft.

[14] M. Vrancken, W. Aerts, and G. A. E. Vandenbosch, "Benchmark of full Maxwell 3D electromagnetic field solvers on an SOIC8 packaged and interconnected circuit," *INT J RF MICROW C E* vol. 16, pp. 143-154, 2005.

[15] K. D. T. Ngo, "Subcircuit modeling of magnetic cores with hysteresis in PSpice," *Aerospace and Electronic Systems, IEEE Transactions on,* vol. 38, pp. 1425-1434, 2002.

[16] D. Jiles and D. Atherton, "Theory of Ferromagnetic Hysteresis," *J. Magn. Magn. Mater.,* vol. 61, pp. 48-60, 1986.

[17] D. Jiles, "The Effects of Eddy Current Losses on Frequency Dependent Hysteresis in Electrically Conducting Media," *IEEE Transactions on Magnetics,* vol. 30, pp. 4326-4329, November 1994 1994.

[18] C. Kittel, "Physical Theory of Ferromagnetic Domains," *Phys. Rev., ,* vol. 21, pp. 541-592, 1949.

[19] D. Jiles, "Introduction to Magnetism and Magnetic Materials," in *Introduction to Magnetism and Magnetic Materials* New York: Springer, 1991, pp. 31, 70,109, 128-130.

[20] C. R. Nave, "Hyperphysics," Atlanta, 2006.

[21] McGraw-Hill, "McGraw-Hill Concise Encyclopedia of Science & Technology ", 2005.

[22] J. Brown William Fuller *Micromagnetics*. New York: John Wiley & Sons, 1963.

[23] A. H. Morrish, *The Physical Principle of Magnetism*: John Wiley & Sons, 1965.

[24] S. Ramo, J. R. Whinnery, and T. V. Duzer, "Fields and Waves in Communication Electronics 3rd Eddition," New York: John Wiley & Sons, Inc., 1994, pp. 72-75.

[25] A. T. Williams, "Consciousness, Physics, and the Holographic Paradigm," 2007.

[26] H. D. Young, *Sears and Zemansky's University Physics with Modern Physics, 11th Ed by Young and Freedman, Addison-Wesley (2004)*, 2004.

[27] S. Blundell, "Magnetism in Condensed Matter," in *Magnetism in Condensed Matter*, 2001, pp. 2, 32, 74,128.

[28] R. C. Smith, "Smart Material Systems: Model Development " Philadelphia: Society for Industrial and Applied Mathematics, 2005, pp. 89-93.

[29] G. Bertotti, *Hysteresis in Magnetism: for Physicists, Materials Scientists, and Engineers*. San Diego: Academic Press 1998.

[30] R. M. Rose, L. A. Shepard, and J. Wulff, *The Structure and Properties of Materials, Vol. 4: Electronic Properties*. New York: John Wiley & Sons, Inc., 1966.

[31] D. C. J. Y.M. Shi, A. Ramesh, "Generalization of hysteresis modeling to anisotropic and textured materials," *J. Magn. Magn. Mater.,* vol. 187, pp. 75-78, 1998.

[32] A. Ramesh, D. C. Jiles, and J. M. Roderick, "A model of anisotropic anhysteretic magnetization," *Magnetics, IEEE Transactions on,* vol. 32, pp. 4234-4236, 1996.

[33] R. M. Bozorth, "Ferromagnetism," Princeton: Van Nostrand, 1951, pp. 8-9.

[34] Z. Gao, D. C. Jiles, and D. L. Atherton, "Dependence of energy dissipation on annealing temperature of melt–spun NdFeB permanent magnet materials," *J. Appl. Phys.,* vol. 79, 1996.

[35] D. C. Jiles, J. B. Thoelke, and M. K. Devine, "Numerical determination of hysteresis parameters for the modeling of magnetic properties using the theory of ferromagnetic hysteresis," *Magnetics, IEEE Transactions on,* vol. 28, pp. 27-35, 1992.

[36] P. R. Wilson, J. N. Ross, and A. D. Brown, "Dynamic electrical-magnetic-thermal simulation of magnetic components," 2000, pp. 287-292.

[37] A. D. Snider, *Partial Differential Equations*. Upper Saddle River: Prentice Hall, 1999.

[38] D.C. Jiles, "Frequency Dependence of Hysteresis Curves In Ferromagnetic Materials," 1993, pp. EE-01-EE-01.

[39] J. Pearson, P. T. Squire, and D. Atkinson, "Which anhysteretic magnetization curve" *Magnetics, IEEE Transactions on,* vol. 33, pp. 3970-3972, 1997.

[40] W. R. Wright, "The Magnetization of Iron in the Absence of Hysteresis," *Physical Review,* vol. 11, p. 161, 1918.

[41] C. W. T. McLyman, "Transformer and Inductor Design Handbook," New York: Marcel Dekker, Inc., 1978, pp. 16-17, 277.

[42] R. S. Popovic, C. Schott, L. Shibasaki, J. R. Biard, and R. B. Foster, "Hall-Effect

Magnetic Sensors," in *Magnetic Sensors and Magnetometers*, P. Ripka, Ed. Boston: Artech House, 2001, pp. 181-184.

[43] F. Fiorillo, "Measurement and Characterization of Magnetic Materials," in *Measurement and Characterization of Magnetic Materials*: Academic Press, 2004, pp. 346-348.

[44] A. Microtechnology, "Precision Magnetic Deflection," in *Application Note 5*, 2001.

[45] "IEEE standard for test procedures for magnetic cores," 1992.

[46] F. Jorgensen, "The Complete Handbook of Magnetic Recording," in *The Complete Handbook of Magnetic Recording* New York: McGraw-Hill, 1996, p. 595.

[47] D. B. Clarke, "Demagnetization Factors of Ringcores," *IEEE Transactions on Magnetics,* vol. 35, pp. 4440-4444, 1999.

[48] D. Lederer, H. Igarashi, A. Kost, and T. Honma, "On the parameter identification and application of the Jiles-Atherton hysteresis model for numerical modelling of measured characteristics," *Magnetics, IEEE Transactions on,* vol. 35, pp. 1211-1214, 1999.

[49] Maplesoft, "Maple User Manual," Maplesoft, 2005.

[50] S. Kadamani and A. D. Snider, "USFKAD: An expert system for partial differential equations," *Computer Physics Communications,* vol. 176, pp. 62-69, 2007.

[51] C. D. Mee and E. D. Daniel, *Magnetic Recording*. New York: McGraw-Hill, 1988.

About the Author

Jeremy Walker received his Bachelor's Degree in Electrical Engineering in the 2000 and was awarded a full scholarship and stipend to Mississippi State University through the state-sponsored ComPEET program. While earning his Master's Degree from Mississippi State University, Mr. Walker specialized in analog and digital IC design.

While in the Ph.D. program at the University of South Florida, Mr. Walker held numerous teach roles both as a teaching assistant and instructor, where he thoroughly enjoyed assisting students on projects and other work.

Mr. Walker's work has focused on the measurement and modeling of magnetic cores with particular emphasis on the modeling of the anhysteretic magnetization, which is the subject of most of this dissertation and future journal papers.